Efficiency Loss Mechanisms in Colloidal Quantum-Dot Light-Emitting Diodes

by

Yasuhiro Shirasaki

S.B., Massachusetts Institute of Technology (2006)
M.Eng., Massachusetts Institute of Technology (2008)

Submitted to the Department of Electrical Engineering and Computer Science
in partial fulfillment of the requirements for the degree of

Doctor of Philosophy in Electrical Engineering

at the

MASSACHUSETTS INSTITUTE OF TECHNOLOGY

June 2013

Author ....
Department of Electrical Engineering and Computer Science
May 22, 2013

Certified by ....
Vladimir Bulović
Professor of Electrical Engineering
Thesis Supervisor

Accepted by ....
Leslie A. Kolodziejski
Chair, Department Committee on Graduate Theses

Efficiency Loss Mechanisms in Colloidal Quantum-Dot Light-Emitting Diodes

by

Yasuhiro Shirasaki

Submitted to the Department of Electrical Engineering and Computer Science
on May 22, 2013, in partial fulfillment of the
requirements for the degree of
Doctor of Philosophy in Electrical Engineering

Abstract

Saturated and tunable emission colors make colloidal quantum-dot light-emitting diodes (QD-LEDs) interesting for the next generation of display and lighting technologies. However, there still remain various hurdles to the commercialization of QD-LEDs, including their relatively low external quantum efficiencies (EQE).

In this thesis, we study the efficiency loss mechanisms present in the latest generation of QD-LEDs. We start with understanding the origin of reduced efficiencies at high current density operation, known as the efficiency roll-off. Through simultaneous measurement of quantum dot (QD) electroluminescence (EL) and photoluminescence (PL) efficiencies during device operation, we identify that the reduced PL efficiency of the QDs at high current densities is the cause for the efficiency roll-off. Furthermore, comparison of QD EL spectra, taken under forward bias, and PL spectra, taken under reverse bias, suggests that this reduced PL efficiency is electric-field-induced. We use the relationship between PL peak-shifts and PL quenching of QDs subject to the quantum confined Stark effect to predict the efficiency roll-off in forward bias. The roll-off predicted by this analysis is in excellent agreement with our experimental data and correctly traces an EQE reduction of nearly 50%. We complement the EL-PL study with electroabsorption spectroscopy measurements of a biased QD-LED, which confirms that the charging of the QDs is not voltage bias dependent and is thus unrelated to the roll-off. Finally, we study the effect of Auger recombination on QD-LEDs by varying the QD layer thickness. QD-LEDs with thicker QD layers exhibit lower peak EQEs and QD transient PL with stronger bi-exponential behavior. We attribute the strength of the bi-exponential behavior to the fraction of the QDs charged in the device, which can explain the correlation between the strength of the bi-exponential behavior and the EQE.

Thesis Supervisor: Vladimir Bulović
Title: Professor of Electrical Engineering

Acknowledgments

This work would not have been possible without the help and support of many people. First I would like to thank my advisor, Prof. Vladimir Bulović, who has been a great mentor and also an inspirational leader. I am very grateful for his patience as I explored many different projects over the years in his group, only some of which are covered in this thesis. I would also like to thank my committee members, Prof. Tomas Palacios and Prof. Vanessa Wood, for their insights and advice on quantum dots and optoelectronic devices which were essential to the formation of this thesis. Although it is not directly reflected in this thesis, I am grateful to Prof. Marc Baldo and Prof. Rajeev Ram for many insightful discussions we had regarding my experiments.

Many of the experiments presented in this thesis were in collaboration with colleagues at the Organic and Nanostructured Electronics Laboratory. In particular, I would like to thank Geoffrey Supran, Dr. Katherine Stone, Prof. William Tisdale, and Katherine Song. Their contributions were essential to both fabricating the LEDs and understanding their operating mechanisms. I would also like to thank the rest of the ONE Lab for making the work environment fun and keeping the facilities operational. I would also like to thank the former members of the group, Prof. Polina Anikeeva, Prof. Jonathan Tischler, and Prof. Scott Bradley, for getting me started at ONE Lab, teaching me about organic materials and various device fabrication techniques.

I would also like to thank my friends, Kevin Sung, Daniel Kraemer, Anirban Mazumdar, and the other members of the JSU who brought me laughs on and off the basketball court.

Lastly I would like to thank my wife, Kimi, my brother, and my parents for being supportive every step of the way through the long graduate school days.

Contents

1 Introduction **21**

2 Background **25**

2.1 Colloidal Quantum Dots 26

2.1.1 What is a Quantum Dot? 26

2.1.2 The Benefits of Colloidal QDs for Light-Emitting Applications 27

2.2 Physics of Quantum Dots 34

2.2.1 Cadmium Selenide Semiconductor 34

2.2.2 Particle in a Sphere 34

2.2.3 Excited States of QDs 37

2.3 Organic Optoelectronics 41

2.3.1 Organic Semiconductors 41

2.3.2 Excitons 44

2.3.3 Organic Light-Emitting Diodes 44

2.4 Quantum-Dot Light-Emitting Devices 46

2.4.1 Evolution of QD-LEDs 46

2.4.2 Novel QD-LEDs 53

3 QD-LED Fabrication and Testing **57**

3.1 Fabrication Methods 57

3.1.1 Solution Processing 59

3.1.2 Physical Vapor Deposition 60

3.2 Device Testing 62

3.2.1 Current-Voltage and External Quantum Efficiency 63
3.2.2 Luminance 64
3.3 QD-LED used in this Thesis 65

4 Efficiency roll-off in QD-LEDs 67
4.1 Efficiency roll-off 68
4.2 Cause of efficiency roll-off in QD-LEDs 68

5 QD Luminescence Quenching in QD-LEDs 75
5.1 QD Luminescence Quenching Mechanisms 76
5.2 Electric-Field-Induced Quenching of QD Luminescence 79

6 Electroabsorption Spectroscopy Study on QD-LEDs 91
6.1 Features of Charged QDs 92
6.2 Electroabsorption Spectroscopy on a QD-LED 93

7 Charging in QD-LEDs 105
7.1 Auger Recombination in QDs 106
7.2 Auger Recombination in a QD-LED 107

8 Conclusions and Outlook 115
8.1 Thesis Summary 115
8.2 Outlook 117

A QD-LED Fabrication Procedure 119
A.1 QD Solution Preparation 119
A.2 Substrate Preparation 120
A.3 QD-LED Fabrication 120

B Supplementary Information 123
B.1 Förster Resonance Energy Transfer 123
B.2 Space-Charge-Limited and Trap-Filled Limit Conduction 128
B.3 Coulomb attraction 132

B.4 Modeling QD PL quenching in section 5.2 133

List of Figures

1-1 Typical EQE vs current density curve for a QD-LED. Three regimes of operation are defined: low current density, optimal current density, and high current density. 22

2-1 Tunable and pure color light emission from colloidal QDs. (a) Solutions of colloidal QDs of varying size and composition, exhibiting PL under optical (ultraviolet) excitation [1]. (b) PL spectra of CdSeZnS and PbSCdS coreshell colloidal QDs. The upper inset shows a schematic of a typical coreshell colloidal QD [2]. The lower inset is a high-resolution transmission electron microscope image of a CdSe QD (scale bar, 1.5 nm) [3]. (a) Demonstrates the size- and composition-dependent tunability of QD emission color, whereas (b) shows the extension of this narrow-band emission into the NIR. QD-LED EL typically closely matches the corresponding PL spectra. 28

2-2 Optical advantages of colloidal QDs for display and SSL applications. (a) CIE chromaticity diagram showing that the spectral purity of QDs enables a color gamut (dotted line) larger than the high-definition television (HDTV) standard (dashed line). (b) Plot showing the luminous efficacy and CRI of various commercially available lighting solutions. The first commercial QD-based SSL source, developed by QD Vision and Nexxus Lighting, consists of sheets of red QDs backlit by a blue LED with a yellow phosphor coating, resulting in a high CRI without compromising high luminescence efficacy. Recently, Philips A-Style LED, which employs remote phosphors, has demonstrated even more energy-efficient lighting. There is evidently an emerging market for high-quality optical downconverters, such as QDs. 30

2-3 (a) An example of an energy band diagram of an direct bandgap semiconductor. (b) For QDs, only the states with k that can satisfy the boundary condition can exist. From ref. [4]. 35

2-4 The first four spherical Bessel functions with l=0, 1, 2, and 3, corresponding to s, p, d, and f orbitals respectively. To satisfy the boundary condition of a QD, the spherical Bessel function must be zero at the surface of the QD. 36

2-5 Energy band diagram of a CdSe semiconductor. There are three valence bands due to the fact that they originate from Se p orbitals. The degeneracy is lifted due to the spin-orbit coupling and the crystal field splitting. From ref. [4]. 39

2-6 (a) Schematic of a benzene ring. Each carbon atom has sp^2 hybridized orbitals, forming σ bonds with two neighboring carbons and a hydrogen, and a p_z orbital protruding out of the plane of the molecule. Neighboring p_z orbitals weakly overlap, forming π bonds, and results in delocalization of electrons over the π orbital. (b) Chemical structure of the benzene ring showing conjugated bonds. (c) Energy band diagram of the benzene ring showing HOMO and LUMO. The electrons fill half of the π orbital states [courtesy of Tim Osedach]. 43

2-7 Chemical structures of CBP and TCTA. 43

2-8 (a) Wannier-Mott exciton in a crystal lattice. (b) Frenkel exciton tightly bound to a single molecule [courtesy of Tim Osedach]. 45

2-9 Progression of orange/red-emitting QD-LED performance over time in terms of peak EQE and peak brightness. (a) Peak EQE. (b) Peak brightness. QD-LEDs (a substantial but non-exhaustive selection from the literature) are classified into one of four types, as described in the text, and are compared with selected orange/red-emitting (phosphorescent) OLEDs. Solid lines connect new record values. [5] 46

2-10 Type-II QD-LED. (a) The prototypical type-II QD-LED structure, comprising a monolayer of QDs sandwiched between an organic hole-transport layer (HTL) and an organic electron-transport layer (ETL) [6]. Its corresponding energy band diagram is shown in Fig. 2-10(e). Inset: an atomic force microscope image of a monolayer of QDs on an organic HTL. (b) Photographs of EL from type-II QD-LEDs with varying QD compositions and their respective emission spectra [1]. . . 48

2-11 QD excitation mechanisms.There are four routes for generating excitons in QDs that have been used in QD-LEDs. (a) Optical excitation: an exciton is formed in a QD by absorbing a high-energy photon. (b) Charge injection: an exciton is formed by injection of an electron and a hole from neighboring CTLs. (c) Energy transfer: an exciton is transferred to a QD via FRET from a nearby donor molecule. (d) Ionization: a large electric field ionizes an electron from one QD to another, thereby generating a hole. When these ionization events occur throughout a QD film, generated electrons and holes can meet on the same QD to form excitons. (e) Energy band diagram of a typical type-ii QD-LED that outlines the two suspected QD excitation mechanisms: charge injection and energy transfer. 49

2-12 State-of-the-art QD-LEDs and their use in large-area devices. (a) Energy band diagram of the first type-iv QD-LED employing ZnO [7]; the electron transport layer of choice in todays high-performance devices; PEDOT, poly(3,4-ethylenedioxythiophene); PVK, poly-N-vinyl carbazole. (b) The first demonstration of red-green-blue EL from (type-ii) QD-LED pixels, patterned using microcontact printing [8]. (c) This technique has been harnessed to produce a 4-inch full-color active matrix type-iv QD-LED display [9]. (d) Flexible white-emitting type-ii QD-LED [10]. 50

3-1 Diagram and a picture of the Organic and Nanostructured Electronics Laboratory (ONE Lab) where most of the device fabrication is performed. [Courtesy of Tim Osedach] 58

3-2 Diagram and a picture of the thermal evaporator used in ONE Lab [Courtesy of Tim Osedach]. 61

3-3 Diagram and a picture of the RF magnetron sputtering system used in ONE Lab [Courtesy of Tim Osedach]. 62

3-4 A typical current density vs. voltage relationship observed for a QD-LED. Plotting the curve in log-log scale presents two regimes where the curve follows a power law. Below the turn-on of the diode, the curve exhibits ohmic conduction (power of 1). After the turn-on, the curve exhibits trap-limited conduction (power greater than 2; 6.7 in this case). 63

3-5 The luminosity function shows the sensitivity of an average human eye as a function of wavelength. 65

3-6 Current density and normalized EQE as a function of voltage for a typical QD-LED used in this thesis. The peak EQE is 2%. The inset shows the energy levels of the device based on literature values. . . . 66

3-7 A picture of a QD-LED used in this thesis, emitting at 610 nm. Ten devices are patterned onto each of 0.5 in × 0.5 in glass substrates. . . 66

4-1 EQE roll-offs for different kinds of LEDs including an OLED [11], a type-IV QD-LED [12], a GaN LED [13], and a QD-LED fabricated at ONE Lab. The roll-off is an universal behavior for LEDs but the cause is different for each type of LED. 69

4-2 Simultaneous electroluminescence and photoluminescence measurement setup. The PL efficiency of the QDs in a QD-LED is measured as the device bias is swept by illuminating the device with $\lambda = 530$ nm LED light modulated at 1 kHz. The combined EL and PL is collected using a Si photodiode and sent to a lock-in amplifier, where the PL signal (AC) is separated from the EL signal (DC). 70

4-3 Absorption spectra of the main constituents of the QD-LED: QD, ZnO, and CBP. Excitation wavelength of $\lambda = 530$ nm ensures the selective excitation of the QDs in the device. 71

4-4 Relative PL efficiency of the QDs in the QD-LED as a function of bias voltage for three different excitation intensities: 15.6, 34.4, 44.5 μW. The PL efficiency is independent of the excitation intensity, indicating that the optically formed excitons are not affecting the measured PL efficiencies. 72

4-5 EQE and QD PL intensity of the QD-LED (normalized at 4 V, when the peak EQE = 2%) as a function of voltage. Roll-off of the EQE above 4 V reflects reduced QD PL efficiency at high biases. 73

5-1 Three QD PL quenching mechanisms possible in a QD-LED. (a) The Auger recombination involves an exciton non-radiatively transferring its energy to a nearby free charge carrier. (b) Heat-induced quenching involves one or both of the charge carriers constituting an exciton escaping to a surface defect state via thermal excitation. (c) Electric-field-induced quenching involves dissociation of an exciton or reduced radiative recombination rate due to reduced overlap between the electron and hole wavefunctions. 76

5-2 PL spectra of a QD thin film as a function of temperature. 78

5-3 PL measurement setup to measure the QD PL spectra of QD-LEDs as they are reversed biased using the sawtooth-like voltage waveform shown in Fig. 5-4 80

5-4 Electric-field-dependent QD PL was measured by applying a sawtooth-like voltage waveform to the QD-LED and illuminating it with a 530 nm LED pulse synchronized with the voltage waveform. QD PL at varying electric fields was measured by sweeping the delay (phase) between the voltage waveform (black line) and the LED pulse (green line). 81

5-5 EL measurement setup to measure the QD EL spectra of QD-LEDs as they are forward biased. The integration time of the spectrometer is adjusted as the LED gets brighter to avoid saturation. 82

5-6 Comparison of QD PL spectra (black lines) and QD EL spectra (orange diamonds) at corresponding peak emission energies, for three different biases. At high biases, the PL spectrum exhibits a red shoulder that is not observed at lower biases or in the EL spectrum. Insets: PL spectra (black) are reconstructed (green) using two Gaussians, which correspond to emission from two QD subpopulations A and B (red and blue, respectively). 83

5-7 (a) Relative intensities of subpopulations A (red) and B (blue). The PL data are fitted to a simplified version of the model presented in Ref. [14]. (b) Peak energies of subpopulation A (red) and subpopulation B (blue). Quadratic fits (black lines) to the PL data are made assuming that the shifts are due to the quantum confined Stark effect. 85

5-8 Measured EQE and predicted EQE as a function of voltage. EQE is predicted through the comparison of PL and EL data [Figs. 5-7(a) and (b)] as described in the text. The agreement between the data and the prediction shows that the quantum confined Stark effect can self-consistently account for the QD-LED efficiency roll-off. 86

5-9 Transient PL of QDs in the QD-LED reverse biased at 0, -8, -12, and -16 V. Time constants of the decays (inset) are independent of the applied voltage, suggesting that the nonradiative exciton recombination rate is independent of the electric field. 88

5-10 Three possible mechanisms for the electric-field-induced quenching of QD PL: (a) Reduced electron-hole wavefunction overlap leads to a decrease in radiative exciton recombination rate. (b) Exciton dissociation leads to an increase in nonradiative exciton recombination rate. (c) Hot charge carrier trapping by QD surface traps leads to a decrease in the probability of forming bandedge excitons. 89

6-1 Absorption bleaching in charged CdSe QDs.(a) An extra electron in the conduction band decreases the $1S_{3/2}$-$1S_e$ transition probability by 50%. (b) Absorption spectrum for a solution of the QDs (solid line) and a change in the absorption spectrum of charged QDs. (c) Time-dependent change in the percentage bleaching of the band-edge-exciton state [15]. 94

6-2 Top: Current density-voltage and external quantum efficiency (EQE)-voltage characteristics of the QD-LED under investigation. Inset: Energy band-diagram of the device, with indicated energy values referenced to the vacuum level. Bottom: Timing diagram for the electroabsorption spectroscopy measurement. The voltage is applied for 1.5s, during which current, EQE, and EL spectrum measurement are taken. The voltage is then turned off for 4s, during which the electroabsorption measurement is taken. The voltage is then stepped up and the process is repeated. 95

6-3 Measurement setup for the electroabsorption spectroscopy. A white light source (Xenon lamp) is split into two beams, with one reflected off of a QD-LED and the other reflected off of a reference sample, and focused into the spectrometer. The two spectra are taken simultaneously to later account for any spectral fluctuation of the lamp. 96

6-4 (a) Electroabsorption spectra of the QD-LED exhibiting four distinct features above 8 V bias. (b) Transient absorption spectra of the main constituents of the QD-LED. (c) Linear absorption spectrum of the QD. 98

6-5 Top: Absorption spectra of the main constituents of our QD-LED: QD, ZnO, and CBP. Middle: Spectra of pump and probe used for the TA measurements on ZnO and CBP. Bottom: Spectra of pump and probe use for the TA measurements on QD. 99

6-6 (a) The electroabsorption spectra of the QD-LED focused around $\alpha 1$ and $\beta 1$. (b) $\alpha 1$ and $\beta 1$ simulated by red-shifting a Gaussian absorption profile by varying energies. The Gaussian profile is obtained from fitting a Gaussian to the B1 feature in Fig. 6-4(b). (c) Peak energies of the EL spectra as a function of applied voltage. (d) Change in the four electroabsorption features as a function of applied voltage. The solid lines are the simulated change in the amplitudes of the electroabsorption features using the model described in the text. 101

6-7 The dynamics of the four electroabsorption features as the device was biased from 0 to 13 V (t = -30 s) and then turned off (t = 0 s). The long retention time (~7 min) indicates that the electric field responsible for the EA features is due to trapped charges in the QD-LED. 103

7-1 Transient PL of a single QD charged by an electrochemical setup. The negative voltage applied is correlated with the degree of charging and results in faster PL decay curves with more negative voltages. From Ref. [16] 106

7-2 Current density-voltage characteristic of QD-LEDs with three different QD layer thicknesses: 7, 14, and 28 nm. Large dependence of the current-voltage characteristic on the QD layer thickness indicates that the QD layer poses a significant electrical resistance in the device. Inset: device structure of the QD-LED. 108

7-3 Top: EQE-voltage characteristic of the QD-LEDs. Bottom: EL peak energy-voltage characteristic of the QD-LEDs. The EL peak energies are obtained by fitting double-Gaussian to the EL spectra. The EQE roll-off tracks the EL peak energy roll-off as explained in section 5.1. . 109

7-4 Transient PL of QDs in the QD-LEDs before and after a 2s operation at 1 A/cm^2. The PL transients exhibit a stronger bi-exponential behavior after operation with the strongest bi-exponential behavior observed from the QD-LED with the thickest QD layer. Dotted curve is an example bi-exponential fit to this PL transient curve. 111

7-5 Fraction of the QDs charged in the QD-LEDs before and after the operation. The values are calculated from the bi-exponential fits to the QD PL transient curves as described in the text. 112

7-6 QD charging fraction for the QD-LED with 28 nm QD layer before and after the operation (t=0). The QDs remain charged for hours and are not fully discharged to its original state for days. 113

Chapter 1

Introduction

Colloidal quantum-dot light-emitting diodes (QD-LEDs) are thin film light-emitting devices ($\sim$ 100 nm thick) that uses colloidal semiconductor nanocrystals called quantum dots (QDs) as luminophores. In essence, they are an extension of organic light-emitting diode (OLEDs) technology, sharing many of the material sets and the fabrication techniques. As such, QD-LEDs possess many of the traits that have made OLEDs appealing for display and lighting technologies. Some of these traits include the ability to use low cost fabrication methods like solution processing, to fabricate on an amorphous substrate, and to pattern red-green-blue emitting LEDs side by side. Furthermore, these devices can be fabricated onto flexible substrates to make flexible displays. QD-LEDs offer additional advantages of more saturated emission color, the ability to emit in the near-infrared (NIR), which is not possible with OLEDs, and the possibility of being more stable than OLEDs which often suffer from degradation of its organic layers upon exposure to air.

The advantages of QD-LEDs are clear. However, despite almost two decades of research since their first demonstration, understanding of the mechanisms by which these devices operate remains shallow. In most cases, electrical excitation of the QDs indicate successful injection of electrons and holes into the QDs. Literature that attempts to further explain the attributes of QD-LEDs through either experiments or theoretical modeling is still scarce.

In this thesis, we attempt to deepen our understanding of QD-LEDs through

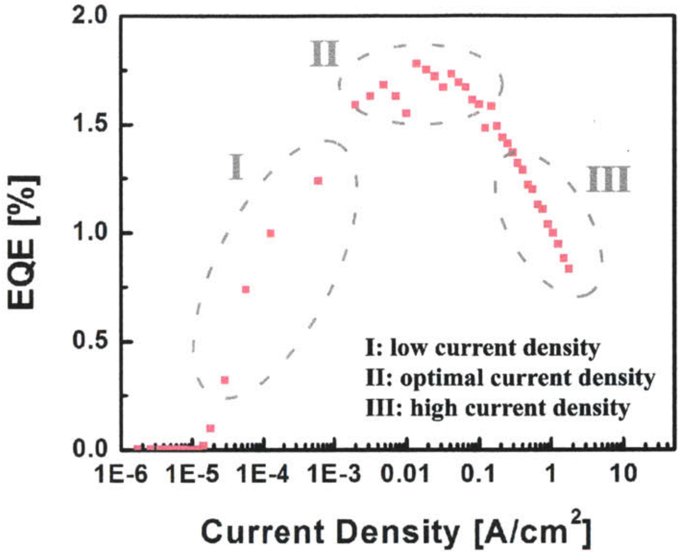

Figure 1-1: Typical EQE vs current density curve for a QD-LED. Three regimes of operation are defined: low current density, optimal current density, and high current density.

investigations of mechanisms that limit the efficiency of these devices. The metric that we focus on is external quantum efficiency (EQE), which is the ratio of the number of photons emitted out of a device to the number of electrons injected into the device. A typical graph of EQE as a function of current density through the device is shown in Fig. 1-1. We define three regimes of operation: low current density, optimal current density, and high current density. In order to make QD-LEDs useful for various applications that require different current density operations, we must first understand the limiting factors of the EQE in these three regimes. Low efficiency at the low current density regime is often a consequence of the current leakage through the device that does not contribute to light emission. This thesis, instead, focuses on identifying the loss mechanisms that limit the EQE at the optimal and high current density regimes.

The structure of this thesis is as follows. Chapter 2 reviews the basics of quantum dots, organic semiconductors, and light-emitting devices that use these materials. Chapter 3 reviews the the fabrication and the performance of the QD-LEDs used in this thesis. Chapter 4 discusses the concept of reduced efficiency of a QD-LED at high-current-density operation, known as the "efficiency roll-off." Through simultaneous electroluminescence (EL) and photoluminescence (PL) efficiency measurements, we identify diminished QD luminescence efficiency to be the cause of the roll-off. Chapter 5 discusses possible mechanisms that can quench the QD luminescence in the high-current-density regime. Through comparison of QD EL and PL spectra, we identify electric-field-induced quenching of the QD luminescence as the likely cause of the roll-off. Chapter 6 explores the possibility of Auger recombination due to charged QDs, another QD luminescence quenching mechanism, contributing to the efficiency roll-off. Through electroabsorption measurements, we confirm that the charging of the QDs is not voltage bias dependent, and thus unrelated to the roll-off. Chapter 7 discusses how the Auger recombination may be playing a role in determining the peak EQE in the optimal-current-density regime. Chapter 8 is the conclusion of this thesis and discusses possible future directions of the research.

Much of chapter 2 is published in ref. [5]. Chapters 4 and 5 are published in ref. [17]. Manuscripts covering chapters 6 and 7 are currently in preparation [18,19].

Chapter 2

Background

This chapter addresses the technological potential of optically and electrically excited QDs for high-color-quality lighting and display technologies by reviewing the QD technology, their advantages, and their recent progress with respect to other comparable technologies. Initial applications of QD luminescence harness the optically-induced emission (photoluminescence, PL) of colloidal QDs for use in the backlighting of liquid-crystal displays and in visible and near-infrared (NIR) optical down-converters for inorganic and organic solid-state lighting (SSL) sources. This is evidenced by the large number of start-up companies and major corporations developing colloidal QD-enhanced displays and SSL sources, such as QD Vision, Nanosys, LG Innotek, Samsung, Philips Lumileds Lighting Company and Avago [20]. In the longer term, one can envision the development of large-area QD-LED flat-panel displays reliant on the electrically induced emission (electroluminescence, EL) of colloidal QDs, which is a target also being pursued commercially. With the global flat-panel display market exceeding US $80 billion in 2011 [21], and with lighting constituting 20% of US electricity consumption [20], the economic and environmental incentives are clear.

2.1 Colloidal Quantum Dots

2.1.1 What is a Quantum Dot?

Colloidal quantum dots are solution-processed nanoscale crystals of semiconducting materials. The unique size-dependent optical properties of QDs have motivated increasingly active research aimed at applying them in the next generation of optoelectronic and biomedical technologies. Since the first directed QD synthesis three decades ago, QD thin-films have been featured in a range of optoelectronic devices, including LEDs [7,22–24], solar cells [25], photodiodes [26], photoconductors [27], and field-effect transistors [28], while QD solutions have been used in a myriad of invivo and invitro imaging, sensing, and labeling techniques [29]. The market for QD-based products has been forecast to grow rapidly from 2012 to 2015, with particularly rapid growth in the optoelectronics sector [20].

Epitaxial versus Colloidal Quantum Dots

Quantum dots may be categorized by their synthetic route as either colloidal or epitaxial (also known as self-assembled). Whereas the latter are derived from relatively high-energy-input dry methods of epitaxial growth from the vapor phase [30], colloidal QDs are synthesized by wet chemical approaches [4] and are the focus of this thesis. The precise size and shape control, as well as the high monodispersity, spectral purity, and photoluminescence quantum yields, η_{PL} (that is, the number of photons emitted per photon absorbed) afforded by the chemical synthesis of QDs, are unmatched by epitaxial techniques. Colloidal QDs are freestanding and therefore amenable to numerous chemical post-processing and thin-film assembly steps, in contrast with epitaxial QDs, which are substrate-bound [31]. Additionally, the relatively inexpensive, facile and scalable solution-based conditions necessary for the synthesis of nearly defect free colloidal QDs have an impurity tolerance far exceeding that of the ultrahigh-vacuum environments required for epitaxial growth. Moreover, only weak quantum-confinement effects are observed in epitaxial QDs [32] due to their relatively large lateral dimensions (typically > 10 nm) and difficulties associated with size control. This is in stark contrast with the size-tunable emission of colloidal QDs, which are therefore favorable as luminophores in LEDs [33].

Quantum Dot Chemistry

Colloidal QDs comprise a small inorganic semiconductor core (1-10 nm in diameter), often a wider-bandgap inorganic semiconductor shell, and a coating of organic passivating ligands (Fig.2-1(b), insets). The benchmark QD preparation technique, which yields high quality and monodisperse (size variation of $< 4\%$) QDs, involves the pyrolysis of organometallic precursors injected into a hot organic coordinating solvent at temperatures of 120-360°C [4, 34, 35]. Thermally activated nucleation and growth of small crystallites from the precursors ensues until arrested by cooling. Fine control over QD size (for example, 1.5-12nm for CdSe QDs [34]) and size dispersion can therefore be achieved by controlling the reaction time and temperature, as well as precursor and surfactant concentrations. Post-synthesis size-selective precipitation can further increase monodispersity in colloidal QD solutions. The resulting QDs are dressed with organic ligands, which confer solubility in a diversity of common non-polar solvents. Scaling up this technique to reduce the cost of QDs is a prerequisite for the commercialization of QD technologies, and yield increases from milligrams to kilograms per week have been reported [20, 36].

2.1.2 The Benefits of Colloidal QDs for Light-Emitting Applications

Tunable and Pure Colors

The greatest asset of QDs for light-emitting applications is their tunable bandgap, which is governed by the quantum size effect. Confinement of electron-hole pairs (excitons) on the order of the bulk semiconductor's Bohr exciton radius (5.6 nm for CdSe) leads to quantization of the bulk energy levels, resulting in atomic emission-like spectra. Another result of this confinement is that the QD's bandgap increases as its size decreases, leading to a blue shift in emission wavelengths [37]. This is shown in

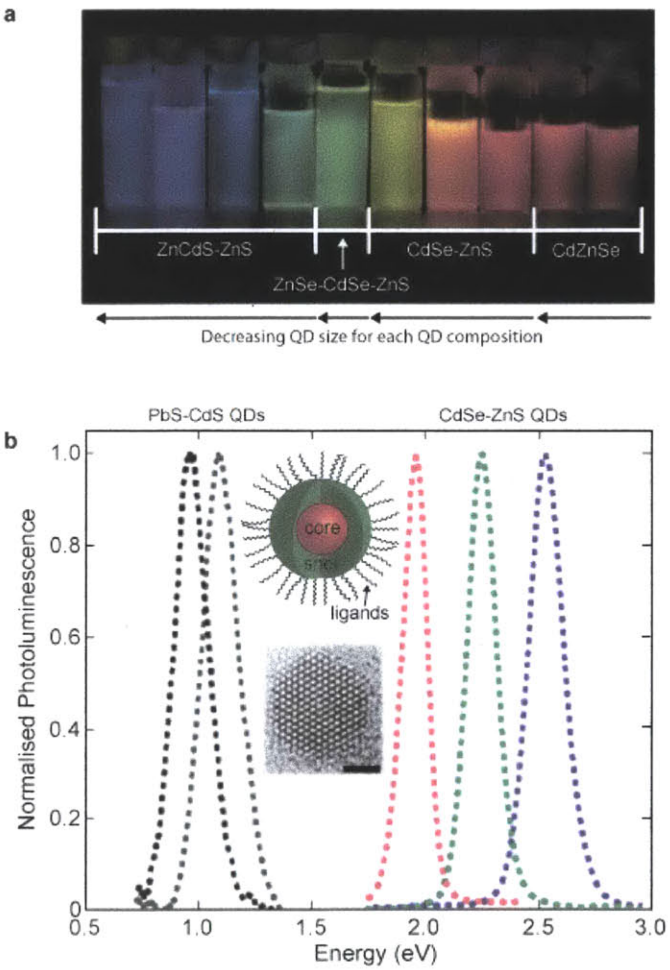

Figure 2-1: Tunable and pure color light emission from colloidal QDs. (a) Solutions of colloidal QDs of varying size and composition, exhibiting PL under optical (ultraviolet) excitation [1]. (b) PL spectra of CdSeZnS and PbSCdS coreshell colloidal QDs. The upper inset shows a schematic of a typical coreshell colloidal QD [2]. The lower inset is a high-resolution transmission electron microscope image of a CdSe QD (scale bar, 1.5 nm) [3]. (a) Demonstrates the size- and composition-dependent tunability of QD emission color, whereas (b) shows the extension of this narrow-band emission into the NIR. QD-LED EL typically closely matches the corresponding PL spectra.

Fig.2-1(a), which also illustrates how this spectral tunability can be extended through changes in QD chemical composition and stoichiometries [1, 38]. Such systematic and precise spectral tunability of efficient emission, even in the NIR region, is a distinguishing technological advantage of QDs over organic dyes. CdSe-based core-shell QDs are currently the material of choice for visible-wavelength QD-LEDs [1, 12, 39, 40], and lead chalcogenide QDs dominate NIR devices [41, 42]. In the visible range, the spectrally narrow emission of QDs (see Fig.2-1(b); full-width half-maximum (FWHM) of around 30nm for CdSe) [34] compared with those of inorganic phosphors (FWHM $\sim$ 50 - 100nm) [43] identifies QDs as outstanding luminescent sources of saturated emission color.

This high color quality is quantifiable on the Commission International del Eclairage (CIE) chromaticity diagram (Fig. 2-2(a)), which maps colors visible to the human eye in terms of hue and saturation. By combining the emission of three light sources, such as red, green and blue emissive display pixels, a set of apparent colors can be generated corresponding to the colors enclosed by the triangle on the CIE diagram. Fig. 2-2(a) shows that, with the highly saturated color of QD emission, it is possible to select red-green-blue QD-LED sources whose subtended color gamut (dotted line) is larger than that required by high-definition television standards (dashed line) [2].

Broad spectral tunability also allows a more controlled combination of colors, such that higher-quality white light, with a precisely tailored spectrum, can be generated. The quality of white light can be measured in terms of a correlated color temperature (CCT) and color rendering index (CRI), which compare LED emission with that from the Sun (the 'ideal' white light source, with a CRI of 100). Conventional white LEDs, which comprise a blue inorganic LED backlight coated with a yellow phosphor optical down-converter, typically exhibit a cool bluish emission that is characteristic of high CCTs (> 5,000K) and low CRIs (mostly in the range of 80-85), as shown in Fig.2-2(b). For lower-CCT lights (for example, 2,700 K) it is particularly difficult to maintain high luminous efficiency and high color quality simultaneously because the required red luminophores must have relatively narrow emission spectra to avoid photon loss as infrared emission. The emission spectra of conventional red phosphors

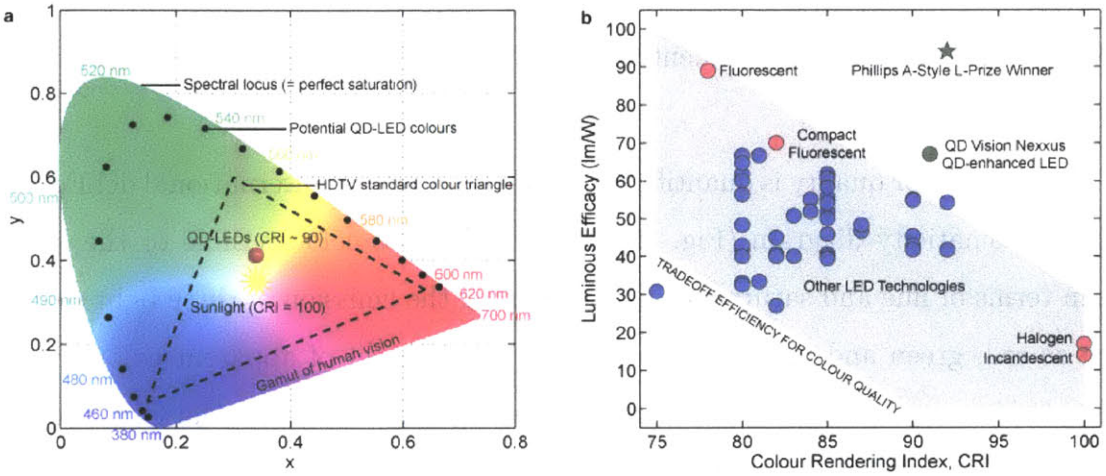

Figure 2-2: Optical advantages of colloidal QDs for display and SSL applications. (a) CIE chromaticity diagram showing that the spectral purity of QDs enables a color gamut (dotted line) larger than the high-definition television (HDTV) standard (dashed line). (b) Plot showing the luminous efficacy and CRI of various commercially available lighting solutions. The first commercial QD-based SSL source, developed by QD Vision and Nexxus Lighting, consists of sheets of red QDs backlit by a blue LED with a yellow phosphor coating, resulting in a high CRI without compromising high luminescence efficacy. Recently, Philips A-Style LED, which employs remote phosphors, has demonstrated even more energy-efficient lighting. There is evidently an emerging market for high-quality optical downconverters, such as QDs.

is unfortunately too broad ($>$ 60nm FWHM) to avoid this loss. In contrast, the narrow spectral emission ($\sim$ 30nm FWHM) of the QDs in QD Vision's Quantum Light offer supplementary and more selective optical down-conversion of some of the backlight's bluer emission (generated by Nexxus Lighting LED light bulbs) into redder light, leading to a CRI of $>$ 90% and a superior CCT of 2,700K while maintaining a very high 65 lm W^{-1} efficacy [2] (see Fig.2-2(b) for a comparison with other LED light sources). QDs therefore enable higher color quality and, accordingly, lower power consumption in SSL sources. Analogous approaches can also be utilized as backlights in high-color-quality liquid-crystal displays, as demonstrated by Nanosys's Quantum Dot Enhancement Film [44].

Bright Emission

Over-coating with wider-bandgap inorganic semiconductor shells (Fig.2-1(b), inset) has been shown to enhance the η_{PL} and photostability of QDs dramatically. This process passivates surface non-radiative recombination sites more effectively than organic ligands alone and shifts the electron wavefunction by confining excitons to the QD core, away from surface trap states [45–47]. For example, solutions of CdSe-ZnS core-shell QDs can be synthesized with a η_{PL} of 30-95% - almost one order of magnitude greater than those of native CdSe cores [4]. Similar improvements in η_{PL} using over-coating have been obtained for NIR-emitting QDs [48].

As QD-LEDs often comprise films of QDs, it is their η_{PL} in this close-packed form that dictates a devices maximum efficiency. For core-only QDs in solution, η_{PL} is typically reduced by one to two orders of magnitude when the QDs are deposited as thin films [49]. Evidence suggests that this self-quenching results from the efficient non-radiative Förster resonant energy transfer (FRET) of excitons within the inhomogeneous size distribution of QDs [50, 51] to non-luminescent sites, where they recombine non-radiatively [42, 52]. It follows from the very strong inter-dot spacing dependence of FRET efficiency (decreasing as spacing increases) that QD ligand length and shell thickness can profoundly impact the degree of QD self-quenching. Thin films of core-shell CdSe-ZnS QDs with long oleic acid ligands, for example, typically retain a η_{PL} of 10-20%, which directly benefits the EQE of QD-LEDs containing those QD films.

The EQE of a QD-LED is defined as the ratio of the number of photons emitted by the LED in the viewing direction to the number of electrons injected. This may be expressed as:

$$EQE = \eta_r \chi \eta_{PL} \eta_{oc} \tag{2.1}$$

where η_r is the fraction of injected charges that form excitons in the QDs, χ is the fraction of these excitons whose states have spin-allowed optical transitions, η_{PL} is the QD PL quantum yield associated with these transitions, and η_{oc} is the fraction of emitted photons that are coupled out of the device. The internal quantum efficiency (IQE) is the efficiency of the charge recombination process, independent of η_{oc} (that is, IQE = EQE/η_{oc}).

It is also technologically significant that $\chi \approx 1$ for CdSe QDs. This value is identical to that of the most efficient organic phosphors used in high-efficiency OLEDs [11]. In CdSe QDs, the high value of χ is a result of the small energetic separation (< 25 meV) of the "bright" and "dark" band-edge excitonic states [53], which have spin-allowed and spin-forbidden transitions to the ground state, respectively. Thermal mixing at room temperature enables efficient crossing of excitons from dark states to higher energy bright states, leading to a high effective χ.

Solution Processable

QD surface ligands confer solubility in a variety of organic solvents. This enables the use of low-cost QD deposition techniques such as spin-coating [6], mist coating [54], inkjet printing [55, 56] and microcontact printing [8, 9]. Ligands can also be chosen [7] (or cross-linked post-deposition [57, 58]) to enable the deposition of subsequent materials in orthogonal solvents.

These methods have led to, for example: organic-QD hybrid structures [59], molecular length-scale control of dot-to-dot separation [60], QDs deposited on curved surfaces [61], QD monolayers [6], QD multilayer superstructures [31], and one-dimensional chains [62].

Stable

It is commonly attested that the photostability of QDs exceeds that of organic chromophores, and that this gives them distinct advantages for applications in LEDs. Yet oxidation in QDs has been seen to cause spectral diffusion (blue-shifting) and PL quenching in both single QDs [63,64] and ensembles of QDs [65]. Exposure to light generally exacerbates these effects through photo-oxidation and photobleaching [64], although substantial photobrightening (increased η_{PL} following exposure to light) has also been observed [66–68]. Beyond the presence of oxygen, these phenomena have been found to be critically dependent on a range of factors, including humidity [69,70], QD film geometry [71] and the duration [65,66], intensity and wavelength [71] of optical illumination.

Nevertheless, QD shells markedly improve photostability [64] by passivating surface traps, confining excitons to QD cores and hindering the diffusion of oxygen, for example, into QD cores. Moreover, thick inorganic multishells [72,73], surface-passivating ligands [74] and radially graded alloyed shells [75] can heavily attenuate and even entirely suppress blinking (PL intermittency) in CdSe QDs. Reductions in blinking are relevant to QD-LEDs because they translate to a higher ensemble η_{PL} [76]. Talapin et al. recently synthesized QDs with inorganic molecular metal chalcogenide ligands [77] and metal-free ionic ligands [78], thereby relieving QDs of instabilities associated with the photodamage of organic ligands [72]. We note that many of the above studies involved single QD spectroscopy at cryogenic temperatures.

Overall, QDs are proving to be more photostable than organic dyes for use as bioanalytical labels [79]. However, whether this holds true for LEDs is yet unclear. Tremendous opportunities exist for improving the longevity of QDs in QD-LEDs by investigating the chemistry and photophysics of films of QDs under operating conditions [80].

2.2 Physics of Quantum Dots

Whereas the last section presented the merits of the QDs for QD-LEDs from an engineer's point of view, this section builds a deeper understanding of the QDs from a physicist's point of view. Understanding the working mechanism of QD-LEDs is essential in making efficient QD-LEDs. At the heart of the device is the QD, a classical 'particle in a box' system rich in physics. The properties arising from this unique system are what makes the QDs attractive for the LED application as described in section 2.1.2. In this section we review the physics that allows us to understand many of the unique properties that these QDs possess.

2.2.1 Cadmium Selenide Semiconductor

Cadmium selenide (CdSe), in wurtzite crystal structure, is the most widely studied semiconductor for colloidal QDs. It is a II-VI semiconductor with a direct band gap energy of 1.73 eV and an exciton Bohr radius of 5.6 nm. When a CdSe nanocrystal is smaller than its Bohr radius, the energy levels of the excitonic states are altered due to the boundary condition that the excitons must satisfy at the surface of the nanocrystal. This effect is schematically shown in Fig. 2-3. In bulk, the semiconductor exhibits a typical energy dispersion curve of a direct band gap semiconductor (Fig. 2-3(a)). For QDs however, of all the states available for the bulk, only the states that satisfy the boundary condition are permitted. These states are indicated in Fig. 2-3(b) as open (filled) circles for electrons (holes). The band gap of the material is then effectively widened by introducing the boundary condition. This effect, known as the quantum confinement effect, allows us to be able to tune the band gap energy anywhere from its bulk value to almost 2.8 eV by simply changing the size of the QD. Quantitative analysis of this confinement effect will be discussed in the next section.

2.2.2 Particle in a Sphere

QDs are often crudely modeled as an electron in a spherical box. This model, although simple, captures many of the essential QD properties. As with any quantum

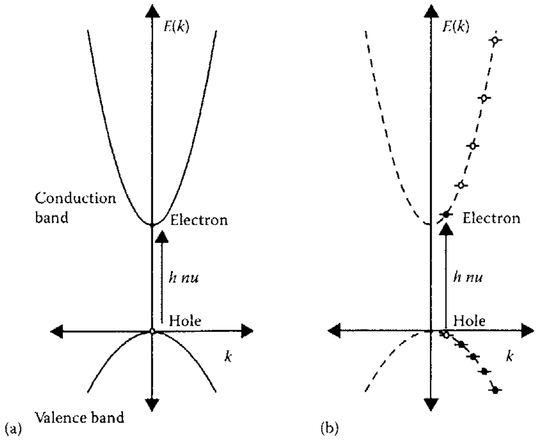

Figure 2-3: (a) An example of an energy band diagram of an direct bandgap semiconductor. (b) For QDs, only the states with k that can satisfy the boundary condition can exist. From ref. [4].

mechanics problem, we start with the time-independent Schrödinger equation to solve for the eigen-energies of the system,

$$E\Psi = H\Psi = \left(\frac{p^2}{2m} + V\right)\Psi. \tag{2.2}$$

The potential energy of an electron in a spherical box with infinite potential barrier is described by:

$$V(r) = \begin{cases} 0 & \text{for} \quad r < a \\ \infty & \text{for} \quad r \geq a \end{cases} \tag{2.3}$$

Since the potential energy, V, is radially symmetric, the differential equation is solved in a spherical coordinate system and we assume the wavefunction is a product of a radial component, $R(r)$, and an angular component, $Y(\theta, \phi)$,

$$\psi(r, \theta, \phi) = R(r)Y(\theta, \phi). \tag{2.4}$$

The solution to the Schrödinger equation, after plugging the wavefunction above into equation 2.2, is given by:

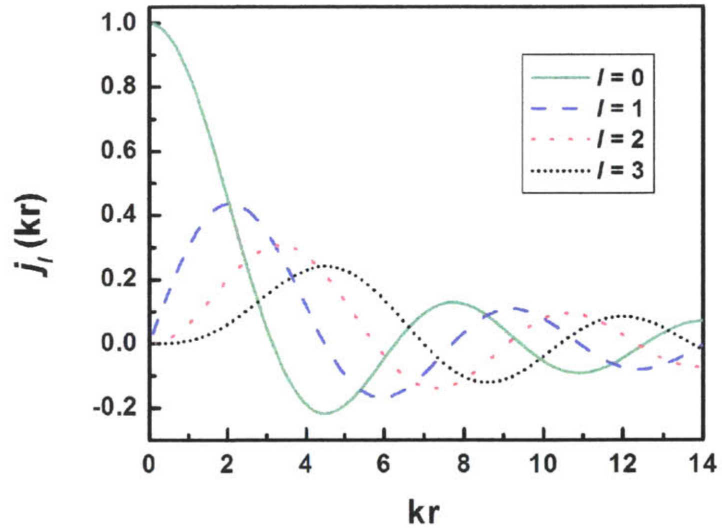

Figure 2-4: The first four spherical Bessel functions with l=0, 1, 2, and 3, corresponding to s, p, d, and f orbitals respectively. To satisfy the boundary condition of a QD, the spherical Bessel function must be zero at the surface of the QD.

$$\psi(r, \theta, \phi) = A j_l(k_{nl} r) Y_l^m(\theta, \phi) \tag{2.5}$$

where A is a constant, j_l is the spherical Bessel function, and Y_l^m is the same angular wavefunction that solves the Schrödinger equation for a hydrogen atom. Interested readers are encouraged to read ref. [81] for a detailed derivation of equation 2.5. Due to the symmetry of the problem, the solutions for particle in a sphere resemble the solutions for the hydrogen problem. Consequently, similarly to atomic orbitals, the *spdf* notation is used to label the different energy states. The first few spherical Bessel functions are shown in Fig. 2-4. To satisfy the boundary condition, the Bessel functions must be zero at the boundary. As a word of caution, one must remember that the spherical Bessel functions alone do not satisfy the Schrödinger equation. The solution must always be a product of the spherical Bessel function and the angular function, $Y_l^m(\theta, \phi)$. The only solution that is truly radially symmetric is the $j_1(r)$, which is an s orbital.

The surface boundary condition requires

$$k_{nl} = \frac{1}{a}\beta_{nl}, \tag{2.6}$$

where β_{nl} is the nth zero of the lth spherical Bessel function shown in Fig. 2-4. The energies of the eigenstates for this system can then be calculated by

$$E_{nl} = \frac{\hbar^2}{2ma^2}\beta_{nl}^2. \tag{2.7}$$

Like the one-dimensional 'particle in a box' problem, the energies are inversely proportional to the square of the box size ($\sim a^{-2}$). We also note that, unlike the hydrogen problem, this system allows the existence of the $1p$ state, which is often observed as one of excitonic features in an absorption spectrum of a QD film.

2.2.3 Excited States of QDs

In this section, we build on the simple model investigated in the previous section to understand the origin of different excitonic states in a QD. The major simplification of the spherical well model is that it overlooks the periodic potential due to atoms that compose the QD crystal. Now we take the model one step closer to a real QD by introducing this periodic potential and discuss its consequences.

We first start with a bulk crystal of CdSe. Bloch's theorem states that for a system with a periodic potential, as is the case for electrons in a crystal, the eigenstates can be written as a product of a periodic function with the same periodicity as the potential, $u_{nk}(\vec{r})$, and a plane wave envelope function, $exp(i\vec{k} \cdot \vec{r})$ (Equation 2.8). Using the tight-binding model, $u_{nk}(\vec{r})$ is often portrayed using superposition of wavefunctions for isolated atoms. Therefore, the index n indicates the different eigenstates of the individual atom. We note that, despite its similarity to a normal plane wave, multiplying $\vec{k}$ in Equation 2.8 by $\hbar$ yields a quantity known as the crystal momentum, which is different from the real momentum.

$$\Psi_{nk}(\vec{r}) = u_{nk}(\vec{r})exp(i\vec{k} \cdot \vec{r}) \tag{2.8}$$

Although CdSe has a hexagonal symmetry (wurtzite crystal structure), the CdSe structure is approximated as diamond-like at $k = 0$ for simplicity. The resulting energies of the eigenstates as a function of k are shown schematically in Fig. 2-3. The conduction band arises from Cd $5s$ orbitals and is two-fold degenerate at $k = 0$. The valence band arises from Se $4p$ orbitals and is, therefore, six-fold degenerate at $k = 0$. However, a real QD has many more features not included in our simple model that lifts this six-fold degeneracy into three separate bands [37]. Notable features include spin-orbital coupling and crystal field splitting. The valence band is composed of three bands, two of which have $p_{3/2}$ (A and B bands) while the third has $p_{1/2}$ (C band). The subscript refers to the angular momentum $J = l + s$, where l is the orbital and s is the spin angular momentum respectively. The spin-orbital coupling splits the C band from A and B bands by 0.42 eV. Furthermore, the crystal field splitting splits the A and B bands by 25 meV. The resulting energy bands are shown in Fig. 2-5.

Near $k = 0$, the conduction and the valence bands can be approximated by parabolas, just like energy of an electron (or a hole) in free space ($E = \hbar^2 k^2/2m$), except these bands have different curvatures due to the periodic potential($u_{nk}(\vec{r})$). If the mass of an electron is "adjusted" such that the curvature of the bands are identical to those of a free electron, the electron in that band can be thought of as a free electron with a different mass called effective mass. In other words, each band can be perfectly described by a free electron (hole) with an unique effective mass. For electrons in the conduction band, this effective mass is $0.11m_0$, where m_0 is the mass of an electron. Holes in the valence bands have $1.14m_0$, $0.31m_0$ and $0.49m_0$ for A, B and C bands respectively [82].

Conceptually, being able to think of electrons and holes in the complicated potential field as free particles simplifies the problem significantly, as will soon become apparent. With the eigenstates of the bulk crystal known, the problem becomes simply a matter of satisfying the boundary condition of a QD. To solve for the wavefunction that meets the boundary condition, we write the QD wavefunction as a superposition of bulk crystal eigenstates:

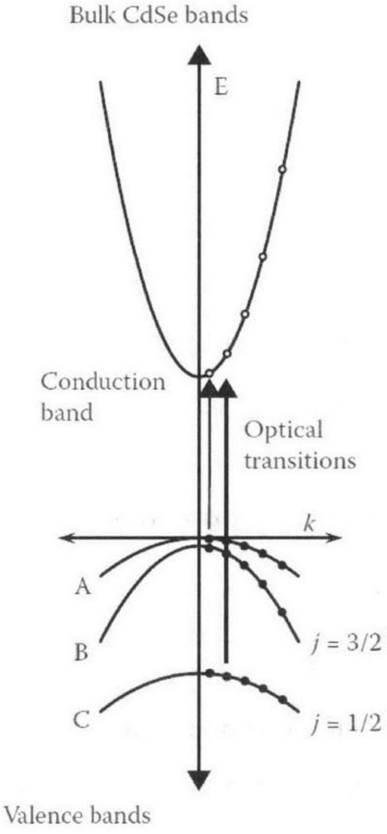

Figure 2-5: Energy band diagram of a CdSe semiconductor. There are three valence bands due to the fact that they originate from Se *p* orbitals. The degeneracy is lifted due to the spin-orbit coupling and the crystal field splitting. From ref. [4].

$$\Psi_{QD}(\vec{r}) = \sum_k C_{nk} u_{nk}(\vec{r}) exp(i\vec{k} \cdot \vec{r}). \tag{2.9}$$

If we assume that $u_{nk}(\vec{r})$ has a weak dependence on $\vec{k}$, the summation can be approximated as

$$\Psi_{QD}(\vec{r}) \approx u_{n0}(\vec{r}) \sum_k C_{nk} exp(i\vec{k} \cdot \vec{r}). \tag{2.10}$$

Therefore, the boundary condition must be satisfied by the summation term. Since the exponentials in the summation are identical to the wavefunction of free electrons (i.e. plane waves), this is exactly the same "particle in a sphere" problem solved in section 2.2.2. Hence, we can immediately infer that the eigenstates of a QD are periodic wavefunction, $u_{nk}(\vec{r})$, enveloped by the spherical Bessel functions.

Invoking equation 2.7, and keeping in mind that an appropriate effective mass must be used to take into account the $u_{nk}(\vec{r})$ component of the wavefunctions, the energy of an exciton in a QD can be expressed as

$$E_{ex} = E_g + \frac{\hbar^2}{2a^2}\left(\frac{\beta^2_{n_e l_e}}{m_e} + \frac{\beta^2_{n_h l_h}}{m_h}\right) - \frac{1.8e^2}{4\pi\epsilon a}, \tag{2.11}$$

where E_g is the bulk bandgap of the QD material, m_e and m_h are the electron and hole effective masses, respectively, and ϵ is the dielectric constant of the QD. The first term indicates that the bandgap is dependent on the material constituting the QD. The second term, called the quantum confinement term, is a function of the QD radius, a, and is the reason that the bandgap of a QD can be tuned by varying the size of the QD. The third term is a correctional term to account for the Coulombic attraction between an electron and a hole (appendix B.3). However, this term becomes less significant for strongly confined excitons since the second term scales as $1/a^2$ while the Coulomb term scales as $1/a$. Interested readers are recommended to read [37] for more details on this topic.

The lowest excited state of a QD is when the electron and the hole are in the $1S_e$ and $1S_{3/2}$ states respectively. This state, written as $1S_e - 1S_{3/2}$, is called the bandedge exciton state and is eight-fold degenerate. The degeneracy is a product of two-fold degenerate electron states and four-fold degenerate hole states. In reality, many of the perturbative effects mentioned earlier lift this eight-fold degeneracy and create an exciton fine structure [83]. Interestingly, the lowest energy exciton state is an optically inactive state, known as the "dark exciton" state, lying below an optically active state, called the "bright exciton" state. The energy difference between the "dark" and the "bright" states depends on the size and the shape of the QD but is generally less than kT at room temperature. Therefore, an exciton in the "dark" state can still be thermally excited to the "bright" state, making QDs efficient phosphors at room temperature.

2.3 Organic Optoelectronics

QD-LEDs were originally motivated from OLEDs and, to this day, share similar device structures, material sets, and even thin film deposition techniques. Therefore, many of the attributes observed in organic opto-electronics are also observed in QD-LEDs. To gain better insight into the operation of QD-LEDs, we provide here a brief review of organic semiconductors and their use in OLEDs.

2.3.1 Organic Semiconductors

Organic molecules are compounds based on a collection of carbon atoms that are covalently bonded together. A carbon has atomic configuration of $1s^2 2s^2 2p^2$, where the last four electrons are valence electrons that can form σ and π bonds with other atoms. When the neighboring carbon-carbon bond alternate between single and double bonds, the molecule is said to be *conjugated* and exhibit semiconducting properties. In contrast, molecules where all the carbon-carbon bonds are single bonds are said to be *saturated* and generally exhibit insulating properties. Organic solids are held together by van der Waals interactions, which are relatively weak. These weak bondings result in localization of electronic states to individual molecules.

As an example, benzene, which is a building block for many organic semiconductors, is a molecule with six carbon atoms in a ring configuration shown in Fig. 2-6. Each carbon uses three valence electrons in sp^2 orbitals (hybridized state of $2s$, $2p_x$, and $2p_y$ orbitals) to form σ bonds to two neighboring carbon atoms and a hydrogen. The fourth valence electron of each carbon atom resides in the unhybridized $2p_z$ orbital. Neighboring $2p_z$ orbitals overlap, forming π bonds while also forming a cloud of electrons, above and below the plane of the molecule, called delocalized π orbital. Fig. 2-6(b) shows the chemical structure of a benzene ring with the alternating single and double bonds. The double bonds consists of a σ bond and a π bond. In case of a conjugated molecule, the valence electrons not contributing to the σ bonds fill half of the states available by the delocalized π orbitals. The highest occupied molecular orbital (HOMO) is a π orbital and the lowest unoccupied molecular orbital (LUMO) is an excited configuration of the π orbitals, labeled π^* state (Fig. 2-6(c)). Therefore, the lowest energy transition is a $\pi \rightarrow \pi^*$ transition [84].

Just like QDs, a bigger conjugated molecule generally exhibits greater delocalization of the π electrons, reducing the confinement effect and, therefore, the bandgap of the molecule. This simple particle in a box approach shows that the bandgap energy can be reduced to visible spectral region with about seven repeating units [84]. The delocalization and the out-of-plane geometry of the π electron cloud, which assist with electron hopping between molecules, help the electrical conductivity of these organic semiconductors.

Organic semiconductors that are of interest to us generally fall under two broad categories: aromatic hydrocarbons and conjugated polymers. Aromatic hydrocarbons are carbon-hydrogen compounds containing benzene rings. Conjugated polymers are polymers (long-chain molecule with repeating sequences of monomer units) with conjugated backbones. Most of the organic semiconductors used in this thesis fall under the first category. For example, the hole transporting layer materials, CBP and TCTA, are both aromatic hydrocarbons. As shown in Fig. 2-7, they both possess a number of benzene rings in their structures.

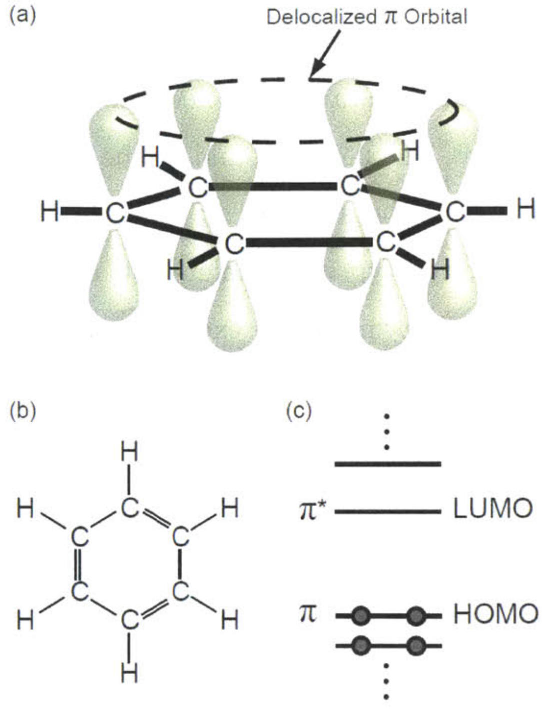

Figure 2-6: (a) Schematic of a benzene ring. Each carbon atom has sp^2 hybridized orbitals, forming σ bonds with two neighboring carbons and a hydrogen, and a p_z orbital protruding out of the plane of the molecule. Neighboring p_z orbitals weakly overlap, forming π bonds, and results in delocalization of electrons over the π orbital. (b) Chemical structure of the benzene ring showing conjugated bonds. (c) Energy band diagram of the benzene ring showing HOMO and LUMO. The electrons fill half of the π orbital states [courtesy of Tim Osedach].

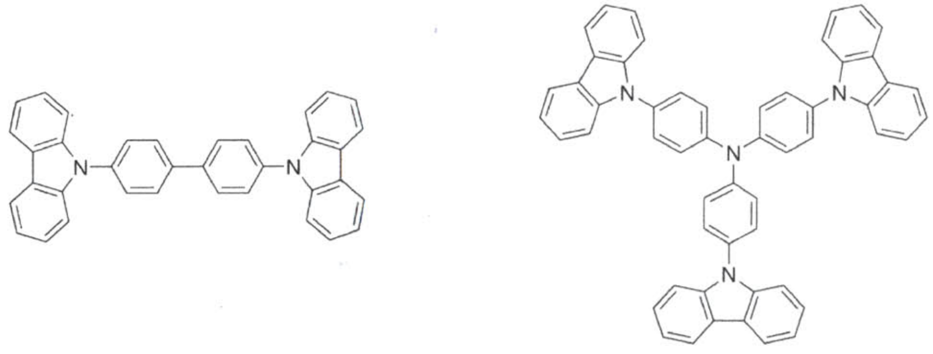

CBP **TCTA**

Figure 2-7: Chemical structures of CBP and TCTA.

2.3.2 Excitons

As mentioned earlier, an exciton is a bound electron-hole pair that can be formed either optically or electrically. The pair is bound by the Coulomb interaction between the electron and the hole and the strength of the interaction determines its size. Excitons are categorized into two types: Wannier-Mott excitons and Frenkel excitons. Wannier-Mott excitons, also known as free excitons, are excitons often observed in inorganic semiconductors. Since these materials have high dielectric constants ($\epsilon_r > 10$), the Coulomb interaction is weak due to screening. As a result, these excitons are large, extending over many atoms (Fig. 2-8(a)), and have low binding energies (~ 0.01 eV). Therefore, these excitons are generally not observable at room temperature.

Frenkel excitons, also known as tightly bound excitons, are excitons often observed in organic molecules. Organic materials have a low dielectric constant ($\epsilon_r \approx 3$), resulting in strong Coulomb interaction. The excitons are localized to individual molecules (Fig. 2-8(b)) and have high binding energies (0.1-1 eV), which make them observable even at room temperature.

We note that excitons in QDs are slightly different in nature from the above two excitons. While the above two kinds of excitons are held together by the Coulomb interaction, excitons in QDs are generally bound by the physical confinement due to the potential well. This is clear by looking at equation 2.11. As the radius gets smaller, the kinetic energy of the charge carrier (second term) gets larger than the Coulomb interaction energy (third term).

2.3.3 Organic Light-Emitting Diodes

The first successful OLED was demonstrated by Tang *et al.* in the late 1980s [85]. The device structure consisted of an aromatic hydrocarbon ETL-HTL bilayer sandwiched between ITO and silver electrodes. The turn-on voltage was below 4 V and the efficiency was EQE $\approx$ 1%. This promising result started the field of OLEDs.

The efficiencies of these early OLEDs were limited due to the fluorescent nature of the organic emitters used. When excitons are electrically excited in an OLED,

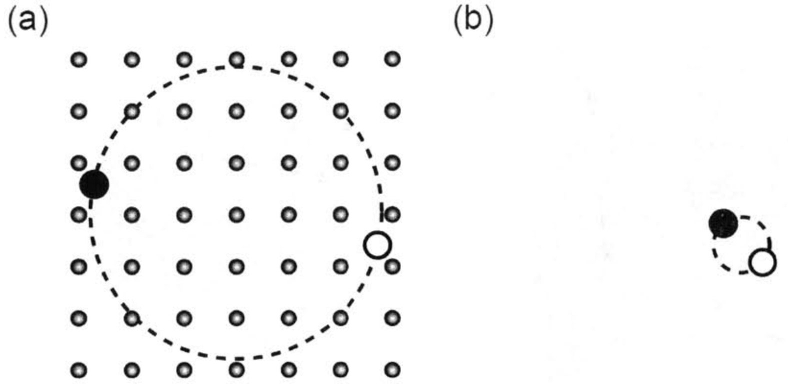

Figure 2-8: (a) Wannier-Mott exciton in a crystal lattice. (b) Frenkel exciton tightly bound to a single molecule [courtesy of Tim Osedach].

statistically, only 25% of them are singlets and the rest are triplets. Singlet excitons have spin asymmetry while triplet excitons have spin symmetry. Therefore, without spin-orbit coupling, the Pauli exclusion principle inhibits these triplet excitons from emitting photons and relaxing to their ground states.

A breakthrough came in the late 1990s when Baldo *et al.* demonstrated the use of phosphorescent organic molecules as efficient emitters in OLEDs [11,86]. A phosphorescent organic molecule has a heavy metal center that causes spin-orbit coupling. Hence, triplet excitons acquire some singlet characteristics, allowing them to relax to their ground states and emit photons. With phosphors, any electrically formed excitons are permitted to emit photons and efficiencies of these devices reached EQE $\approx 8\%$.

With much improved efficiencies and stabilities today, OLEDs have become a proven technology used for many smartphone displays (such as the Samsung Galaxy S series). In many ways, QD-LEDs are an extension of these earlier works. Although incorporating inorganic semiconductor nanocrystals into these structures comes with new material instability and incompatibility issues, it also comes with hopes of achieving many attributes that are not realizable with organics alone. Many of these attributes are discussed in sections 2.1.2 and 2.4.2.

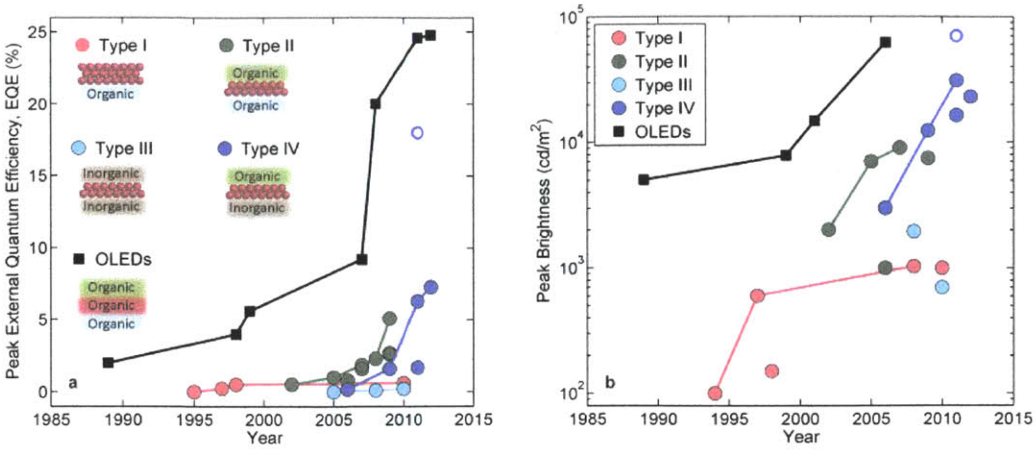

Figure 2-9: Progression of orange/red-emitting QD-LED performance over time in terms of peak EQE and peak brightness. (a) Peak EQE. (b) Peak brightness. QD-LEDs (a substantial but non-exhaustive selection from the literature) are classified into one of four types, as described in the text, and are compared with selected orange/red-emitting (phosphorescent) OLEDs. Solid lines connect new record values. [5]

2.4 Quantum-Dot Light-Emitting Devices

2.4.1 Evolution of QD-LEDs

The performance of electrically driven colloidal QD-LEDs has improved dramatically since their invention in 1994. Fig. 2-9 summarizes this progress for the case of orange/red-emitting (almost always CdSe-based) QD-LEDs in terms of two metrics: peak EQE (Fig. 2-9(a)); and peak brightness (Fig.2-9(b)). (We note that QD Vision recently reported EQEs of up to 18% [87, 88], and that Kwak *et al.* demonstrated green-emitting QD-LEDs with a maximum brightness of 218,800 cd m^{-2} [12]). EQE is directly proportional to power conversion efficiency — a key metric for SSL and displays — and brightness values of $10^3 - 10^4$ cd m^{-2} and $10^2 - 10^3$ cd m^{-2} are required for SSL and display applications, respectively. Fig. 2-9 classifies reported QD-LEDs into one of four architecture types, which are described in the following sections. It can be seen that these four types have evolved nearly chronologically. Despite the scattered data, the trend is a steady increase in both EQE and brightness, with values approaching those of phosphorescent OLEDs (black squares).

Type I: QD-LEDs with polymer charge transport layers

Pioneered in the early 1990s, these devices are the earliest QD-LEDs and have structures similar to polymer LEDs. Original devices comprised a CdSe core-only QD-polymer bilayer or blend [22, 89] sandwiched between two electrodes. QD EL was achieved but at extremely low EQEs (<0.01% at around 100 cd m^{-2}), partly due to the low η_{PL} of QDs without shells (10% in solution). The low brightness was a consequence of the very low current densities achievable while using insulating QDs as both charge transport and emissive materials. Core-shell CdSe QDs were later employed in type-I structures to take advantage of their higher η_{PL} [90], and EQEs of up to 0.22% (maximum of 600 cd m^{-2}) were reported using CdS shells [91]. However, these devices still exhibited significant parasitic polymer EL, which is indicative of inefficient exciton formation in QDs.

In these initial QD-LEDs, QD EL was speculated to be driven by direct charge injection (Fig.2-10(b)), FRET (Fig.2-10(c); see also appendix B.1), or both. In the case of direct charge injection, an electron and a hole are injected from charge transport layers (CTLs) into a QD, forming an exciton that subsequently recombines to emit a photon. FRET is also a viable mechanism that is unique to devices with luminophores, such as emissive polymers [92], small molecule organics [93] or inorganic semiconductors [94, 95], in close proximity to the QDs. In this scheme, an exciton is first formed on the luminophores. The excitons energy is then non-radiatively transferred to a QD through dipole-dipole coupling. The relative contribution of these mechanisms remains unclear in all four types of QD-LEDs, and a better understanding of their roles, for example as a function of QD-LED architecture, will be essential in designing more efficient and brighter devices.

Type II: QD-LEDs with organic small molecule charge transport layers

In 2002, Coe *et al.* introduced type-II QD-LEDs consisting of a monolayer of QDs at the interface of a bilayer OLED (Fig.2-11) [23]. These devices demonstrated a record EQE of 0.5%. The enhanced efficiency was attributed to the use of a monolayer

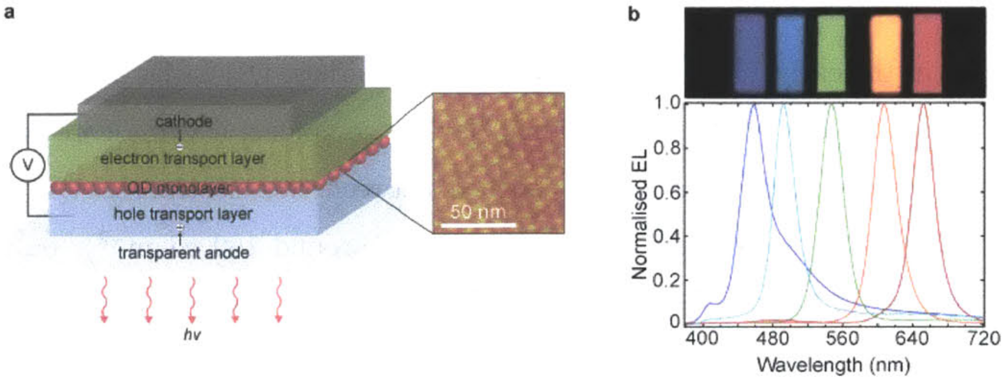

Figure 2-10: Type-II QD-LED. (a) The prototypical type-II QD-LED structure, comprising a monolayer of QDs sandwiched between an organic hole-transport layer (HTL) and an organic electron-transport layer (ETL) [6]. Its corresponding energy band diagram is shown in Fig. 2-10(e). Inset: an atomic force microscope image of a monolayer of QDs on an organic HTL. (b) Photographs of EL from type-II QD-LEDs with varying QD compositions and their respective emission spectra [1].

of QDs, which decoupled the luminescence process from charge transport through the organic layers [23, 93, 96, 97]. This work also introduced a procedure by which to form a self-assembled monolayer of QDs at the organic interface: when a blend solution of QDs and charge transporting organic molecules are spin-cast together, phase separation causes the spontaneous formation of a QD monolayer on top of a film of the organic molecules (Fig.2-11(a), inset).

Consequently, the fabrication and patterning of a closely packed QD monolayer became important to enhance the efficiency and practicality of type-II QD-LEDs. One alternative to the above approach is microcontact printing. In this method, a monolayer of QDs is spin-cast onto a poly(dimethylsiloxane) (PDMS) stamp, which, after drying, is brought into contact with a substrate, resulting in the transfer of QDs from the stamp to the substrate (Fig.2-12(b)) [8, 96, 98]. Microcontact printing has the benefit of avoiding exposure of the underlying organic to solvents during QD deposition. QD-LEDs fabricated using microcontact printing yield higher efficiencies than those employing phase-separation because the QDs are partially embedded in the underlying organic layer during stamping [93]. Placing the QD monolayer a few nanometers away from the organic interface is thought to result in reduced QD

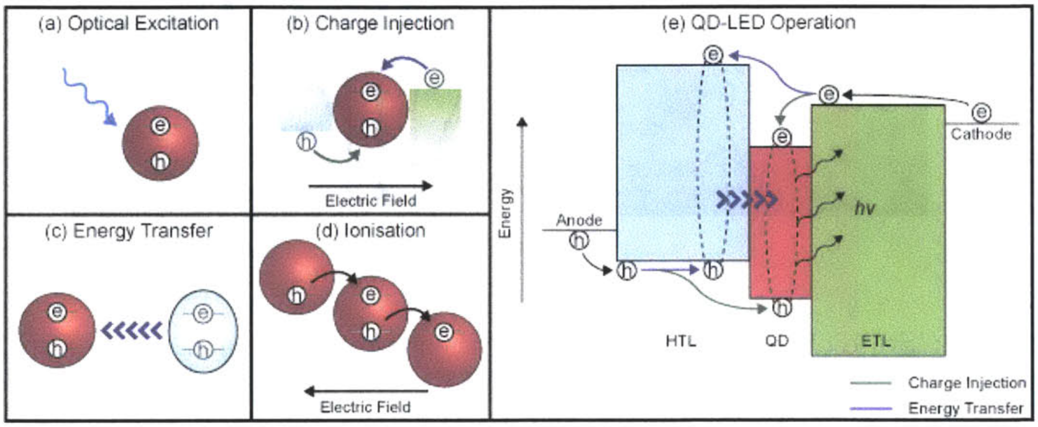

Figure 2-11: QD excitation mechanisms.There are four routes for generating excitons in QDs that have been used in QD-LEDs. (a) Optical excitation: an exciton is formed in a QD by absorbing a high-energy photon. (b) Charge injection: an exciton is formed by injection of an electron and a hole from neighboring CTLs. (c) Energy transfer: an exciton is transferred to a QD via FRET from a nearby donor molecule. (d) Ionization: a large electric field ionizes an electron from one QD to another, thereby generating a hole. When these ionization events occur throughout a QD film, generated electrons and holes can meet on the same QD to form excitons. (e) Energy band diagram of a typical type-ii QD-LED that outlines the two suspected QD excitation mechanisms: charge injection and energy transfer.

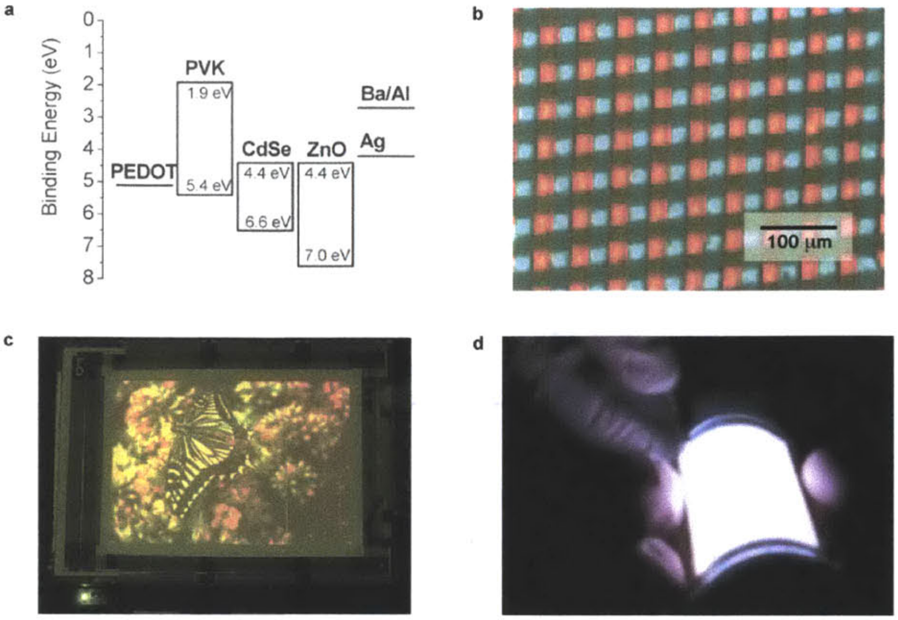

Figure 2-12: State-of-the-art QD-LEDs and their use in large-area devices. (a) Energy band diagram of the first type-iv QD-LED employing ZnO [7]; the electron transport layer of choice in todays high-performance devices; PEDOT, poly(3,4-ethylenedioxythiophene); PVK, poly-N-vinyl carbazole. (b) The first demonstration of red-green-blue EL from (type-ii) QD-LED pixels, patterned using microcontact printing [8]. (c) This technique has been harnessed to produce a 4-inch full-color active matrix type-iv QD-LED display [9]. (d) Flexible white-emitting type-ii QD-LED [10].

charging and an electric field across the QDs [97], both of which can decrease the EQE by reducing η_{PL} [15,99].

Using microcontact printing, Anikeeva *et al.* demonstrated a series of QD-LEDs whose emission could be tuned across the entire visible spectrum by varying the composition of QDs sandwiched between two organic CTLs (Fig.2-11(b)) [1]. A maximum EQE of 2.7% was achieved for orange emission. The spectral purity and tunability of the QD-LEDs reported in this work clearly demonstrate the potential of QD-LEDs for use in EL displays. It has also been demonstrated that white-light-emitting QD-LEDs can be fabricated by mixing different compositions [100] or sizes [101] of QDs. A CRI of 86 was achieved by mixing red, green, and blue QDs. As shown in Fig.2-2(a), even higher CRIs should be achievable by mixing a greater variety of QD colors, which suggests that white QD-LEDs could be realized for use as SSL sources. Furthermore, compatibility of type II QD-LEDs with flexible substrates is exemplified by the flexible white-light-emitting QD-LED shown in Fig.2-12(d).

Studies in our group have indicated that FRET is the dominant QD excitation mechanism [97], at least in certain type-II QD-LED geometries. Yet, the achievement of EQEs reaching $> 2\%$ in QD monolayer-based devices comprising organic donor materials with very low η_{PL} [102] challenges the universality of the FRET model.

Combining an OLED architecture with a monolayer of QDs was nevertheless a significant step forwards in demonstrating efficient QD-LEDs. These devices boast all the advantages of OLEDs while providing the added benefits of enhanced spectral purity and tunability. However, the use of organic layers introduces device instabilities upon exposure to air [103, 104]. As with OLEDs, commercialized QD-LEDs would then require protective encapsulation, which adds to manufacturing costs and hinders applications such as flexible technologies. Furthermore, the relatively insulating nature of organic semiconductors can limit the current densities achievable in QD-LEDs prior to device failure, therefore limiting their brightness.

Type III: QD-LEDs with inorganic charge transport layers

Replacing the organic CTLs of type-II QD-LEDs with inorganic CTLs could lead to greater device stability in air, and could enable the passage of higher current densities. One such all-inorganic QD-LED (apart from organic ligands) was made by Mueller *et al.*, who sandwiched a monolayer of QDs between epitaxially grown n- and p-type GaN [24]. They observed QD EL, although at very limited efficiencies (EQE of $< 0.01\%$). The epitaxial growth of GaN, however, diminishes the advantage of using colloidal QDs to inexpensively fabricate large-area devices. This necessitates alternative approaches for developing QD-LEDs with inorganic CTLs.

One such alternative is the use of sputtered metal oxides as CTLs. Like organic materials, metal oxide and chalcogenide thin films can be deposited at room temperature by sputtering. The broad variety of metal oxide and chalcogenide compositions enables their energy bands to be fine-tuned, as required for the optimal operation of QD-LEDs. In addition, metal oxides can be more conductive than their organic counterparts, and the conductivity of metal oxides is tunable by controlling oxygen partial pressure during thin-film growth. Caruge *et.al.* applied this technique in QD-LEDs comprising zinc tin oxide and NiO as n- and p-type CTLs, respectively [105]. As expected, these devices were able to pass higher current densities (up to 4 A cm^{-2}) but with an EQE of $< 0.1\%$.

This inefficiency was attributed to the damage of QDs during sputtering of the overlying oxide layer, carrier imbalance (due to a large hole injection barrier between the p-type metal oxide and the QDs), and quenching of QD PL by the surrounding conductive metal oxide [106]. To our knowledge, a type-III QD-LED has not yet been developed with efficiencies comparable to those of type-II devices.

Over the past few years, a category of all-inorganic QD EL device that operates by an altogether different excitation mechanism has emerged. These devices are capacitive structures consisting of two contacts sandwiching a film of dielectric material, with a layer of QDs at its center [107, 108]. High AC voltages drive these devices, resulting in operation by electric-field-assisted ionization of QDs to generate free carriers (Fig.2-10(d)). This architecture eliminates the need for CTLs and energy band alignment between different semiconductors. Although their brightness is limited ($\sim 10^{-3}$ lm W^{-1}), these devices demonstrate an alternative way to electrically excite QDs and offer a unique testbed with which to study the effect of electric fields on QDs [109].

Type IV: QD-LEDs with hybrid organic-inorganic charge transport layers

As a compromise between type-II and type-III QD-LEDs, recent attention has been focused on type-IV QD-LED hybrid architectures comprising both organic and inorganic CTLs. One layer, typically the n-type semiconductor, is a metal oxide, while the other is an organic semiconductor (Fig.2-12(a)). Although this type of structure is not new to the field [7, 110], it is only recently that these devices have gained attention, due to their high EQEs and high brightnesses. QD Vision recently reported an QD-LED with 18% EQE [87] using this hybrid structure, which greatly surpassed previous efficiencies. Type-IV devices can also be solution-processed using colloidal metal oxide nanoparticles as the electron transport layer [12,39]. In particular, Qian *et al.* have demonstrated red, green and blue solution-processed (excluding electrodes) QD-LEDs. The EQEs of these devices were 1.7%, 1.8% and 0.22%, with maximum brightness values of 31,000 cd m^{-2}, 68,000 cd m^{-2} and 4,200 cd m^{-2} for red, green and blue devices, respectively. These brightness values are among the highest reported so far.

Recently, using similar type-IV hybrid structures, a full color 4-inch QD-LED display (Fig.2-12(c)) has also been reported [9]. In pixelated display structures, QDs are patterned by microcontact printing (Fig.2-12(b)) with a resolution of up to 1,000 pixels per inch (25 μm features) [8], which provides a striking demonstration of the feasibility of using QD-LEDs in display applications.

The energy-transfer scheme that is suspected to dominate QD excitation in type-II QD-LEDs requires migration of one carrier type through the close-packed QDs of a monolayer film, so as to form excitons in an adjacent donor material (Fig.2-10(e)) [97]. Because type-III and type-IV QD-LEDs, in contrast with type-II QD-LEDs, employ QD films that are thicker than one monolayer (up to $\sim$ 50 nm), the working mechanism of type-IV QD-LEDs is more likely reliant on charge injection than on energy transfer.

2.4.2 Novel QD-LEDs

Near-Infrared (NIR) QD-LEDs

In recent years, there has been a push to extend the EL of both QD-LEDs and organic-based LEDs from the visible into the NIR range (780 - 2,500 nm). At wavelengths of up to $\sim$ 800 nm, OLEDs and polymer LEDs have exhibited EQEs as high as 6.3% [111, 112], although beyond 1 μm efficiencies are much lower ($<$ 0.3%) [113]. This is largely due to the paucity of high-η_{PL} NIR molecular and polymeric dyes, even when modified with heavy-metal atoms [112].

In contrast, the PL and EL of QDs are readily tunable throughout the NIR range, resulting in EQEs of up to $\sim 2\%$ [41]. In our laboratory we have recently realized devices with efficiencies exceeding 4% [114]. NIR QD-LEDs have the potential for use in military applications, including night-vision-readable displays [111] and friend/foe identification systems [115]. In addition, deep-tissue biomedical imaging and optical diagnosis for biological transparency windows in the range of 800-1,700 nm [116] are also compatible with tunable NIR QD emission [29]. We envision, for example, low-cost NIR QD-LEDs in microfluidic point-of-care devices [117]. It has been frequently proposed that solution-processable sources of EL in the 1.3-1.55 μm telecommunications band could be integrated into complementary metal-oxide semiconductor silicon electronics, thus finding applications in on-chip, chip-to-chip, fiber-optic and free-space optical communications [42, 118–121]. As a word of caution, however, we note that many such applications would require gigahertz response rates, which are far greater than the typical megahertz rates of QD-LEDs [118, 122].

Extension of the wet chemical methods discussed above has enabled the synthesis of a variety of efficient NIR-emitting colloidal QDs, which, in the telecommunications band, include PbE (where E=S, Se or Te), InAs and HgTe, as well as core-shell QDs such as PbE-CdS and InAs-ZnSe. In many cases, high η_{PL} ($> 50\%$) have been achieved. There are a number of in-depth reviews (see refs. [4, 118, 123, 124]) for the interested reader. As discussed in the next section, NIR emission from silicon QDs has also been observed [125].

The majority of NIR QD-LEDs have evolved directly from polymer LEDs and are of type-I architecture with a hole-transporting conjugated polymer, most commonly a derivative of polyphenylenevinylene (PPV). The earliest NIR QD-LED, reported by Banin *et al.*, was based on core-shell InAsZnSe QDs in a poly[2-methoxy-5-(2-ethylhexyloxy)-1,4-phenylenevinylene] (MEH-PPV) polymer blend and had an EQE of 0.5% [126]. Tunable EL centered at around 1.3 μm was observed, although the turn-on voltage exceeded 15 V. Subsequently reported NIR QD-LEDs have almost exclusively employed core-only PbS [119, 127] and PbSe [121, 128] QDs, with record EQEs of 2% [41] and 0.83% [121], respectively. Turn-on voltages have been reduced to ~ 1 V [119]. Recently, Holmes *et al.* described the first silicon QD-based LEDs (type-II architectures were employed), which emitted NIR EL at around 850 nm and displayed very high EQEs of up to 8.6% [125, 129]. Just as with visible-wavelength QD-LEDs, it has been argued that electrical excitation of QDs in these NIR devices occurs either by FRET [42,120] or direct charge injection [119,121,129–131]; a balance between the two is likely in most cases.

The optical tunability of high-brightness QDs throughout the NIR region is a major advantage over their organic dye counterparts, and the variety of potential applications compels further investigation. Despite their infancy, the EQEs of NIR QD-LEDs are already comparable with those of visible-wavelength-emitting QD-LEDs, perhaps because their smaller bandgaps are more amenable to efficient electrical excitation [125]. Improvements in thin-film NIR QD η_{PL} will enable the evolution of a more diverse range of NIR QD-LED architectures.

Heavy-metal-free QD-LEDs

The QD-LEDs discussed so far rely on the use of heavy-metal cations such as cadmium, lead and mercury, which make up the core or shell (often both) of colloidal QDs. However, there are growing concerns regarding the risks that these materials pose to our health and to the environment. The European Unions Restriction of Hazardous Substances Directive, for example, severely limits the use of these materials in consumer electronics. The likelihood of commercial success for QD-LEDs will therefore be greatly increased if these devices can be fabricated using heavy-metal-free QDs. There have already been a few demonstrations of QD-LEDs based on cadmium-free QDs — for example, red and green QD-LEDs with ZnCuInS QDs [132, 133] — albeit at low efficiencies.

Another approach to making heavy-metal-free QD-LEDs is to use silicon QDs. Silicon is both non-toxic and naturally abundant, yet bulk silicon, the cornerstone of modern electronics, is an indirect-bandgap semiconductor with low η_{PL} and is therefore not used as an emitter in today's LEDs. Silicon QDs may provide a means of addressing the dearth of luminescent excitons that exist in bulk silicon at room temperature. As a silicon crystal gets smaller, the loss of translational symmetry relaxes momentum conservation and band-edge emission becomes increasingly efficient [134]. Silicon QDs with diameters of less than 5 nm can effectively confine excitons and exhibit high η_{PL} (40-60% in solution [135]). In addition, similarly to CdSe QDs, the emission energy of silicon QDs can be tuned from 1.1 eV (bulk bandgap) to 3.0 eV (2 nm diameter QDs) by changing the size of the QDs. One of the earliest reported silicon QD-LEDs featured silicon QDs synthesized from the electrochemical etching of silicon wafers and embedded in a polymer matrix [136]. Such devices exhibited EL but also suffered from concomitant polymer emission. More recently, non-thermal plasma has been used to synthesize silicon QDs [137], and NIR EL with EQEs as high as 8.6% have been achieved [125].

These demonstrations of heavy-metal-free QD-LEDs show both good color tunability and increasingly competitive efficiencies. Some of the main challenges are the development of efficient visible-wavelength (especially blue and green) emitters, and the achievement of higher brightnesses. In terms of both QD synthesis and QD-LED engineering, the need for non-toxic QD-LEDs makes this an exciting field that will likely benefit from the improvements of CdSe QD-LEDs seen in recent years.

Chapter 3

QD-LED Fabrication and Testing

This chapter introduces standard fabrication and testing procedures of QD-LEDs. Like fabrication of any other thin film optoelectronic devices that contain materials sensitive to O_2 and H_2O (e.g. organic materials and QDs), the fabrication must take place in an inert environment. This environment is usually a high vacuum chamber or a glove box filled with N_2. All of the devices used in this thesis were fabricated at the Organic and Nanostructured Electronics Laboratory (ONE Lab) shown in Fig. 3-1. There is a "wet" glove box where solution processing is performed, connected to a "dry" glove box where the samples are prepared to be loaded into the load lock. The load lock connects the dry box with a centralized vacuum system, which allows transfer of samples without exposing them to air. The centralized vacuum system is maintained at high vacuum ($\sim 10^{-6}$ Torr) and there is a pulley system within that allows transfer of the samples to any of the thin-film deposition equipments attached to the system. There is a testing glove box on the far end to perform standard efficiency testing of the LEDs.

3.1 Fabrication Methods

QD-LEDs, like many other thin-film optoelectronic devices, requires succession of thin film depositions so as to build a multi-layer structure. Each layer is $1 \sim 100$ nm thick and the entire device is only a few hundred nanometers thick. The deposition method

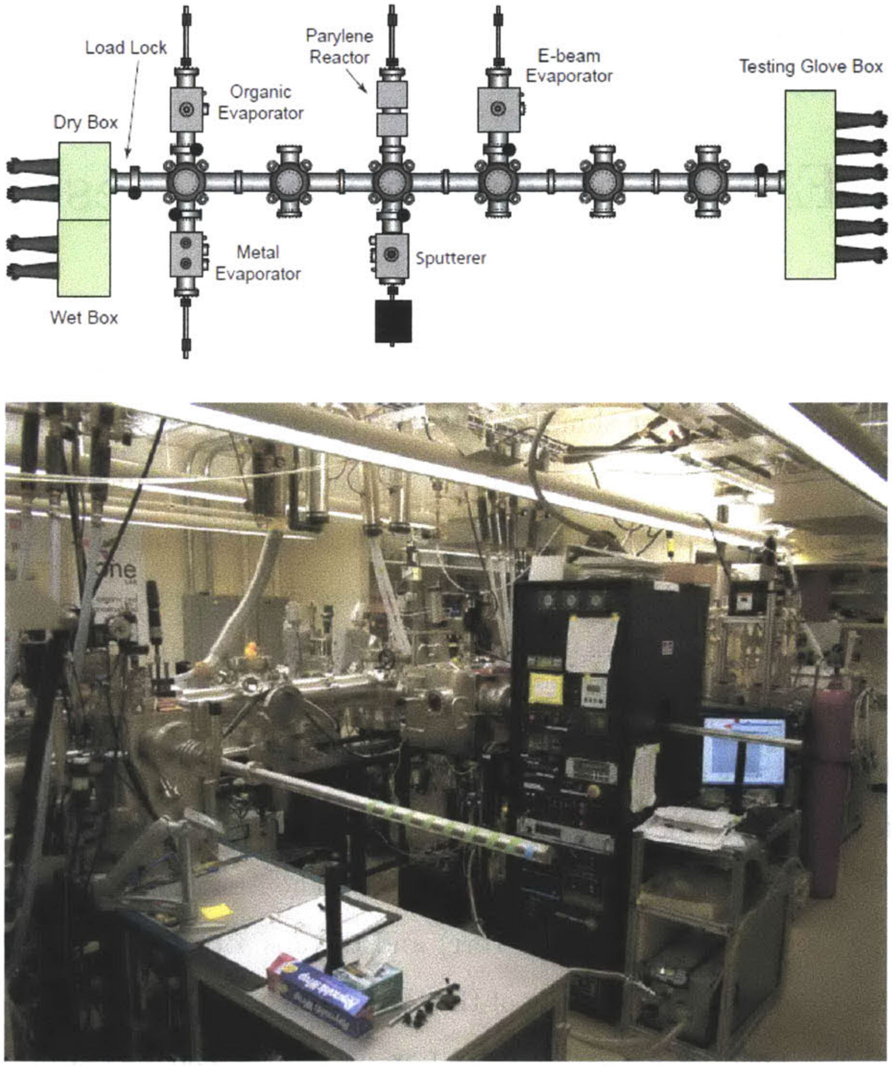

Figure 3-1: Diagram and a picture of the Organic and Nanostructured Electronics Laboratory (ONE Lab) where most of the device fabrication is performed. [Courtesy of Tim Osedach]

for each layer depends on many factors, including the material being deposited and the materials of the underlying layers. We briefly describe here the techniques most commonly used to fabricate a QD-LED.

3.1.1 Solution Processing

Solution processing is a set of techniques that dissolve the material of interest into a solution before processing it into a film on a substrate. It is considered a versatile thin-film deposition technique that can be performed at a low cost, one of the main driving forces behind thin-film optoelectronic devices. Here we briefly describe a solution-processing technique that is used extensively in this thesis: spin-coating.

Spin Coating

Spin-coating is a technique that involves dispensing a solution with the desired material onto a substrate and then rotating the substrate. Rotating the substrate distributes the solution across the substrate, leaving a uniform film of the material as the solvent evaporates off during the rotation. The thickness of the film depends on many factors including the kind of solvent, the rotation speed of the substrate, and the concentration of the solution. The boiling points of typical organic solvents ranges from 61°C (chloroform) to 131°C (chlorobenzene). Different boiling points affect the evaporation rate of the solvent and, in turn, result in different film thickness as well as morphology. The rotation speed affects the spreading of the solution on the substrate, with higher speed resulting in thinner films. However, it is not easy to control the thickness of the film by the choice of solvent or the rotation speed. Instead, the thickness is generally controlled by changing the concentration of the solution since the film thickness scales proportionally with the concentration.

The spin-coating method can be used for any QDs with proper ligand coating, small molecule organics, or polymers that can be dissolved into a solvent. The usefulness of this method is in its simplicity and applicability to many materials. However, there are many limitations to the technique. For a multilayer structure, the use of solvent requires the underlying layer to be stable against the solvent so the underlying layers are not washed off as the top layer is spun on. Thickness of the spin-coated films are not as well controlled as some of the other techniques. The spinning of the substrate also limits its applications to relatively small substrates.

3.1.2 Physical Vapor Deposition

Physical vapor deposition (PVD) allows for the deposition of many of the materials that are not solution processable, such as metals and metal oxides. This technique is a vacuum deposition method and produces a film by vaporizing the material and subsequently allowing it to condense onto a substrate. In general, PVD offers better control over the film thickness than solution processing. However, PVD cannot be used for some materials like QDs, and the plasma required to vaporize high melting point materials can be detrimental to the materials in the underlying layers. We briefly mention here two kinds of PVD techniques: thermal evaporation and sputtering.

Thermal Evaporation

Thermal evaporation vaporizes the material by simply heating the material and evaporating (or subliming) it onto a substrate. A schematic and a picture of a thermal evaporator is shown in Fig. 3-2. It consists of a vacuum chamber ($\sim 10^{-6}$ Torr) with tungsten crucibles that hold the materials (in a form of powder or pellets) and a rotating substrate holder. External power supplies deliver AC current to the crucibles to heat the crucibles and the materials inside. The rate of deposition can be controlled by adjusting the power supplied to the crucibles and that rate is monitored using a quartz crystal thickness monitor that resides inside the chamber. Typical deposition rate is ~ 1 Å, giving nanometer precision for film thickness. While thermal evaporation is a useful technique, some of its limitations include not being able to deposit QDs and other materials that have high sublimation temperatures like polymers.

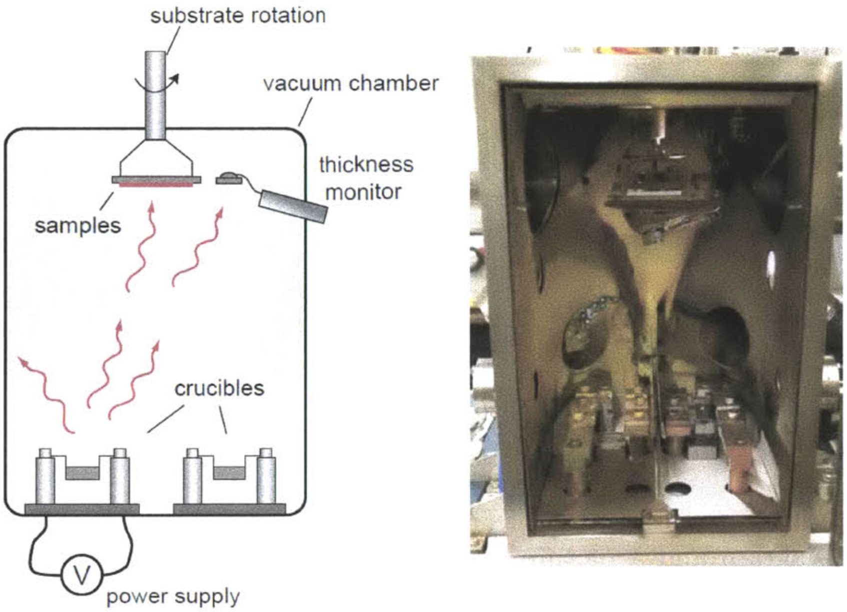

Figure 3-2: Diagram and a picture of the thermal evaporator used in ONE Lab [Courtesy of Tim Osedach].

RF Magnetron Sputtering

RF sputtering deposits a film by bombarding ionized inert gas (typically Ar) into a disk of the desired material, called a "target", which consequently ejects atoms of the target onto a substrate positioned nearby. The setup of the system, shown in Fig. 3-3 is identical to the thermal evaporator except the crucibles are replaced with sputtering guns and the chamber pressure is typically ~ 10 mTorr. The sputtering guns consist of two electrodes (an RF electrode and a grounded shield) and two magnets (a center magnet and a ring magnet). The electrodes form the electric field to ionize the gas and form a plasma, while the magnets form the magnetic field to localize the plasma over the target.

Sputtering allows for deposition of materials with high boiling points that can not be evaporated like metals and metal-oxides. If the material being sputtered is insulating, then the surface of the target becomes positively charged over time as the cathode attracts the ionized Ar atoms. These accumulated positive charges screen the cathode potential, reducing the sputtering rate. To avoid this charging, the applied

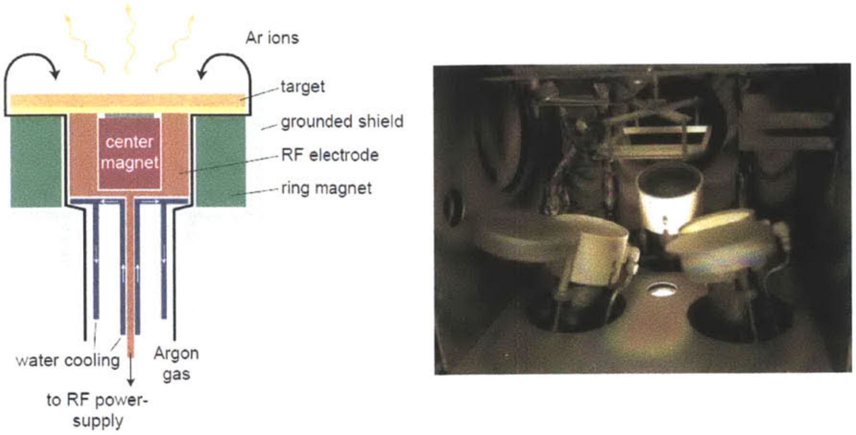

Figure 3-3: Diagram and a picture of the RF magnetron sputtering system used in ONE Lab [Courtesy of Tim Osedach].

voltage is alternated at $f = 13.65$ MHz, which can then neutralize the built-up charge periodically.

The rate of film deposition can be controlled by adjusting the chamber pressure or the power delivered to the electrodes. Similarly to the thermal evaporator, RF sputtering typically deposits films at ~ 1 Åand offers a nanometer precision for the deposited film thickness. However, the presence of plasma in the chamber can damage any organic films on the substrate and limits the choice of the substrate. For this reason, RF sputtering on top of a QD layer is typically avoided.

3.2 Device Testing

The QD-LEDs we fabricate are tested for their electrical and optical properties to assess their performances. Since QD-LEDs are still in their developmental stage, there is no standardized QD-LED and almost every QD-LED in literature is different. The following device evaluation allows us to ensure that the QD-LEDs we study are among the best QD-LEDs reported. In this section, we briefly describe the standard tests we perform on our QD-LEDs.

3.2.1 Current-Voltage and External Quantum Efficiency

Current-voltage (IV) measurement, in addition to verifying the diode-like rectifying behavior, provides valuable information about the turn-on voltage, conductivity, and different conduction mechanisms present in the device. A typical IV curve of a QD-LED is shown in Fig. 3-4. The IV curve follows power laws and generally exhibits at least two different regimes of conduction. The exponent reveals the type of the conduction mechanism present (see Appendix B.2 for details). At low biases, the conduction occurs via ohmic conduction ($V \propto J^1$), whereas at high biases, the conduction occurs via trap-limited conduction ($V \propto J^{m+1}$, where m > 1. See appendix B.2.). The turn-on voltage is typically close to the bandgap of the QD which ensures that there is efficient carrier injection into the QDs. The current density of the devices can reach up to $\sim$ 1 A/cm^2, which is in stark contrast to GaN LEDs which can operate at $\sim$ 100 A/cm^2.

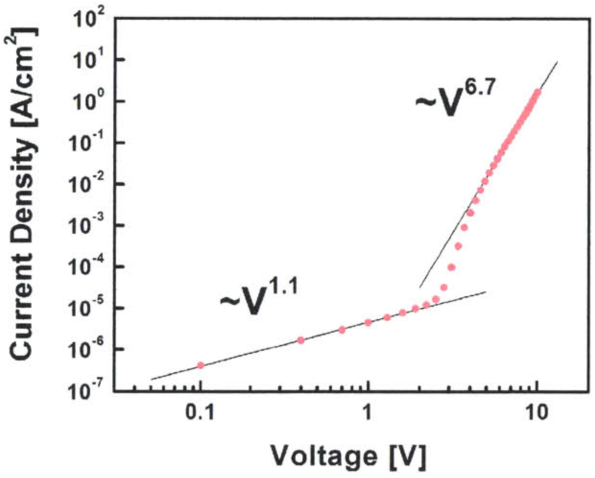

Figure 3-4: A typical current density vs. voltage relationship observed for a QD-LED. Plotting the curve in log-log scale presents two regimes where the curve follows a power law. Below the turn-on of the diode, the curve exhibits ohmic conduction (power of 1). After the turn-on, the curve exhibits trap-limited conduction (power greater than 2; 6.7 in this case).

EQE measures the ratio of the number of photons emitted out of the device to the number of electrons injected into the device, per unit time, at every voltage step. In practice, it is measured simultaneously with the IV measurement by simply placing a photodetector over the device and recording the photocurrent generated by the EL of the device. EQE is calculated by

$$EQE = \frac{g\lambda I_{pc}}{hcR}\frac{q}{I}, \tag{3.1}$$

where g is geometrical correction factor (solid angle covered by the photodetector divided by 2π), λ is the wavelength of the EL, I_{pc} is the photocurrent of the detector, h is the Planck's constant, c is the speed of light, R is the responsivity of the photodetector (in [A/W]), q is the elementary charge, and I is the current through the device.

3.2.2 Luminance

Luminance, measured in [Cd/m^2], is a measure of luminous flux perceived by the eye and is a figure of merit for how bright a surface appears. Generally, $10^2 \sim 10^3$ cd/m^2 is required for display applications and $10^3 \sim 10^4$ cd/m^2 is required for solid-state lighting applications. Average luminance from a device is given by,

$$L = \frac{683}{2\pi} \times EQE \times \frac{J}{q} \int EL(\lambda)\overline{y}(\lambda)\mathrm{d}\lambda, \tag{3.2}$$

where J is the current density through the device, q is the elementary charge, $EL(\lambda)$ is the EL spectrum normalized by area under the curve (power per unit wavelength), and $\overline{y}(\lambda)$ is standard luminosity function. The luminosity function, shown in Fig. 3-5, describes the average spectral sensitivity of human eye to brightness and is a unitless function. We stress that this is luminance averaged over the 2π steradian emission out of the device. Luminance is a function of the viewing angle of the device since the emission profile is not isotropic and is rather Lambertian. The peak intensity occurs in a direction normal to the surface and its intensity is twice that of the average calculated in Equation 3.2.

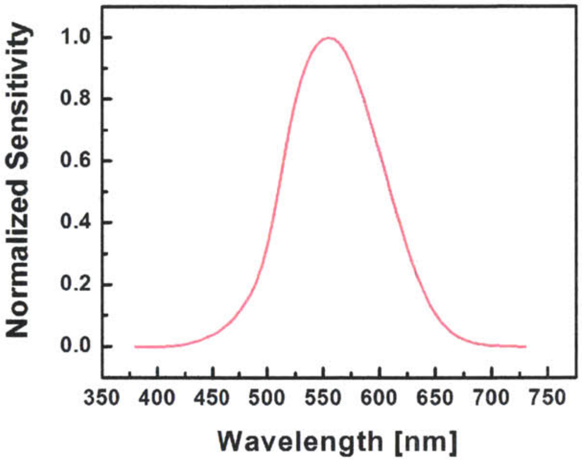

Figure 3-5: The luminosity function shows the sensitivity of an average human eye as a function of wavelength.

3.3 QD-LED used in this Thesis

Since the device performance and, quite possibly, the working mechanism are dependent on the device structure and its fabrication method, it is important to know every detail of the device under investigation. This section briefly discusses the particular QD-LED investigated in this thesis.

The device structure investigated is a type-IV QD-LED (section 2.4.1) with organic-inorganic hybrid charge transport layers that recently attracted attention due to its record high EQE and brightness. The device was fabricated on a glass substrate with indium-tin-oxide and has the structure: ITO (150 nm)/ZnO (50 nm)/QDs (30 nm)/4,4-bis(carbazole-9-yl)biphenyl (CBP) (100 nm)/MoO_3 (10 nm)/Al (100 nm). ZnO was radio-frequency sputtered, QDs were spin-cast out of chloroform, and CBP, MoO_3 and Al were thermally evaporated. We used CdSe-ZnCdS core-shell QDs with a peak PL wavelength of 610 nm, provided by QD Vision Inc. Current density and normalized EQE for a typical device are shown in Fig. 3-6. The EQE peaks at 2% at 4 V applied bias and the maximum luminance can reach up to 30,000 cd/m^2 which are both comparable to the most efficient QD-LEDs reported today. The energy level diagram of the device is shown in the inset, and is based on literature

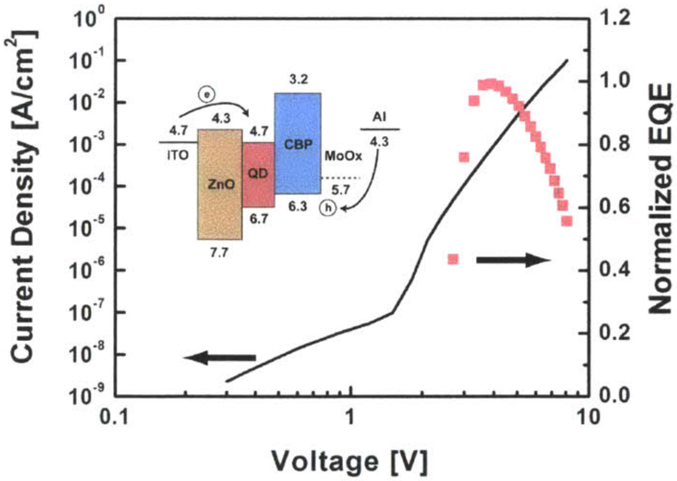

Figure 3-6: Current density and normalized EQE as a function of voltage for a typical QD-LED used in this thesis. The peak EQE is 2%. The inset shows the energy levels of the device based on literature values.

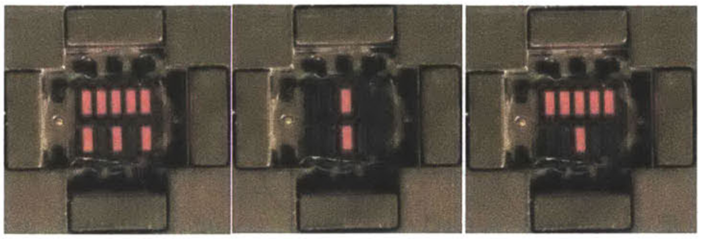

Figure 3-7: A picture of a QD-LED used in this thesis, emitting at 610 nm. Ten devices are patterned onto each of 0.5 in × 0.5 in glass substrates.

values [1, 9, 86, 138].

These QD-LEDs are fabricated onto 0.5 in × 0.5 in glass substrates with patterned ITO cathodes. The number of devices per substrate (ten) and the device area (0.0121 cm^2) are defined by the overlap between the bottom ITO cathode pattern and the top Al anode pattern. A photograph of the QD-LEDs in operation, emitting at 610 nm, is shown in Fig. 3-7. All the QD-LEDs studied in this thesis are a variation on the structure mentioned above unless otherwise noted. A more detailed description of this fabrication procedure is given in Appendix A.

Chapter 4

Efficiency roll-off in QD-LEDs

QD-LEDs, which capitalize on the excellent color saturation and high photoluminescence efficiency of colloidal QDs, offer the prospect of a new generation of display technologies. However, these devices suffer from decreasing EQE at high-current-density operations, on the order of $0.1 \sim 1$ A/cm^2. This behavior, known as the efficiency roll-off or efficiency droop, is a severe problem for QD-LEDs targeting solid-state lighting applications which require high brightnesses.

This is the first of three chapters in this thesis focused on understanding the origin of efficiency roll-off in QD-LEDs. Understanding the cause not only gives us a better insight into the workings of QD-LEDs but also is an important step towards being able to design brighter QD-LEDs. Consequently, these chapters can be instructional for designing QD-LEDs that are aimed to be used for high brightness applications like solid-state lighting. The first question to be answered is whether the roll-off is a behavior rooted in the use of the QDs or is due to extrinsic parameters such as the neighboring charge transport layers. We investigate the origins of the roll-off behavior in QD-LEDs by performing simultaneous measurements of QD EL and PL efficiencies of a QD-LED at different voltage biases, which pinpoint the cause of the roll-off to be a decrease in QD luminescence efficiency.

4.1 Efficiency roll-off

Efficiency roll-off is a problem that affects most types of LEDs including QD-LEDs, OLEDs, and GaN LEDs [12, 13, 139]. The proposed mechanism responsible for the roll-off has been different for each architecture. Fig. 4-1 shows some examples of the efficiency roll-off present in different types of LEDs. For efficient OLEDs, which generally use phosphor dopants as emitters, the cause has been attributed to triplet-triplet annihilation [139]. Combination of long exciton lifetime and high current density increases the probability of generated excitons to diffuse and interact with each other before their natural recombination lifetime. For GaN LEDs, the cause has been generally attributed to the Auger recombination [13]. In this scenario, the electron-hole pairs find and interact with free charges (electron or hole) before their natural recombination lifetime. For QD-LEDs, a mechanism to explain its efficiency roll-off had not yet been proposed. Compared to GaN LEDs, which generally shows the roll-off at $\sim$ 10 A/cm^2, QD-LEDs generally exhibit the roll-off at a much lower current density of $\sim$ 0.1 A/cm^2. Although OLEDs exhibit the roll-off at similar current densities, CdSe QDs generally have much shorter exciton lifetimes than the phosphors used for OLEDs ($\sim$ 10 ns for CdSe QDs compared to $\sim$ 1 μs for a phosphor like Ir(ppy)$_3$). This indicates that the cause for the efficiency roll-off in QD-LEDs may be different from those of other types of LEDs.

4.2 Cause of efficiency roll-off in QD-LEDs

Possible explanations for the efficiency roll-off in QD-LEDs fall under two broad categories. First, the roll-off may be a result of reduced QD luminescence efficiency at high voltage biases. There are many possible mechanisms that can cause QD luminescence quenching, which will be explained in the next chapter. Second, the roll-off may be a result of charge carrier leakage. In this case the electrons and/or holes are not well confined to the QD layer and leak through their respective blocking layers (organic layer for electrons and ZnO for holes).

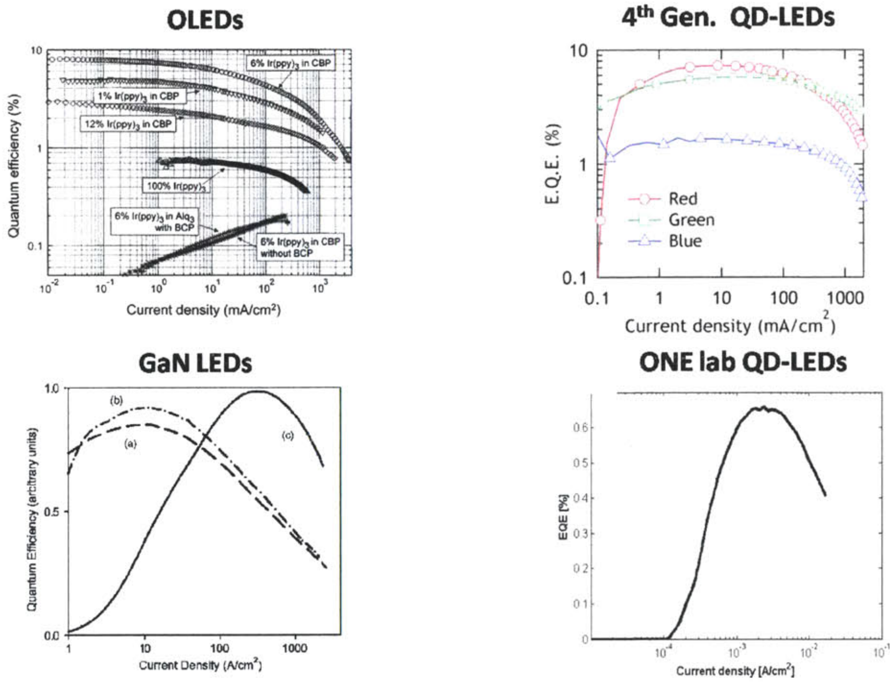

OLEDs

4th Gen. QD-LEDs

GaN LEDs

ONE lab QD-LEDs

Figure 4-1: EQE roll-offs for different kinds of LEDs including an OLED [11], a type-IV QD-LED [12], a GaN LED [13], and a QD-LED fabricated at ONE Lab. The roll-off is an universal behavior for LEDs but the cause is different for each type of LED.

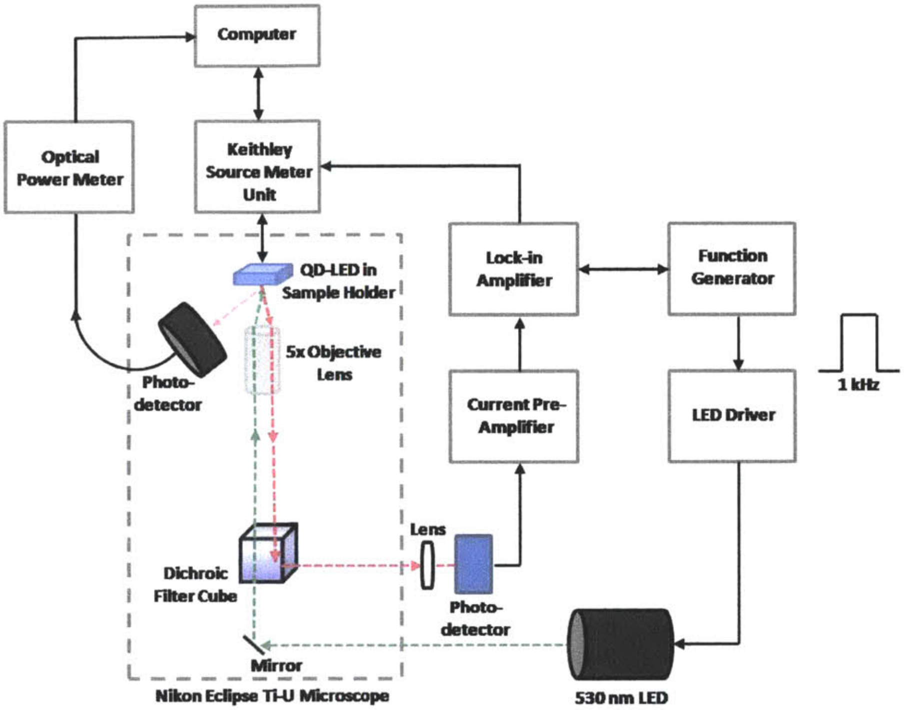

Figure 4-2: Simultaneous electroluminescence and photoluminescence measurement setup. The PL efficiency of the QDs in a QD-LED is measured as the device bias is swept by illuminating the device with $\lambda = 530$ nm LED light modulated at 1 kHz. The combined EL and PL is collected using a Si photodiode and sent to a lock-in amplifier, where the PL signal (AC) is separated from the EL signal (DC).

To identify which of these two mechanisms dominates, we perform a simultaneous EL-PL experiment to monitor the relative EL and PL efficiencies of the QDs in a QD-LED as the device bias is swept. The experimental setup is shown schematically in Fig. 4-2. To isolate the PL contribution from the total luminescence, we modulate the PL excitation source ($\lambda = 530$ nm LED) at 1 kHz and send the combined EL-PL signal (collected using a Si photodiode and a current-preamplifier) to a lock-in amplifier. The PL intensity is intentionally kept low (PL/EL $< 0.001\%$ at maximum brightness) to avoid significantly increasing the charge density within the QD layer. As shown in Fig. 4-3, an excitation wavelength of 530 nm ensures that the QD layer is excited without exciting the surrounding wider bandgap charge transport layers.

We first verify that the optical excitation of the QDs by the LED does not modify the exciton dynamics inside the LED by performing intensity dependent PL mea-

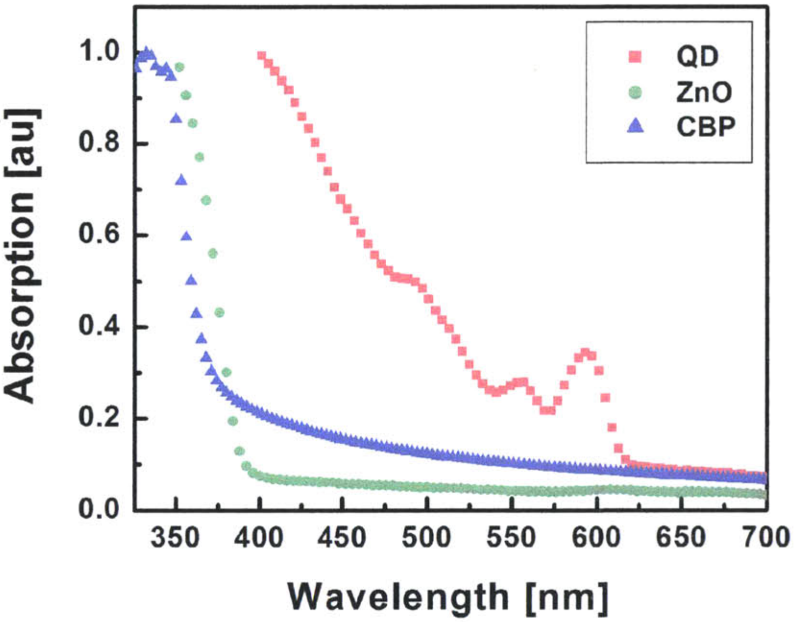

Figure 4-3: Absorption spectra of the main constituents of the QD-LED: QD, ZnO, and CBP. Excitation wavelength of $\lambda = 530$ nm ensures the selective excitation of the QDs in the device.

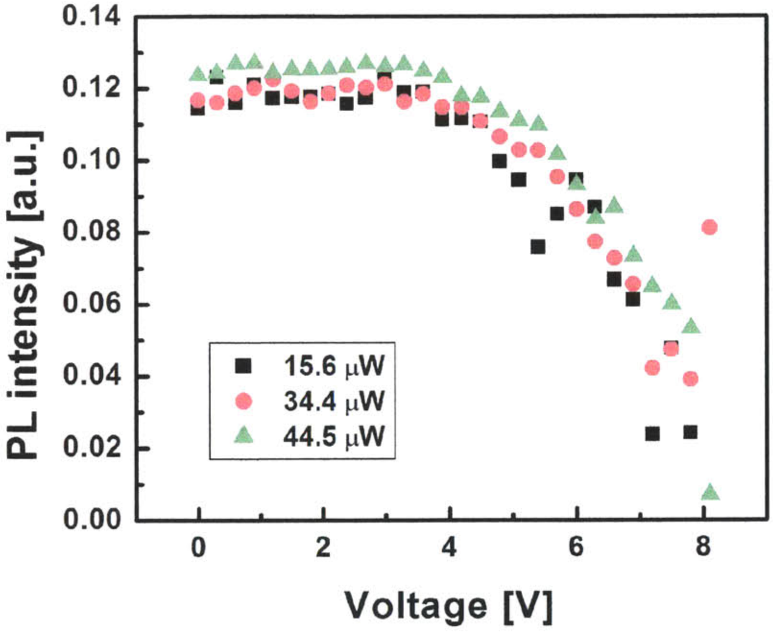

Figure 4-4: Relative PL efficiency of the QDs in the QD-LED as a function of bias voltage for three different excitation intensities: 15.6, 34.4, 44.5 μW. The PL efficiency is independent of the excitation intensity, indicating that the optically formed excitons are not affecting the measured PL efficiencies.

surements. The PL efficiency of the QDs, as a function of the voltage bias, for three different excitation light intensities is shown in Fig. 4-4. The excitation intensity is varied from 15.6 to 44.5 μW and each PL intensity is normalized by its excitation intensity. We find that all the curves show the same constant QD PL efficiency below 4 V (voltage independent) and a roll-off above 4 V. Therefore, we do not have to worry about the optically generated excitons perturbing the EL of the device.

The result of overlaying this QD PL efficiency with the QD-LED efficiency is shown in Fig. 4-5 with EQE and the QD PL intensity normalized at 4 V applied bias. We find that above 4 V the PL intensity decreases monotonically with increasing bias, tracking the decrease in EQE of the QD-LED. The correspondence between the decreasing PL and EL efficiencies with applied bias identifies the change in the QD luminescence efficiency to be sufficient to explain the QD-LED roll-off behavior. In the following chapters, we will further investigate the cause of this QD luminescence

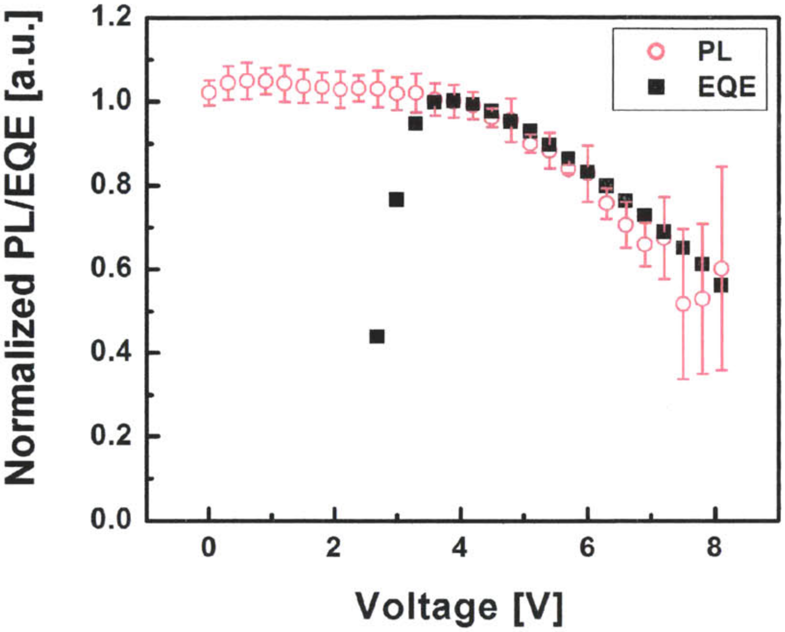

Figure 4-5: EQE and QD PL intensity of the QD-LED (normalized at 4 V, when the peak EQE = 2%) as a function of voltage. Roll-off of the EQE above 4 V reflects reduced QD PL efficiency at high biases.

quenching.

Chapter 5

QD Luminescence Quenching in QD-LEDs

From studies on single QDs to films of QDs, there are many known causes that can quench the PL of QDs. Some of these causes, including heating, charging, and applying an electric field, have possible relevance to the QDs in a QD-LED. Most of these studies often use QDs that reside in relatively controlled environments so that the effects can be analyzed individually. However, the QDs in a QD-LED sit in a complex structure that allows for many of these effects to occur simultaneously.

In the previous chapter, we identified the QD luminescence quenching to be responsible for the efficiency roll-off in our QD-LED. In this chapter, we identify the mechanism by which the QD luminescence gets quenched. Understanding which of the causes is dominant in a QD-LED would help in designing a device structure that mitigates the roll-off. Through comparison of EL and PL spectra we find that strong electric fields are responsible for the reduced QD luminescence. Electric-field-induced quenching is accompanied by red-shifting of the luminescence spectra, known as the quantum confined Stark effect (QCSE), which we use as a measure for the strength of the electric field dropped across the QDs in the device. Using voltage-dependent QCSE observed in the EL, we correctly predict the roll-off of up to 50%.

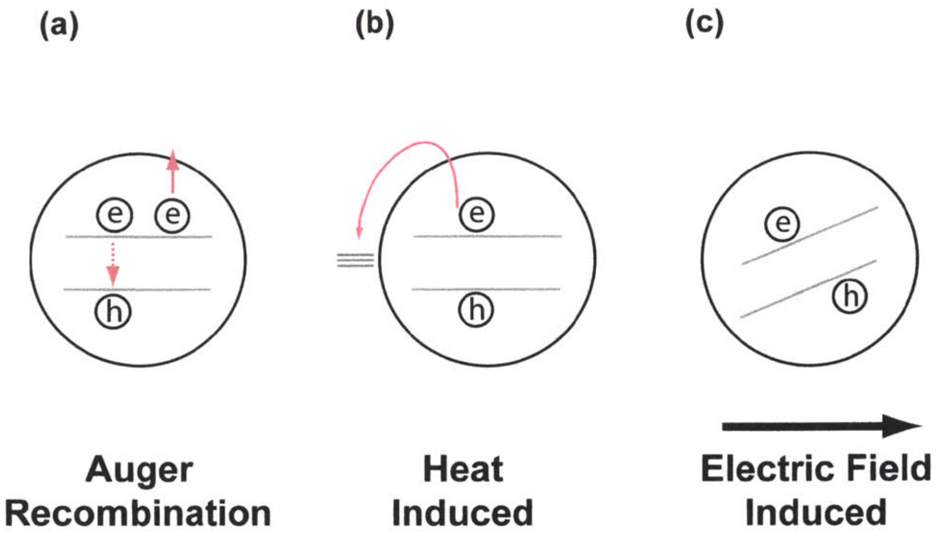

Figure 5-1: Three QD PL quenching mechanisms possible in a QD-LED. (a) The Auger recombination involves an exciton non-radiatively transferring its energy to a nearby free charge carrier. (b) Heat-induced quenching involves one or both of the charge carriers constituting an exciton escaping to a surface defect state via thermal excitation. (c) Electric-field-induced quenching involves dissociation of an exciton or reduced radiative recombination rate due to reduced overlap between the electron and hole wavefunctions.

5.1 QD Luminescence Quenching Mechanisms

Reduction of PL efficiency in QD thin films has been previously measured when QDs are charged (Auger recombination) [15], heated [140], or placed under a strong electric field [14, 141]. The three causes are depicted in Fig. 5-1. The Auger recombination is a three particle process involving a bound electron-hole pair (exciton) and an extra charge (Fig. 5-1 (a)). In this process, instead of emitting a photon, the exciton recombines to give its energy to the extra charge, which then quickly thermalizes back to its ground state. In QDs, the Auger recombination has been previously discussed for cases when the extra charge resides in the QD [142], when the extra charge resides in a deep trap state [143], and when the exciton is an electron in the conduction band and a hole in a trap state [144]. In particular, the Auger recombination involving an extra charge in the QD is known to be the cause of PL intermittency, known as "blinking" [16].

Heating is thought to excite the charge carriers out of the QD into surface defect states (Fig. 5-1 (b)) [140,145]. The quenching of QD PL due to heating can be seen in Fig. 5-2, which shows that as much as ~ 15%, 35%, and 70% of the PL is quenched at 50°C, 70°C, and 100°C, respectively. Therefore, keeping the junction temperature low is essential for efficient device operation. As a matter of fact, heating of the device is a known problem for GaN LEDs, where operating at current densities ~ 100 A/cm^2 can result in junction temperatures close to 70°C, leading not only to reduced efficiencies but also to reduced longevity of the device [146].

Lastly, electric-field-induced quenching of QD PL is a known quenching mechanism that is accompanied by a red-shifting of the PL spectrum, known as the QCSE. QCSE can be understood using the first two terms of the perturbation theory:

$$\Delta E_n = \langle n| \Delta H |n\rangle + \sum_{k \neq n} \frac{|\langle k| \Delta H |n\rangle|^2}{E_n - E_k} \tag{5.1}$$

where $\Delta H = ezE$ for a perturbation due to an electric field. This equation is sometimes rewritten as:

$$\Delta E_n = \mu \cdot E + \frac{1}{2}\alpha E^2 \tag{5.2}$$

where $\mu = e\langle n| z |n\rangle$ and $\alpha = 2e^2 \sum_{k \neq n} \frac{|\langle k|z|n\rangle|^2}{E_n - E_k}$ are the dipole moment and polarizability of state $|n\rangle$, respectively. For QDs, the first order term is observed only when a single QD is studied [99]. For an ensemble of QDs such as a QD film, random orientation of the dipoles generally cancels out the first order term. Hence, what is observed is an energy shift that has a quadratic dependence on the electric field strength.

The actual quenching mechanism of the PL due to the electric field is still not well understood, and likely depends on many factors such as the material composition of the QD, thickness of the shell, and quality of the surface passivation. For example, the material composition and the shell thickness can determine how well the electron and hole wavefunctions are confined to the center of the QD when the electric field is applied [147]. If the wavefunctions are not well confined, the electric field can pull the

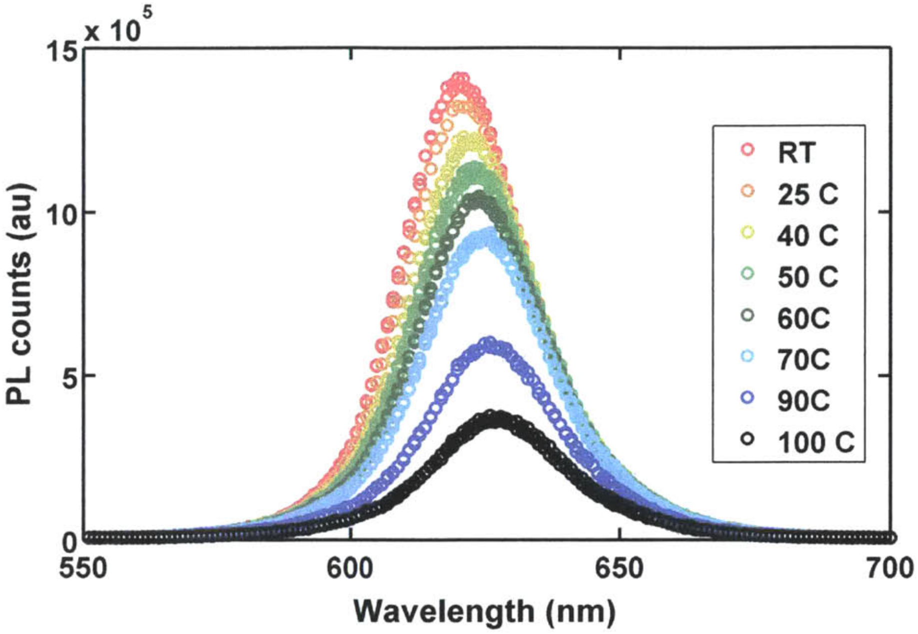

Figure 5-2: PL spectra of a QD thin film as a function of temperature.

electron and hole apart (Fig. 5-1 (b)), decreasing the radiative exciton recombination rate. QDs with thin or no shell are also prone to exciton dissociation [148], which can increase the non-radiative exciton recombination rate. Lastly, a recent report by Galland *et al.* suggests that hot electrons can be trapped by surface defect states [16], which can reduce the efficiency of bandedge exciton formation altogether. This trapping is also likely a function of the electric field as proposed by Park *et al.* [14]. Therefore, there are many possible mechanisms that can contribute to electric-field-induced quenching of QD PL.

In order to determine which of the mechanisms mentioned above is causing the efficiency roll-off, we first determine the mechanisms which are not likely to be dominant in our QD-LED. We eliminate temperature effects on the QD PL efficiency, as measurement of the operating temperature of our QD-LEDs with an infrared camera shows a change of no more than few degrees during the duration of the measurements, which is not sufficient to affect the PL efficiency and explain the roll-off. This does not mean that the QD-LEDs do not heat up, but rather that the few seconds the device is on for a measurement is not long enough to heat the device. In comparison, OLEDs, which are structurally very similar and operate at comparable current densities, can reach a junction temperature of 60°C at a current density of 1 mA/cm^2 [149]. However, the temperature of OLEDs does not rise immediately after turning on the device but rather rises slowly depending on the thickness of the glass substrate [150]. For a common glass substrate with a thickness of ~1 mm, the temperature rise has a time constant on the order of tens of seconds, which is much longer than the time it takes to make our measurement. Therefore, we assume that the temperature effect is negligible in our measurements.

We similarly rule out the charging effects since QDs generally have a long charge retention time (on the order of minutes to hours [15]) whereas the efficiency roll-off curve [Fig. 3-6] is measured within seconds and was repeated many times with the peak EQE unchanged. If charging were causing the roll-off, we would not expect the peak EQE to recover to the same value in consecutive measurements. From these observations, we hypothesize that the electric field associated with the applied bias is quenching the QD luminescence at high voltages.

5.2 Electric-Field-Induced Quenching of QD Luminescence

Earlier studies of the electric-field effect on QDs, also known as the QCSE, showed that the luminescence intensities and spectral shifts of QDs are field dependent [99]. To characterize the QCSE in the QDs inside our QD-LED structure, we first measured the PL spectra of the QD films in our device under reverse bias using the measurement setup shown in Fig. 5-3. Reverse biasing allows the effect of electric field on the QDs in the QD-LED to be studied in situ, in the absence of any charge injection. To avoid damaging the device from prolonged reverse biasing, we apply sawtooth-like voltage waveforms (Fig. 5-4) with a 500 Hz repetition rate. The sawtooth amplitude peaks at -18 V and is followed by a duration of positive voltage (1.6 V) to reduce stress on the device by minimizing the average net applied voltage, but without turning on the EL.

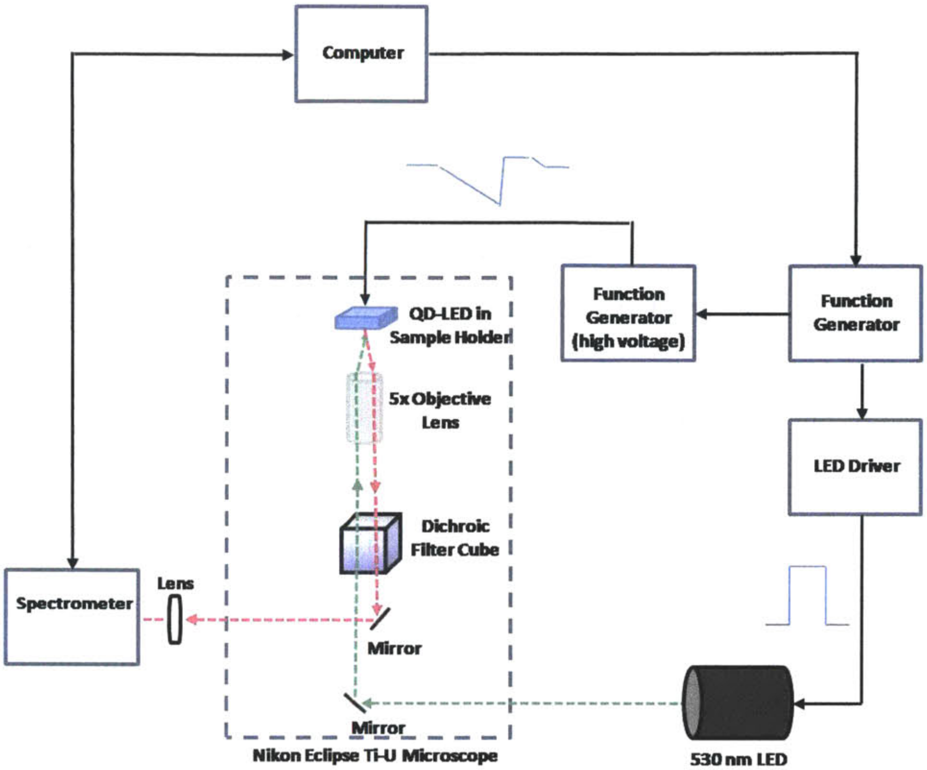

Figure 5-3: PL measurement setup to measure the QD PL spectra of QD-LEDs as they are reversed biased using the sawtooth-like voltage waveform shown in Fig. 5-4

QD PL is induced by a $\lambda = 530$ nm LED emitting 100 μs wide pulses synchronized with the voltage waveform and QD PL spectra are collected with a spectrometer. By sweeping the time delay (phase shift) between the voltage waveform and the illumination pulse, PL spectra of the QDs under different electric-field strengths can be collected while keeping all other conditions unchanged. To assess the degree to which the QCSE occurs while the QD-LED is in operation, EL spectra are monitored as the device is forward biased using the measurement setup shown in Fig. 5-5, again with all other experimental variables held constant. This combined approach allows the study of QD PL and EL from the same active device structure.

The resulting QD PL and EL spectra are normalized and their peak emission energies are compared. Fig. 5-6 shows EL spectra obtained at 5, 11.6, and 13.8 V overlaid with PL spectra with coincident peak energies (PL at 1.6, -8.6, and -16 V, respectively). Both PL and EL spectra are approximately Gaussians at low

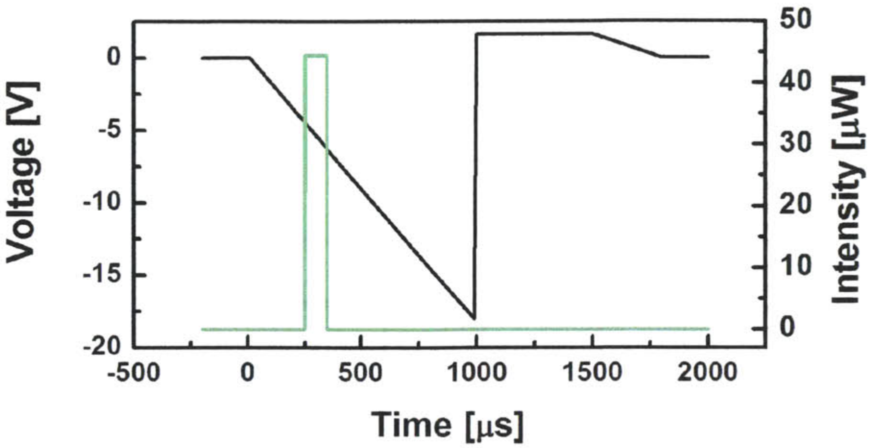

Figure 5-4: Electric-field-dependent QD PL was measured by applying a sawtooth-like voltage waveform to the QD-LED and illuminating it with a 530 nm LED pulse synchronized with the voltage waveform. QD PL at varying electric fields was measured by sweeping the delay (phase) between the voltage waveform (black line) and the LED pulse (green line).

biases and redshift at higher biases. However, EL does not exhibit the same spectral broadening that is observed in the PL. In particular, a shoulder begins to appear on the low energy side of the PL spectra. The inset of each panel in Fig. 5-6 shows a double-Gaussian fit to each asymmetrically broadened PL spectrum. We attribute the double-Gaussian profile to emission from QD subpopulations that are placed in two different environments; for example, a layer of QDs next to ZnO and a layer of QDs away from ZnO. QDs placed adjacent to the ZnO are expected to exhibit energy levels that differ from that of QDs placed adjacent to the CBP, which has a lower dielectric constant [151]. The difference between the EL and PL spectra (even when the peaks are matched) can be explained by the fact that the electric field distribution is generally different between forward and reverse biased diodes [152], thus affecting the two populations differently.

Each PL and EL spectrum is decomposed into two Gaussians, and their intensities and peak energies as a function of device voltage are shown in Figs. 5-7(a) and (b), respectively. The black solid line in Fig. 5-7(a) is a fit to the PL intensity data

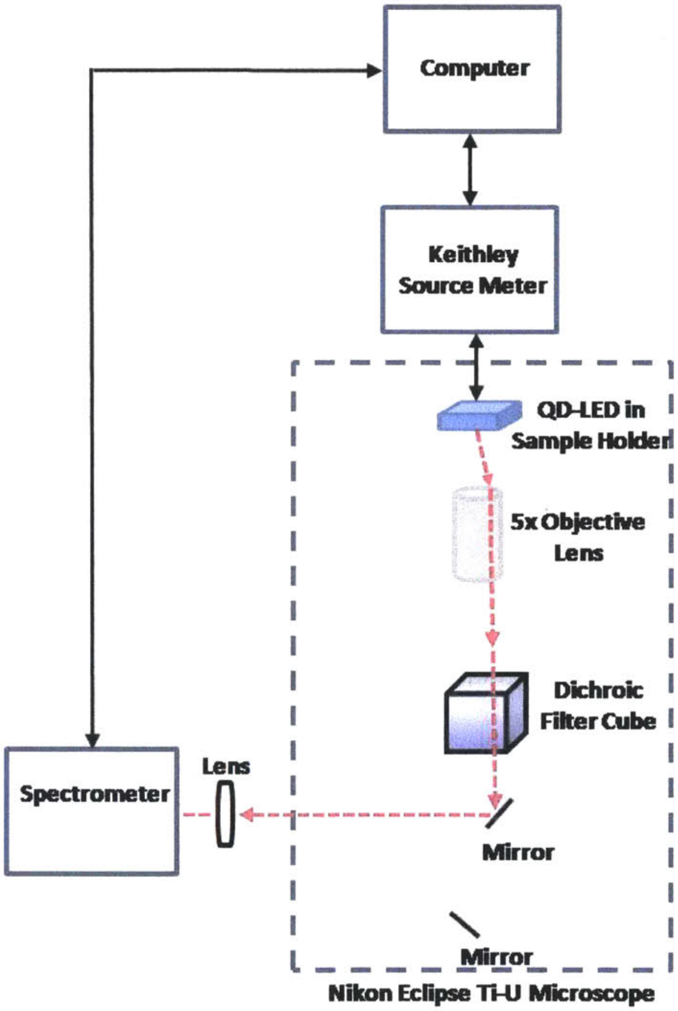

Figure 5-5: EL measurement setup to measure the QD EL spectra of QD-LEDs as they are forward biased. The integration time of the spectrometer is adjusted as the LED gets brighter to avoid saturation.

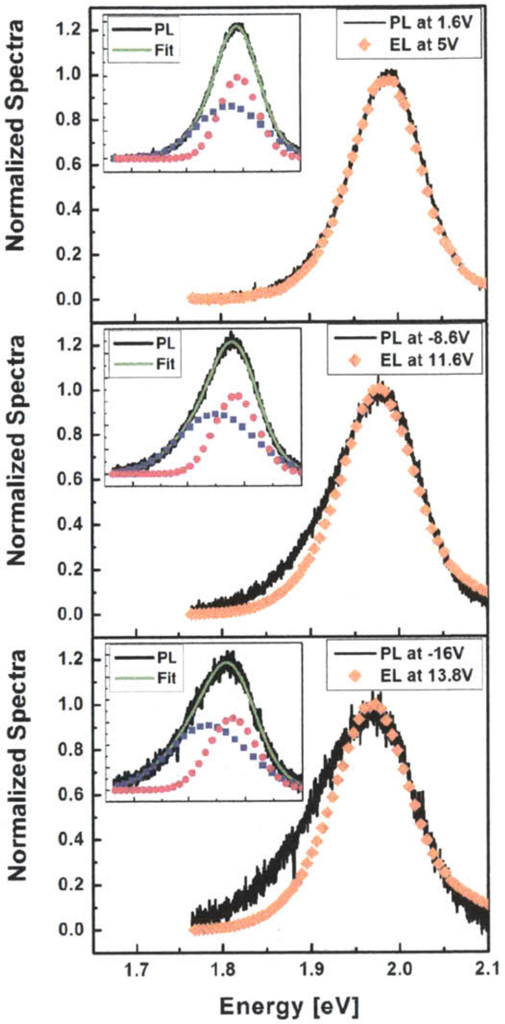

Figure 5-6: Comparison of QD PL spectra (black lines) and QD EL spectra (orange diamonds) at corresponding peak emission energies, for three different biases. At high biases, the PL spectrum exhibits a red shoulder that is not observed at lower biases or in the EL spectrum. Insets: PL spectra (black) are reconstructed (green) using two Gaussians, which correspond to emission from two QD subpopulations A and B (red and blue, respectively).

assuming a simplified version of the model described in Ref. [14] (section B.4). In Fig. 5-7(b), PL and EL peak energies for both subpopulations red-shift under high bias. In particular, the PL peaks of subpopulation A show a quadratic dependence on voltage (black fit), which is a signature of the QCSE. There is no clear fit for the EL peak shift because the distribution of the electric field inside the diode is voltage dependent. The peak energies are at their maximums when the device is slightly forward biased, indicating the presence of a built-in electric field, which is expected in a diode structure.

Assuming that the EQE of the QD-LED is predominantly governed by the QCSE at high forward biases, we should be able to predict the EQE by comparing the forward-bias EL to the reverse-bias PL from Figs. 5-7(a) and (b). A QD film exposed to the electric field will undergo a QCSE, which is manifested as a shift in the QD PL or EL emission spectra and a concomitant decrease in its PL or EL efficiency. Because the emission spectrum is a function of the applied field, whenever the forward bias QD EL emission spectrum of subpopulation A (subpopulation B) matches the reverse-bias QD PL spectrum of the same subpopulation, the QDs in subpopulation A (subpopulation B) are experiencing the same local electric field at those particular EL and PL biasing conditions. Therefore, for each subpopulation, the EL efficiency at each forward bias can be predicted by finding the corresponding PL spectrum in reverse bias with peak energy matching that of the EL peak, and assigning the PL efficiency at that electric field to the EL efficiency. We emphasize that the choice of physical model used to fit the data in Fig. 5-7(a) does not affect the predicted EQE, which is calculated directly from the PL and EL spectra and corresponding PL intensity.

For example, subpopulation A [Fig. 5-7(b), red] shows an EL peak shift from 1.990 to 1.984 eV between 5 and 10 V. This shift corresponds to the PL peak shift from -4.5 to -11.3 V and indicates that the luminous efficiency is reduced by about 37% [Fig. 5-7(a)] for subpopulation A as a result of the QCSE. The relative number of excitons formed on the two subpopulations (A and B) of QDs is calculated by dividing their EL intensities in Fig. 5-7(a) by their respective PL efficiencies. The

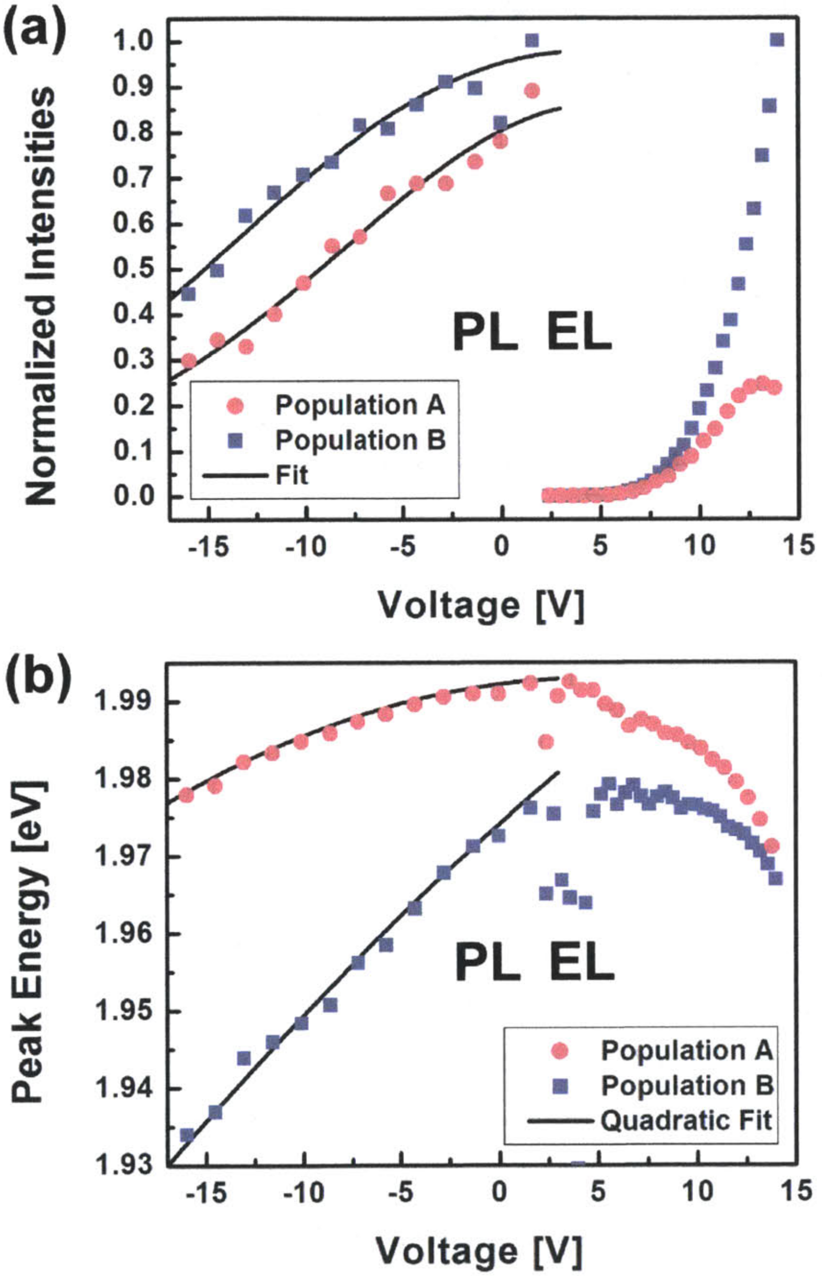

Figure 5-7: (a) Relative intensities of subpopulations A (red) and B (blue). The PL data are fitted to a simplified version of the model presented in Ref. [14]. (b) Peak energies of subpopulation A (red) and subpopulation B (blue). Quadratic fits (black lines) to the PL data are made assuming that the shifts are due to the quantum confined Stark effect.

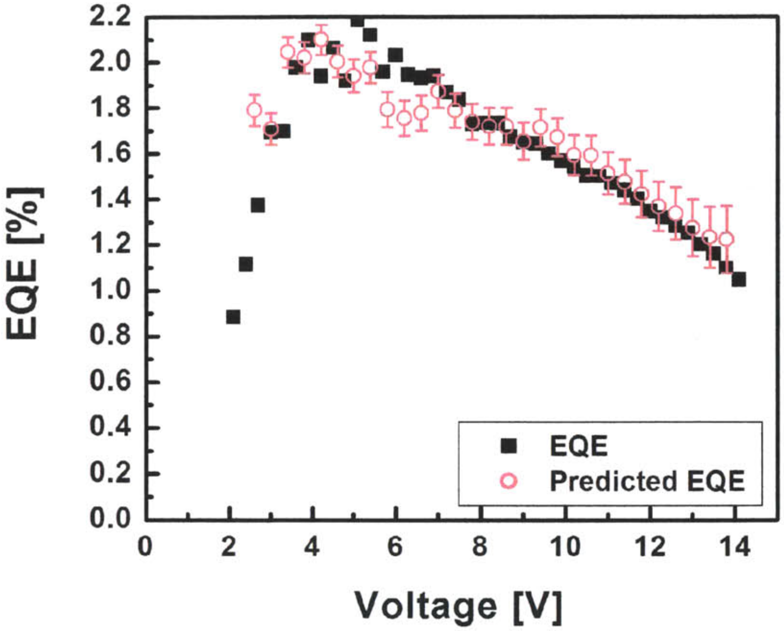

Figure 5-8: Measured EQE and predicted EQE as a function of voltage. EQE is predicted through the comparison of PL and EL data [Figs. 5-7(a) and (b)] as described in the text. The agreement between the data and the prediction shows that the quantum confined Stark effect can self-consistently account for the QD-LED efficiency roll-off.

overall EQE is then the weighted average of the EQEs of the two subpopulations. This analysis is applied for EL data between 2.5 and 14 V and the resulting predicted EQE, which is scaled to match the maximum of the measured EQE, is shown in Fig. 5-8. The predicted and measured EQEs are in good agreement, with the EQE rolling off by up to 40 % at 13 V. The match between the EQE behavior predicted by the QCSE and the experimentally observed efficiency roll-off is evidence that the electric field strength alone, and not carrier leakage or QD charging (Auger recombination), is sufficient to model the efficiency roll-off.

To further understand the effect of the electric field on the QD PL efficiency, we measured transient PL of the QDs in the QD-LED. The same reverse biasing scheme as Fig. 5-4 was used with 100 ps laser pulse train at $\lambda = 540$ nm replacing the green excitation LED. PL was detected with a Si avalanche photodiode and timing information was obtained via a time-correlated single photon counting module. The resulting transient PL at four different voltages reveal a lifetime of 4 ns for all of the voltages applied while the initial intensity decreases with higher applied voltage (Fig. 5-9). The inset indicates the times at which the QD PL intensity, I, has decreased from its initial value of I_0 so that $I/I_0 = e^{-1}$ and $I/I_0 = e^{-2}$ (τ_e^{-1} and τ_e^{-2} respectively). Reduction of QD PL efficiency due to the electric field has previously been attributed to a decrease in radiative exciton recombination rate (e.g., reduced electron-hole wave function overlap [153, 154], Fig. 5-10(a)), an increase in nonradiative exciton recombination rate (e.g., exciton dissociation [148, 155], Fig. 5-10(b)), or a decrease in the probability of forming thermalized excitons (e.g., hot charge carrier trapping by QD surface traps [16, 156], Fig. 5-10(c)). Because our QD film is 8% PL efficient, PL lifetime is dominated by the nonradiative rate. Therefore, the voltage independent PL lifetime observed suggests that the cause is either the decrease in the radiative rate or a decrease in the thermalized-exciton formation efficiency.

In conclusion, we have identified the electric-field-induced PL quenching of QDs to be responsible for the efficiency roll-off in QD-LEDs. We use the relationship between PL peak shifts and PL quenching of QDs subject to the QCSE, observed while reverse biasing a QD-LED, to predict the efficiency roll-off in forward bias. The roll-off predicted by this analysis is in excellent agreement with our experimental data and correctly traces an EQE reduction of nearly 50%. Transient PL measurements tentatively suggest that the reduced QD luminescence efficiency is not the result of an increased nonradiative recombination rate.

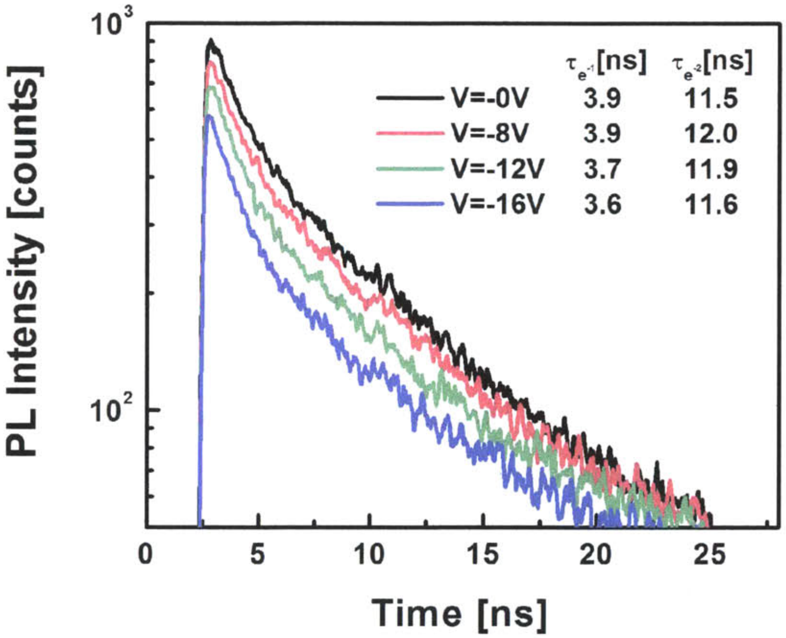

Figure 5-9: Transient PL of QDs in the QD-LED reverse biased at 0, -8, -12, and -16 V. Time constants of the decays (inset) are independent of the applied voltage, suggesting that the nonradiative exciton recombination rate is independent of the electric field.

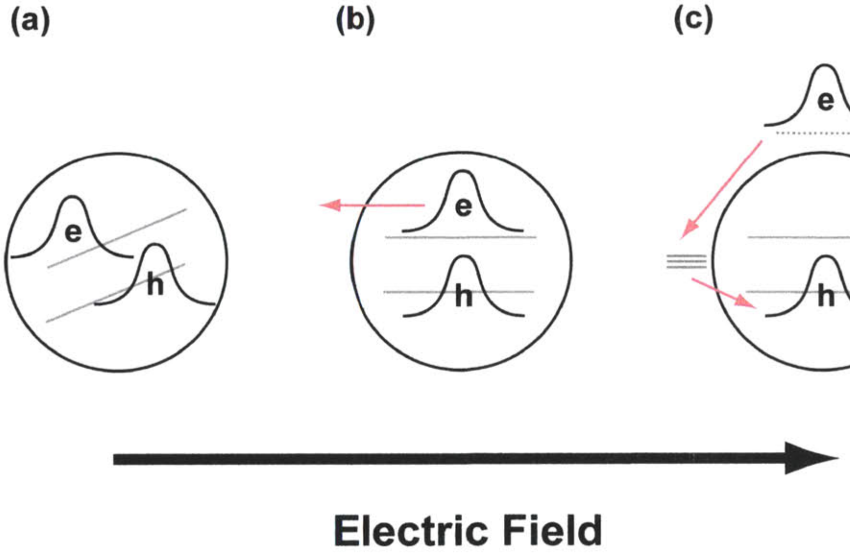

Figure 5-10: Three possible mechanisms for the electric-field-induced quenching of QD PL: (a) Reduced electron-hole wavefunction overlap leads to a decrease in radiative exciton recombination rate. (b) Exciton dissociation leads to an increase in nonradiative exciton recombination rate. (c) Hot charge carrier trapping by QD surface traps leads to a decrease in the probability of forming bandedge excitons.

Chapter 6

Electroabsorption Spectroscopy Study on QD-LEDs

In the field of single QD spectroscopy, it is well known that charging a QD results in Auger recombination that can quench its PL. Therefore, it is almost natural to assume that low or reduced luminescence efficiency of QDs in a QD-LED, where the device is designed to inject charges into the QDs, is due to the Auger recombination [93, 97, 110]. The non-Auger mechanism proposed to explain the efficiency roll-off is then a surprising theory that can benefit from additional confirmation. The question is whether QDs are really not charging as the applied voltage is increased.

In the previous chapter, through the comparison of QD EL and PL spectra, we identified the electric-field-induced quenching of the QD luminescence efficiency as the likely cause of the efficiency roll-off. However, the amount of QD charging is not quantifiable through the luminescence studies and the notion that QD charging does not significantly contribute to the efficiency roll-off remains an assumption based on circumstantial evidences. In this chapter, we assess QD charging and QCSE in a QD-LED through an examination of changes in the absorption features of the device using electroabsorption (EA) spectroscopy measurements. We show that less than 10% of the QDs are charged when the external quantum efficiency has rolled off by 60%, which makes Auger recombination an unlikely cause of the efficiency roll-off as previously assumed.

6.1 Features of Charged QDs

There are a few different ways to probe the charging state of the QDs. One way is to measure the transient PL lifetime of the QDs. Charged QDs exhibit Auger recombination; a non-radiative recombination mechanism which typically has a lifetime on the order of $0.1 \sim 1$ ns [16,157] depending on the size of the QD. Therefore, the presence of the Auger recombination can be quantified by probing the change in the PL decay lifetime. Another method is to measure the change in absorption spectrum of the QDs [15,158]. For example, Woo *et al.* has shown in a solid-state structure that charging a CdSe QD film can quench the absorption features involving the $1S_e$ state (i.e. $1S_{3/2}$-$1S_e$, $1S_{1/2}$-$1S_e$, etc.). As mentioned in section 2.2.3, the bandedge exciton ($1S_{3/2}$-$1S_e$) is eight-fold degenerate, which is a product of the two-fold degeneracy of the electron and the four-fold degeneracy of the $1S_{3/2}$ hole. Therefore, adding an extra electron in the conduction band prohibits the formation of half of these states and, hence, 50% of the absorption strength of this state is lost (Fig. 6-1(a)). As a result, the absorption features of the first and second excitonic states are partially bleached upon charging (Fig. 6-1(b)). Additionally, QDs retain the charges for a long time and these absorption bleaching features persist for minutes to hours (Fig. 6-1(c)).

Measuring the transient PL lifetime and measuring the change in the absorption spectrum of the QDs both have their pros and cons. If the QDs are the luminescent material with the lowest bandgap in the device structure, then the PL of the QDs can be obtained without exciting the other materials in the device. Therefore, the method is useful for probing just the QDs in the device without concerns for PL signals from the surrounding materials. On the other hand, this means the technique can not probe the behavior of the other materials in the device, which may also be charging. Furthermore, the Auger recombination is not the only mechanism that can alter the QD PL lifetime. Therefore, attributing the change in the lifetime to the Auger recombination is not a conclusive way of identifying QD charging. Experimentally, collecting the transient PL signal generally requires a long integration time. The signal is weak due to the weak absorption of a thin QD film in the device, low PL quantum yield of the QD film, and photon collection loss as the PL radiates over a wide solid angle. Long integration time can be a problem if the state of charging changes during that integration period.

Measuring the change in absorption spectrum of a material under electric field, such as the QDs in a QD-LED, is known as electroabsorption spectroscopy. This technique has the advantage of being able to probe changes in the absorption spectra of all the materials in the device structure simultaneously. Observing the bleaching of the QD excitonic features would also serve as a conclusive evidence for charged QDs. However, with many kinds of materials composing a device, it can be difficult to identify the material(s) responsible for the measured spectrum. Since the difference spectrum among different materials can overlap, if many kinds of materials are involved in generating the signal, then deciphering the observed difference spectrum becomes difficult.

6.2 Electroabsorption Spectroscopy on a QD-LED

The device structure investigated was a QD-LED with organic-inorganic hybrid charge transport layers, similar to the one used in the previous chapter. The main difference is that the ZnO film was, instead of sputtering, formed by spin-casting zinc acetate dissolved in methoxyethanol and baked on a hot plate. Current density and normalized EQE for a typical device are shown in Fig. 6-2(Top). The EQE peaks at 2% for 6 V applied bias and rolls-off by 60% by 13 V.

To assess the degree of QD charging and the QCSE present in the device, we perform EA measurements on the biased QD-LED, as shown in Fig. 6-3. We use a tungsten-halogen lamp to generate white light, and an iris and a lens to collimate the light into a beam. The beam is subsequently split into two beams using a beam-splitter, where one beam is used to measure the absorption change in the QD-LED by reflecting the beam off of the QD-LED from the ITO side and the other beam is used as a reference to monitor any spectral and intensity fluctuations of the lamp. The

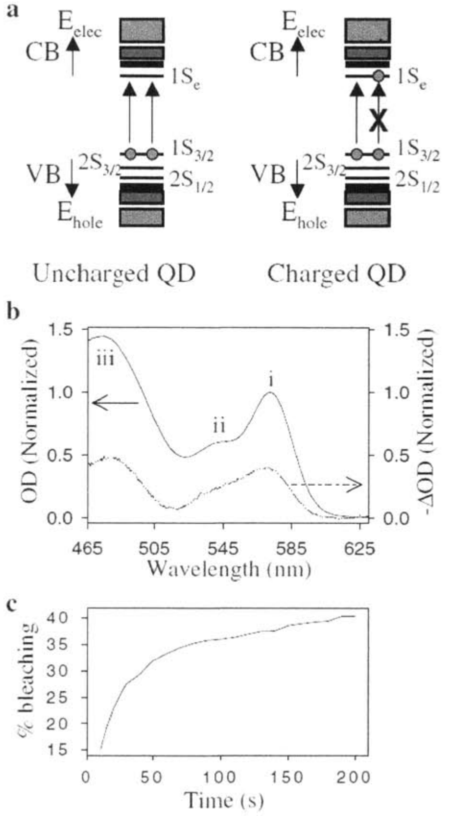

Figure 6-1: Absorption bleaching in charged CdSe QDs.(a) An extra electron in the conduction band decreases the $1S_{3/2}$-$1S_e$ transition probability by 50%. (b) Absorption spectrum for a solution of the QDs (solid line) and a change in the absorption spectrum of charged QDs. (c) Time-dependent change in the percentage bleaching of the band-edge-exciton state [15].

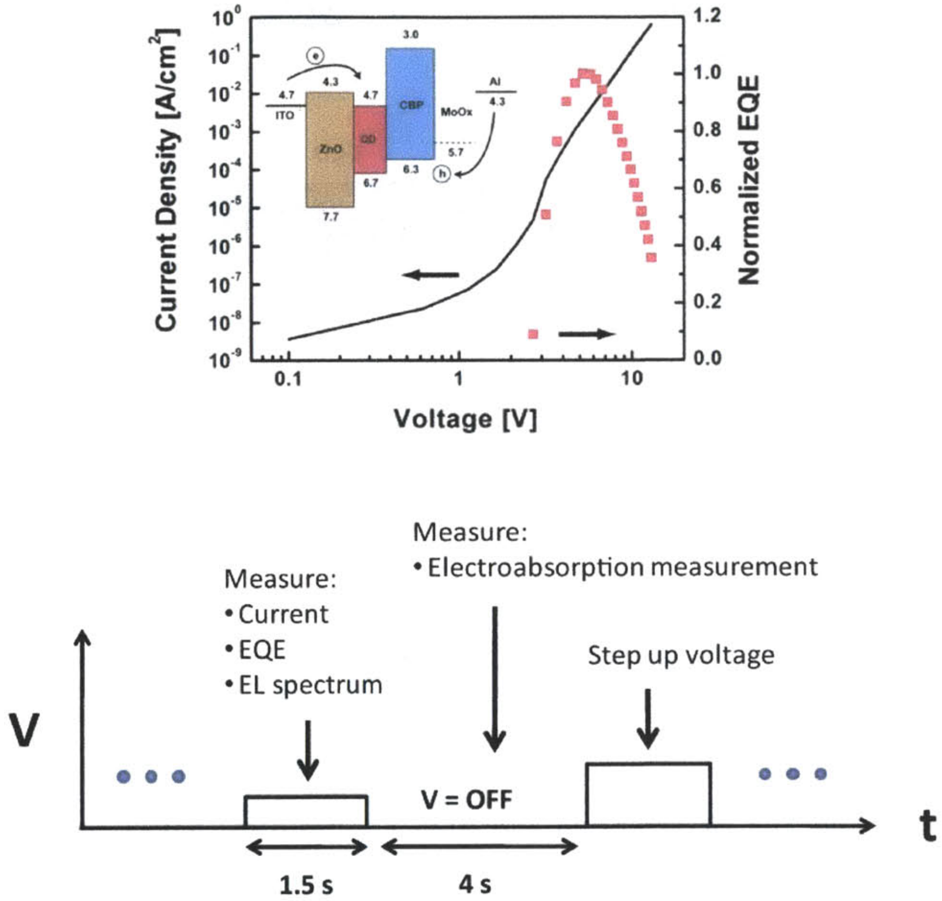

Figure 6-2: Top: Current density-voltage and external quantum efficiency (EQE)-voltage characteristics of the QD-LED under investigation. Inset: Energy band-diagram of the device, with indicated energy values referenced to the vacuum level. Bottom: Timing diagram for the electroabsorption spectroscopy measurement. The voltage is applied for 1.5s, during which current, EQE, and EL spectrum measurement are taken. The voltage is then turned off for 4s, during which the electroabsorption measurement is taken. The voltage is then stepped up and the process is repeated.

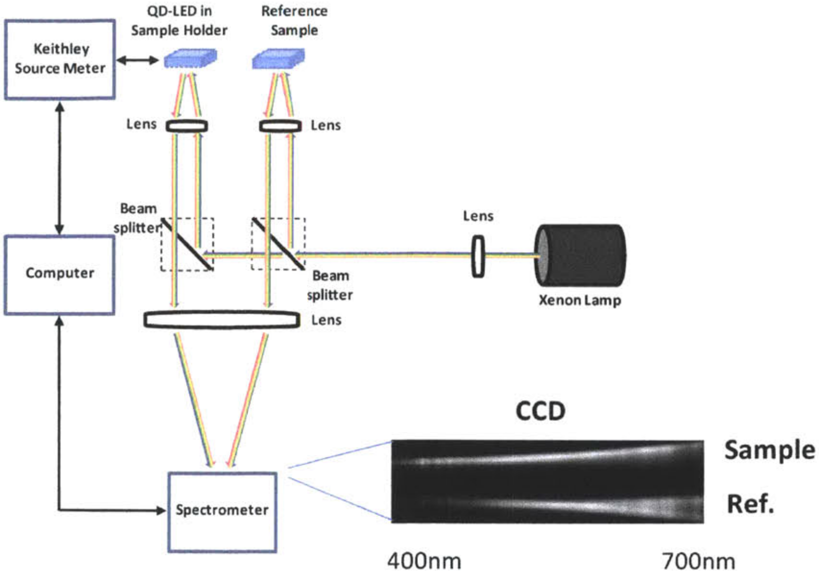

Figure 6-3: Measurement setup for the electroabsorption spectroscopy. A white light source (Xenon lamp) is split into two beams, with one reflected off of a QD-LED and the other reflected off of a reference sample, and focused into the spectrometer. The two spectra are taken simultaneously to later account for any spectral fluctuation of the lamp.

spectra of the two beams are simultaneously measured using a spectrometer, which averages 120 consecutively taken spectra to attain a reasonable signal-to-noise ratio. The QD-LED voltage bias is swept from 0 to 13 V with about 0.5 V increments. At each voltage step, the EL spectrum and EQE are measured before the QD-LED is briefly turned off (~4 seconds) to take EA measurements since the EL overwhelms any EA features (Fig. 6-2(Bottom)). We argue that this brief off-period does not affect the charging of the QDs significantly. Similar solid state QD charging structures have exhibited a charge retention time on the order of minutes [15] after the voltage was turned off, which is significantly longer than the off-period used here.

Spectra at 0 V is subtracted from all the spectra and the resulting EA spectra are shown in Fig. 6-4(a). To help identify the origin of four distinct EA spectral features appearing above applied voltages of 6 V, labeled $\alpha1$, $\beta1$, $\alpha2$, and $\beta2$, we measured separately the transient absorption (TA) spectra of the main constituents of the device: ZnO (50 nm), QD (60 nm), and CBP (100 nm) (Fig. 6-4(b)). The transient absorption measurements were performed using a pair of femtosecond laser pulses coincident on the sample in the familiar pump-probe geometry [159]. The pump pulse, which is generated from a tunable non-collinear optical parametric amplifier pumped by an amplified Ti:sapphire laser, resonantly excites a population of excitons in the sample. The so-called probe pulse is generated via continuum generation in sapphire or calcium fluoride using a copy of the amplified Ti:sapphire laser pulse that generated the pump pulse (Fig. 6-5). The spectral absorption of the probe pulse by the optically-excited sample is measured by a spectrometer and the arrival of the probe pulse at the excitation region is delayed from the pump pulse via an actuated delay line. ZnO and CBP TA spectra were obtained with pump pulses tuned to 3.5 eV and averaging the TA signal between 2 and 4.5 ps. This averaging was done to improve the SNR of the TA spectra and is possible because we observed the TA spectra to change very little during this time period. The QD TA spectrum was obtained with pump pulses tuned to 2.1 eV and averaging the TA signal over 20 and 45 ps. Neither the TA spectra of ZnO nor that of CBP, shown in Fig. 6-4(b), exhibits features observed in the EA spectra. The TA spectral features exhibited by the QD TA spectrum (shown in Fig. 6-4(b)) are labeled B1, B2, A2, and B3, in accordance with Ref. [160]. B1 and B2 are in position with 1S(e)-1S$_{3/2}$(h) and 1S(e)-2S$_{3/2}$(h) excitons, respectively (Fig. 6-4(c)), as expected from state-filling induced bleaching. Since the pump energy is lower than the 1P(e)-1P$_{3/2}$(h) energy and the QD TA spectrum were taken more than 1 ps after the excitation, it is unlikely that B3 is due to the bleaching of 1P(e)-1P$_{3/2}$(h) state. It may possibly be due to the red-shifting of the 1P(e)-1P$_{3/2}$(h) state, which is also believed to be the cause of A2 [160]. We also do not observe A1 which generally decays within the first few picoseconds upon excitation [160, 161]. Spectral similarity between α2 and A2 suggests that α2 may also be a feature due to the 1P(e)-1P$_{3/2}$(h) state red-shifted by the applied voltage. We do not observe any significant B1 or B2 bleaching features in the EA spectra, indicating, as we have previously predicted, the absence of any significant charging. Instead we observe zero-crossing between α1 and β1 coinciding with B1.

Earlier studies of the QCSE showed red-shifting of the lowest excited state [99] and, in the case of an ensemble of QDs, a change in the absorption spectrum that can be

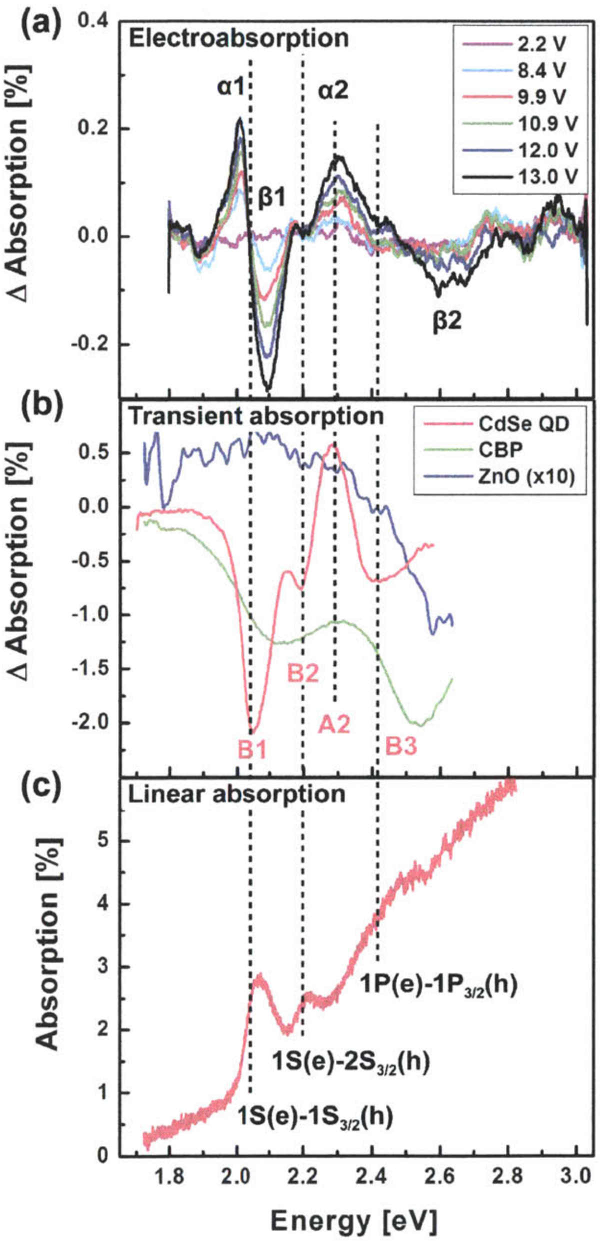

Figure 6-4: (a) Electroabsorption spectra of the QD-LED exhibiting four distinct features above 8 V bias. (b) Transient absorption spectra of the main constituents of the QD-LED. (c) Linear absorption spectrum of the QD.

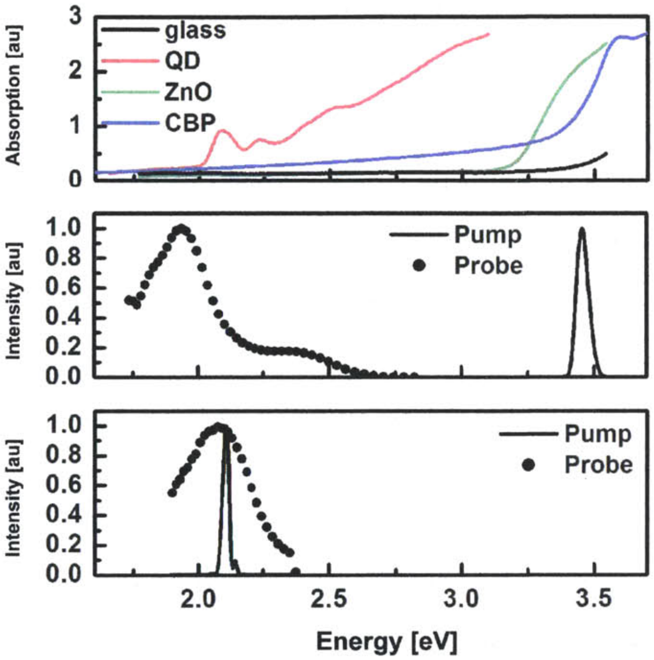

Figure 6-5: Top: Absorption spectra of the main constituents of our QD-LED: QD, ZnO, and CBP. Middle: Spectra of pump and probe used for the TA measurements on ZnO and CBP. Bottom: Spectra of pump and probe use for the TA measurements on QD.

represented by the 1st derivative of the original absorption spectrum [162,163]. From the similarities between the first two EA features, $\alpha 1$ and $\beta 1$, and the 1st derivative of a Gaussian, we hypothesize that the features $\alpha 1$ and $\beta 1$ (enlarged in Fig. 6-6(a)) are due to the QCSE of the 1S(e)-1S$_{3/2}$(h) QD state. To test this hypothesis, we simulate the change in the absorption spectrum by red-shifting a Gaussian absorption profile. The normalized absorption spectrum of the 1S(e)-1S$_{3/2}$(h) state at zero bias is shown in Fig. 6-6(b) and is obtained by fitting a Gaussian to the B1 feature of the QD TA spectrum (Fig. 6-4(b)) and then normalizing it with respect to its maximum. We obtain features similar to Fig. 6-6(a) by red-shifting this Gaussian by varying energies, with a shift of 40 meV generating EA features with amplitudes as much as half that of the Gaussian. Using this model, we predict the growth of $\alpha 1$ and $\beta 1$ as a function of voltage. Since the EL is an emission from the same 1S(e)-1S$_{3/2}$(h) state under consideration, we take the EL red-shift (Fig. 6-6(c)) as the red-shift of the Gaussian needed to simulate $\alpha 1$ and $\beta 1$ at each applied voltage. The EL red-shift is measured by fitting a double-Gaussian profile to the EL spectra [17] and taking the average of the two peak energies. Simulated $\alpha 1$, $\beta 1$, $\alpha 1+\beta 1$, and $\alpha 1-\beta 1$ (black solid lines, from top to bottom) are plotted in Fig. 6-6(d) with their experimental values. The simulated curves use 0.84% peak absorption for the Gaussian, which is the only fitting parameter used. The match between the amplitudes of the EA features predicted from the QCSE model and the experimentally observed amplitudes is evidence that the QCSE is the dominant cause of $\alpha 1$ and $\beta 1$ features.

We quantify the amount of charging from the asymmetry between the 1st exciton EA features. EA spectra at high voltages reveal a slightly larger $\beta 1$ than $\alpha 1$. This asymmetry can be due to reduced or dispersed 1S(e)-1S$_{3/2}$(h) oscillator strength from electric-field-induced quenching [14], broadening of the absorption feature [99], or charging [15, 157] of the QDs at high voltages. The asymmetry at 13 V can be reproduced if we reduce the amplitude of the shifted Gaussian by 5%. Even if we assume that all of the asymmetry is due to charging, this suggests that at most 10% of QDs are charged at 13 V. Assuming that the Auger recombination occurs only in QDs with an extra charge (and not QDs with an extra charge on neighboring QDs),

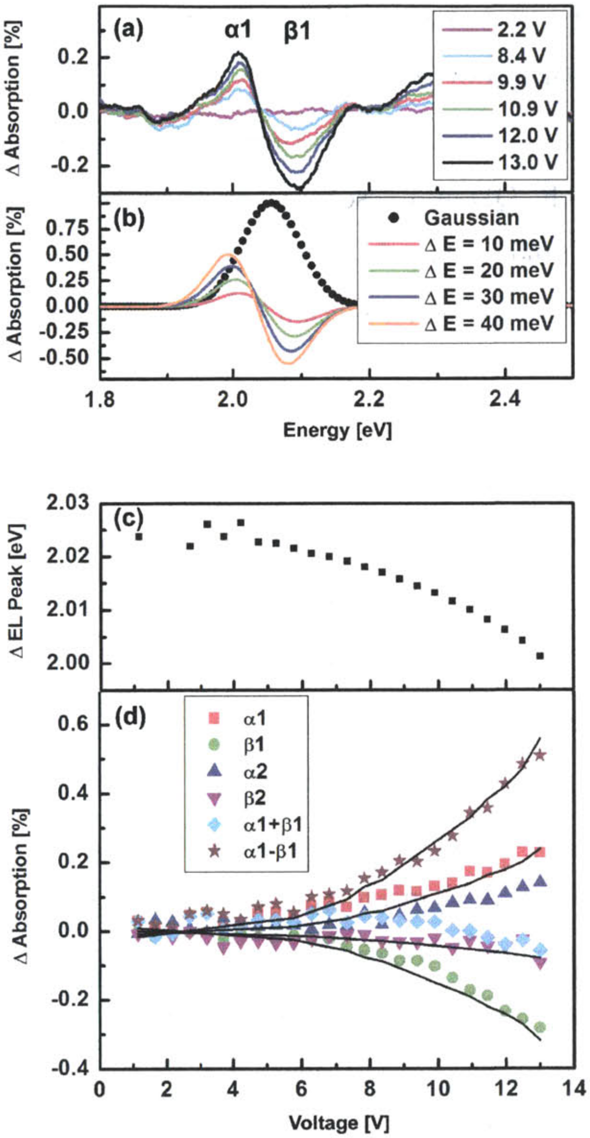

Figure 6-6: (a) The electroabsorption spectra of the QD-LED focused around $\alpha 1$ and $\beta 1$. (b) $\alpha 1$ and $\beta 1$ simulated by red-shifting a Gaussian absorption profile by varying energies. The Gaussian profile is obtained from fitting a Gaussian to the B1 feature in Fig. 6-4(b). (c) Peak energies of the EL spectra as a function of applied voltage. (d) Change in the four electroabsorption features as a function of applied voltage. The solid lines are the simulated change in the amplitudes of the electroabsorption features using the model described in the text.

the Auger recombination only explains 10% of the efficiency roll-off (of more than 60% at 13 V). This result supports our earlier assumption that there is no significant QD charging and that the Auger recombination is not a large contributing factor in the efficiency roll-off of these devices.

We have proposed in our earlier work three possible mechanisms by which the electric field can reduce the QD luminescence, two of which we find to be the possible cause of the efficiency roll-off [17]: a decrease in radiative exciton recombination rate (e.g. reduced electron-hole wavefunction overlap [153, 154]) or a decrease in the probability of forming bandedge excitons (e.g. hot charge carrier trapping by QD surface traps [16, 156]). Although our previous study [17] was not able to discern the change in the radiative rate, our present study suggests that the oscillator strength of the 1S(e)-$1S_{3/2}$(h) state (and hence the radiative rate) remains relatively unchanged during the efficiency roll-off. Therefore, improved understanding of the formation of bandedge excitons in the QDs under electric fields may be needed to mitigate the efficiency roll-off of these QD-LEDs.

Lastly, we note the presence of trapped charges in the QD-LED. Since each EA spectrum is taken after the voltage bias was turned off, our results indicate the presence of long-lasting electric field inside the device. We measure the electric field retention time by monitoring the decay of $\alpha 1$, $\beta 1$, $\alpha 2$, and $\beta 2$ after the voltage is turned off. Fig. 6-7 shows the dynamics of the four features as the device was biased from 0 to 13 V (t = -30 s) and then turned off (t = 0 s). All the features decay with a time constant of approximately 7 minutes. This time constant is much longer than discharge times seen for OLEDs, which often exhibit time constants ranging from micro-seconds [164] to tenths of a second [165]. Therefore, we associate the long discharge time, as seen similarly in QD charging devices [15], to the small amount of charge trapped in the QDs.

We have assumed that the origin of the electric field that causes the QCSE is predominantly due to the external bias. However, the long retention time of the EA features suggests that electric field due to local charges may be responsible for the QCSE. If 10% of QDs are indeed charged at 13 V, there may be a significant

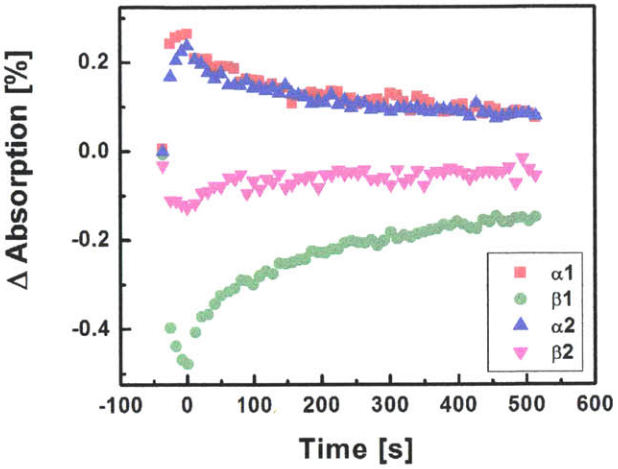

Figure 6-7: The dynamics of the four electroabsorption features as the device was biased from 0 to 13 V (t = -30 s) and then turned off (t = 0 s). The long retention time (~7 min) indicates that the electric field responsible for the EA features is due to trapped charges in the QD-LED.

contribution from the local electric field due to those charges. This may explain the QCSE visible in our EA measurements long after the voltage bias is turned off.

In conclusion, we measured the electroabsorption spectra of a biased QD-LED to understand the dynamics of charging and QCSE in the QD-LED and their relation to the efficiency roll-off. Comparison of these spectra to both the transient absorption and the linear absorption spectra indicate that the QCSE was present and that the charging of the QDs was too small to explain the efficiency roll-off. The electroabsorption features were visible for minutes after the voltage was turned off, suggesting that the field causing the QCSE may be due to the local electric field generated from the small amount of charging inside the device.

Chapter 7

Charging in QD-LEDs

Of many loss mechanisms present inside a QD-LED, we have proposed that the electric-field-induced quenching of the QDs is the dominant loss mechanism for QD-LEDs in the "high" current density regime. On the other hand, this means that the electric field is not a dominant factor governing the EQE at "low" or "optimal" current density regime. Then is the peak EQE determined by the product of the PL efficiency of the unperturbed QD film in the device and the photon out-coupling efficiency?

In this chapter, we present evidence for charging in the QD layer of a QD-LED that is a function of the QD layer thickness. We note that this is not in contradiction with the proposals made in the previous chapters, which indicate that the efficiency roll-off is not charging-induced; a QD-LED may be charged, but there is no *additional* charging from biasing the device. What we propose here is that the QD layer, upon operation, temporarily charges the QDs which may affect the peak EQE observed from the device. We fabricate QD-LEDs with three different QD layer thicknesses: 7, 14, and 28 nm. The peak EQE of these devices varies from 0.8%, for the device with the thickest QD layer, to 2.3%, for the device with the thinnest QD layer. Transient PL measurements of the QDs in these devices exhibit increased presence of Auger recombination for the thicker devices, which may explain their lower peak EQEs.

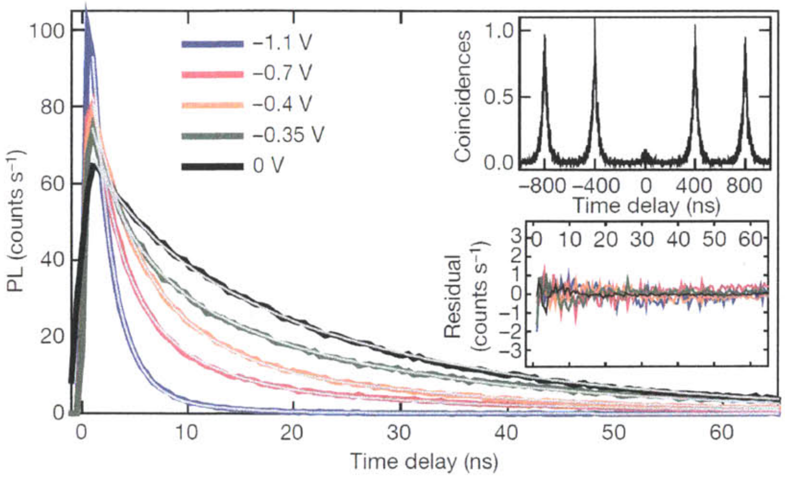

Figure 7-1: Transient PL of a single QD charged by an electrochemical setup. The negative voltage applied is correlated with the degree of charging and results in faster PL decay curves with more negative voltages. From Ref. [16]

7.1 Auger Recombination in QDs

As briefly mentioned in section 5.1, Auger recombination is a non-radiative exciton recombination mechanism that involves a third charge carrier. Instead of emitting a photon, the exciton non-radiatively transfers its energy to the carrier, which simply thermalizes to its ground state immediately after being excited. Introduction of this non-radiative recombination pathway results in reduced and faster PL decay as shown in the work by Galland *et al.* [16] (Fig. 7-1). The PL clearly exhibits shorter lifetimes for charged QDs: 24, 5, and 2 ns for neutral, singly charged, and doubly charged QDs respectively.

Due to the spatial confinement of the charge carriers, the Auger recombination rate is a function of the QD size. In particular, the Auger constant is QD radius, R, dependent and the overall Auger rate becomes proportional to R^{-3} [142]. Therefore, the Auger recombination can be an increasingly concerning loss mechanism for QD-LEDs with small QDs.

7.2 Auger Recombination in a QD-LED

There has long been a speculation that the efficiency of a QD-LED is limited by the Auger recombination resulting from poor electron-hole balance in the QDs. This speculation has been supported, for example, by the difference in the energy barriers for injecting electrons and holes into the QD [12], observation of temporary EQE quenching [97], and improved EQE by adding an electron impeding layer in a QD-LED [106]. However, to our knowledge, there has not been direct evidence for QD charging in a QD-LED.

From an experimental point of view, modifying the device structure to study the role of a single device parameter is often difficult. Device modification, often in the form of changing the material of one of the layers, can change more than the one parameter that is investigated. For example, studying the role of the energy barrier between the valence band of the QD and the HOMO of the hole transporting layer (HTL) by using different HTL materials [12] can be complicated by changes in other physical properties that come with using a different material. Changing the HTL can alter not only the hole injection barrier but also the hole mobility in HTL, the electron blocking barrier, and the hole carrier concentration. The chemical compatibility of the QDs with the HTL as well as its deposition method can also influence the underlying QDs and the morphology of the HTL itself. Therefore, changing the HTL or the electron transport layer to tune the electron-hole balance may not be a straight forward experiment.

Here, we study the most basic of device structure modifications: changing the thickness of the QD layer. By not introducing new materials into the device, we minimize the number of parameters we change in the system while still modifying the system. At first, this may seem like it will not change any device properties. However, as it will become clear, even this simple modification can dramatically change the device performance. The device investigated in this chapter is the same structure investigated in Chapter 6 with the exception of use of a 50 nm organic hole transport layer called Tris(4-carbazoyl-9-ylphenyl)amine (TCTA) instead of CBP.

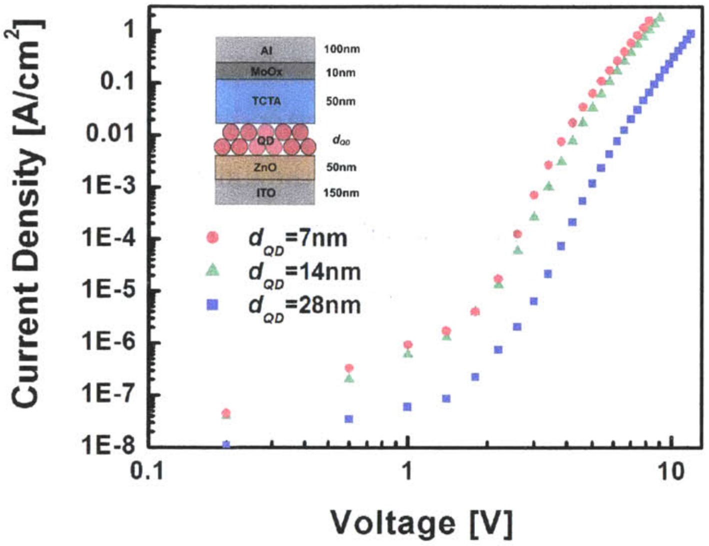

Figure 7-2: Current density-voltage characteristic of QD-LEDs with three different QD layer thicknesses: 7, 14, and 28 nm. Large dependence of the current-voltage characteristic on the QD layer thickness indicates that the QD layer poses a significant electrical resistance in the device. Inset: device structure of the QD-LED.

TCTA offers more morphological stability than CBP, which is thought to be a result of its higher glass transition temperature (T_g(TCTA) = 151°C compared to T_g(CBP) = 62°C [166]) [167]. The QD layer is spin-cast out of chloroform (1500 rpm, 3000 rpm/s) at concentrations of 5, 10, and 20 mg/ml, yielding film thicknesses, d_{QD}, of ~7, 14, and 28 nm, respectively.

The current density-voltage characteristics of these QD-LEDs are shown in Fig. 7-2. The diodes turn on at ~2 V, exhibiting space charge limited conduction before the turn-on and trap limited conduction after the turn-on. As expected, the current density is significantly reduced with the added resistance of thicker QDs. The dependence of current density-voltage on the QD layer thickness indicates that the QD layer is one of, if not, the most resistive layers in the device. Therefore, simply tuning the QD layer thickness may allow us to control the charge balance within the device.

The EQE-voltage characteristic of these QD-LEDs show peak EQEs of 2.3, 1.1, and 0.9% for d_{QD} = 7, 14, and 28 nm, respectively (Fig. 7-3, top). Considering

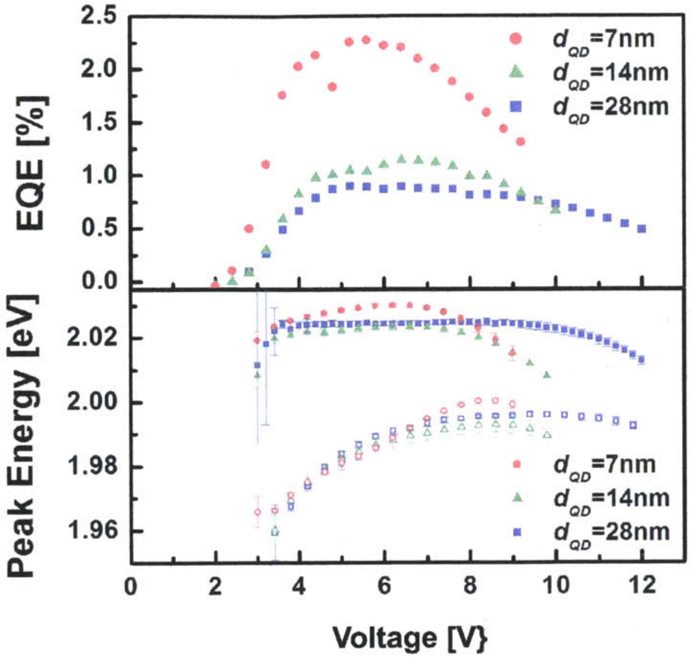

Figure 7-3: Top: EQE-voltage characteristic of the QD-LEDs. Bottom: EL peak energy-voltage characteristic of the QD-LEDs. The EL peak energies are obtained by fitting double-Gaussian to the EL spectra. The EQE roll-off tracks the EL peak energy roll-off as explained in section 5.1.

that the material set and the fabrication process are identical for the QD-LEDs, it is interesting that varying the QD layer thickness can drastically change the peak EQE. We hypothesize, and later show, that different QD layer thicknesses result in different degrees of QD charging, which may be causing the different EQEs. The bottom of Fig. 7-3 shows the EL peak energies of the QD-LEDs as function of the applied voltage bias by performing the double-Gaussian fit discussed in section 5.1. For each QD-LED, the higher EL peak energies roll off the same way their EQEs roll off. This observation is consistent with our previous analysis which indicates that the roll-off is due to electric-field-induced quenching of QD luminescence, the magnitude of which can be monitored through the QCSE.

We now return to the question initially posed in this chapter: what determines the peak EQE. Amongst many possible factors, observation of the peak EQE's dependence on the QD layer thickness suggests that the PL efficiency of the QDs in these

QD-LEDs are different despite the identical device structure and the fabrication process. Given that the peak EQE occurs before the EL-peak shift, electric-field-induced luminescence quenching seems unlikely. Therefore, we investigate a likely, and the most widely speculated, loss mechanism of QDs: Auger recombination due to charged QDs.

To test the hypothesis, we measure the transient PL of the QDs in the QD-LEDs before and after device operation. Once again, we excite the QDs with a 150 fs pulsed laser at $\lambda = 530$ nm (SuperK, 40 MHz repetition rate) and collect the PL with a streak camera. The "device operation" was a 2s operation of the QD-LEDs at 1 A/cm^2. The resulting normalized QD transient PL curves are shown in Fig. 7-4.

Each QD-LED exhibits a bi-exponential behavior with larger contribution from the faster decay component after the operation of the device. The QD-LEDs also show larger contribution from the faster decay component for thicker QD layers, both before and after the device operation. We fit the transient curves to a bi-exponential convolved with the instrument response function (not shown). As an example, the fit to the transient curve for the device with 28 nm thick QD layer is shown in Fig. 7-4. The bi-exponential consists of a fast component with $\tau \approx$ 0.4 ns and a slow component with $\tau \approx 9$ ns (equation shown in the inset). These values are in agreement with the Auger recombination rates observed by previous reports [157]. Increased contribution from the fast component upon device operation is also consistent with the idea of injected charges temporarily residing in the QDs. Therefore, we attribute the the fast decay component to the emission from charged QDs and the slow decay component to the emission from neutral QDs. Assuming the charging occurs at the cores of the QDs (instead of surface traps), the fraction of the QDs charged in the film can be calculated from the relative intensities of the two decay components. Under this assumption, we calculate the fraction of charged QDs simply from

$$FractionCharged = \frac{B/2}{A + B/2}, \tag{7.1}$$

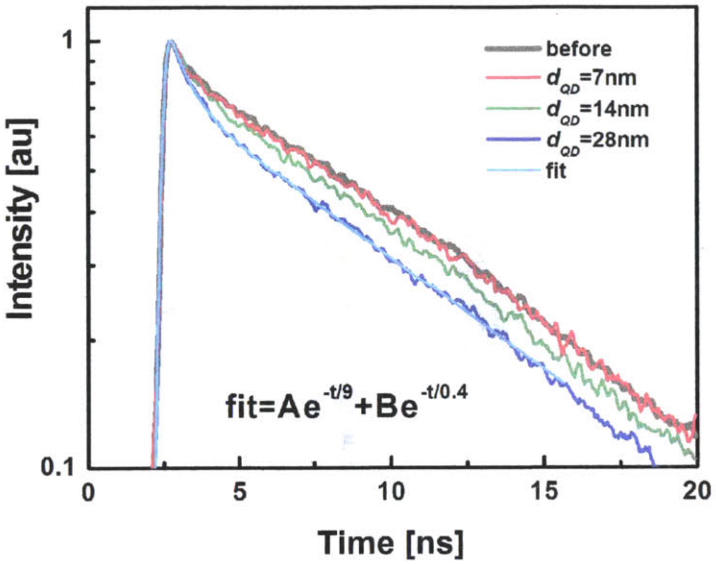

Figure 7-4: Transient PL of QDs in the QD-LEDs before and after a 2s operation at 1 A/cm^2. The PL transients exhibit a stronger bi-exponential behavior after operation with the strongest bi-exponential behavior observed from the QD-LED with the thickest QD layer. Dotted curve is an example bi-exponential fit to this PL transient curve.

where A and B are the coefficients of the bi-exponential fit as shown in the equation on Fig. 7-4. $B/2$ in equation 7.1 corrects for the extra charge that can also contribute to the radiative recombination [16]. For example, having two electrons and one hole in a QD results in two degenerate bandedge exciton states.

The fraction of QDs charged, calculated from equation 7.1, for all the QD-LEDs is shown in Fig. 7-5. In general, thicker QD layers exhibit larger fractional charging and that charging is increased upon device operation. We note that the trend of increasing fractional charging and decreasing EQE with QD film thickness is consistent with the presence of the Auger recombination. Therefore, we attribute the dependence of EQE on QD film thickness to the amount of charging present in the QD films. However, the EQE is not directly proportional to the fraction of uncharged QDs. This may be due to non-uniform distribution of the charges within the QD film.

Lastly, if the QD layer is indeed charging, is it temporary? In other words, is the change in the QD film reversible, as to be expected from a temporary charging

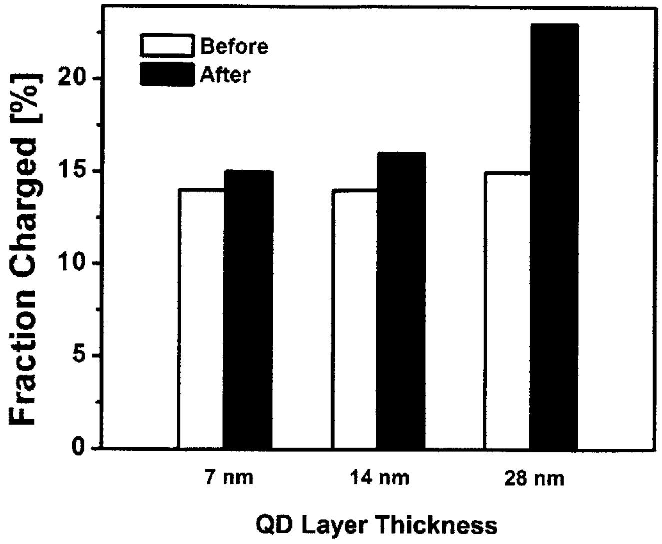

Figure 7-5: Fraction of the QDs charged in the QD-LEDs before and after the operation. The values are calculated from the bi-exponential fits to the QD PL transient curves as described in the text.

event. We monitored the charging state of the thickest QD-film device after the device operation. The result, shown in Fig. 7-6, shows a charge retention time constant on the order of hours, and days for a full discharge. This observation of discharging in a QD-LED is consistent with the observation reported by Anikeeva *et al.*; the peak EQE of a QD-LED decreases upon operation but is recovered after a day [97].

Chapters 5 and 6 have argued the importance of electric-field-induced QD luminescence quenching over the Auger recombination in the high current density regime. However, this *does not imply* that Auger recombination is not present at the high-current-density regime. Rather, these experiments indicate that the Auger recombination is present at any current density *including* the high-current-density regime, while the electric-field-induced quenching is *only* present at the high-current-density regime.

In conclusion, through QD transient PL measurements, we observed charging of the QDs in QD-LEDs with various QD layer thicknesses by monitoring the contribution from the fast decay component of the bi-exponential PL decay curves. QD-LEDs

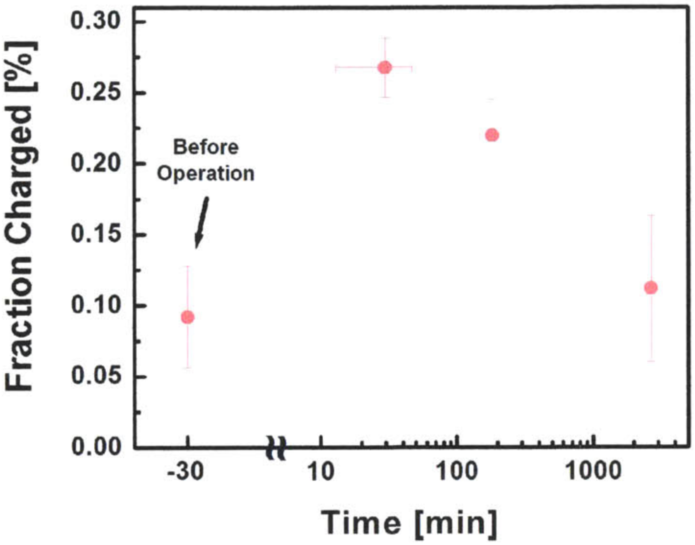

Figure 7-6: QD charging fraction for the QD-LED with 28 nm QD layer before and after the operation (t=0). The QDs remain charged for hours and are not fully discharged to its original state for days.

with thicker QD layers exhibit larger fractions of the QDs charged, which we hypothesize is the cause of their reduced peak EQE. The retention time of these charges is observed to be several hours to a day, which is in agreement with the temporary EQE quenching of a QD-LED previously reported.

Chapter 8

Conclusions and Outlook

8.1 Thesis Summary

Saturated and tunable emission colors make QD-LEDs interesting for the next generation of display and lighting technologies. However, there still remain various hurdles to commercialization of QD-LEDs, including their relatively low efficiencies in comparison to alternative technologies. In order to address these obstacles, we must first deepen our understanding of the mechanism by which these devices operate.

In this thesis, we study some of the efficiency loss mechanisms present in the latest generation of QD-LEDs. We start with understanding the origin of reduced efficiencies at high-current-density operation of these devices. This phenomenon, known as the efficiency roll-off, is a widely observed behavior for all kinds of LEDs, and QD-LED is not an exception. The possible causes of the efficiency roll-off fall under two broad categories: reduced luminescence efficiency of the QDs and charge carrier leakage. Through measurements of simultaneous QD EL and PL efficiencies during device operation, we identify the reduced luminescence efficiency of the QDs at high current densities to be the cause for the efficiency roll-off. We observe that an EQE roll-off of 50% as the device was biased to a high voltage is accompanied by the corresponding roll-off in the PL efficiency of the QDs.

Having established that the luminescence efficiency of the QDs is the cause of the roll-off, we then study the reason for this reduced luminescence efficiency. In forward bias, these QD-LEDs exhibit red-shifting of the EL spectra, indicative of QCSE. The comparison of QD EL spectra taken under forward bias and PL spectra taken under reverse bias suggests that this reduced luminescence efficiency is indeed caused by the electric-field-induced quenching of the QD PL efficiency. We use the relationship between PL peak-shifts and PL quenching of QDs subject to the QCSE observed while reverse biasing a QD-LED to predict the efficiency roll-off in forward bias. The roll-off predicted by this analysis is in excellent agreement with our experimental data and correctly traces an EQE reduction of nearly 50%. While other loss mechanisms, such as Auger recombination due to charging, are present, we find that this electric-field-induced quenching effect alone is strong enough to explain the roll-off.

We complement the EL-PL study with electroabsorption spectroscopy measurements of a biased QD-LED to confirm that the charging of the QDs is not voltage bias dependent, and thus unrelated to the roll-off. Comparison of the electroabsorption spectra to both the transient absorption and the linear absorption spectra indicate that the QCSE is present and that the charging of the QDs is too small to explain the efficiency roll-off. Therefore, the electroabsorption measurements confirm that the electric-field-induced quenching of the QD PL is the cause for the efficiency roll-off in QD-LEDs.

Finally, we study the effect of Auger recombination in QD-LEDs. We compare peak EQEs of QD-LEDs with varying QD layer thicknesses while also studying their QD transient PL. QD-LEDs with thicker QD layers exhibit lower peak EQEs and transient PL with stronger bi-exponential behavior. We attribute the strength of the bi-exponential behavior to the fraction of QDs charged in the device. Fast and slow components of the transient PL have decay lifetimes of 0.4 and 9 ns, respectively, which are consistent with the lifetimes of charged and neutral QDs reported. Therefore, we propose that the low EQE of the QD-LEDs with thick QD layers is due to increased charging of the QDs. We find that, once charged, these QDs retain the charges for hours.

8.2 Outlook

Through the study of the loss mechanisms, we hope to have brought better understanding to how these QD-LEDs operate. However, there are still many hurdles to address before the commercialization of QD-LEDs can be realized. We list here some topics that, we believe, need further investigation to bring better understanding to these devices and to take QD-LEDs one step closer to commercialization.

- Temperature dependence of a QD-LED — As discussed briefly in section 5.1, we expect QD-LEDs to heat up the same way OLEDs do. Heating can not only reduce the luminescence efficiency of the QDs but can also reduce the longevity of the devices. Although our measurements were performed quickly enough to have negligible heating effects, practical use of the QD-LEDs will require prolonged operation times. Therefore, monitoring the steady-state junction temperature as a function of the current density would be valuable information for knowing the limits of high-brightness operation in QD-LEDs.

- Low EQE at low-current-density regime — Due to the resistive and relatively degradation prone nature of QD-LEDs, practical applications of QD-LEDs probably rely on their operation at the low current density regime. However, unlike OLEDs, most QD-LEDs exhibit low efficiencies at low current densities. Low EQEs at low current densities are often attributed to leakage currents through the device. Therefore, a study on the source of this leakage current would be valuable.

- Charge balance — We have observed characteristics of Auger recombination in our QD-LEDs, which occurs from charging of the QDs. This suggests that the EQE may be improved with a more balanced electron and hole injection into the QDs. However, the past attempts have been hindered by the lack of wide bandgap organic materials with LUMO comparable to that of QDs. Recent studies on PbS quantum dots have shown that the use of appropriate ligands can enable surface dipoles and shift the energy levels of the QDs. Therefore, use of these surface dipoles may be an alternative method of achieving a more balanced charge injection.

- Transient absorption measurements of QDs under electric field — In this thesis we have identified electric-field-induced quenching of QD PL to be the source of the efficiency roll-off. However, the exact mechanism by which the electric field quenches the QD PL is not yet clear. One method that may potentially offer the answer to this problem is transient absorption spectroscopy. Transient absorption spectroscopy has been able to elucidate the exciton relaxation dynamics in QDs on a sub-*ps* time scale by monitoring the change in its absorption spectrum. Similar analysis on QDs under varying electric fields may be insightful.

- Photon out-coupling — One of the universal problems with all kinds of LEDs is the photon out-coupling efficiency. In QD-LEDs, only 20% of the generated photons are estimated to be emitted out of the device, which severely limits the overall efficiency. Therefore, a clever scheme to attain better photon extraction efficiency with simple modifications is of paramount importance.

Appendix A

QD-LED Fabrication Procedure

We provide here the step-by-step procedure to produce the QD-LED used in this thesis.

A.1 QD Solution Preparation

The QDs used are CdSe core-shell QD with a peak wavelength at 610 nm from QD Vision Inc. The QDs are generally dissolved in hexane using carboxylic acid ligands. Since the solutions are too rich in ligands to be used as delivered, we perform the following purification procedure.

1. Take 0.8 ml of the original QD solution into a new vial
2. Add 0.2 ml of butanol and stir
3. Add 1.5 ml of methanol and stir
4. Use a centrifuge to separate the QD precipitate from the solution (3500 rpm, 5 min)
5. Pour out the solution, leaving the precipitate in the vial
6. Add 0.8 ml of hexane into the vial and redissolve the precipitate
7. Repeat the crash-out procedure: add 0.2 ml of butanol and stir

8. Add 1 ml of methanol and stir
9. Use a centrifuge to separate the precipitate from the solution (3500 rpm, 5 min)
10. Pour out the solution, leaving the precipitate in the vial
11. Dry out the vial (at least 30 min)
12. Redissolve the QD into chloroform (or a different solvent of choosing)

A.2 Substrate Preparation

The substrates used to make the QD-LED are ITO (150 nm) coated glass substrate acquired from commercial companies. They are cleaned with the following procedure.

1. Sonicate in de-ionized (DI) water for 5 min
2. Rinse in DI water
3. Repeat steps (1) and (2)
4. Sonicate in acetone for 2 min
5. Repeat step (4) using fresh acetone
6. Immerse in boiling isopropanol for 2 min
7. Repeat step (6) using fresh isopropanol
8. Blow dry the substrates with N_2 gas

A.3 QD-LED Fabrication

The QD-LED is fabricated on top of the clean ITO substrates prepared in section A.2 using the following procedure.

1. Expose the substrates to O_2 plasma for 1 min

2. Deposit 50 nm of ZnO on the substrates. This can be done either by sputtering or spin coating:

    - Sputtering:
        - Growth conditions: rate = 0.6 A/s, power = 150 W, gas = Ar, flow rate = 10 sccm, pressure = 4 mTorr
    - Spin coating:
        (a) Spin-coat zinc acetate solution in a N_2 environment (2000 rpm, 1500 rpm/s, 20 sec, 60 μl solution per spin)
        (b) Anneal on a hotplate (300°C) for 5 min in a dry air environment (10 $\sim$ 20% humidity)
        (c) Rinse the film by spin-coating Methoxyethanol (MeOOH) (2000 rpm, 1500 rpm/s, 20 sec, 90 μl solution per spin)
        (d) Rinse the film by spin-coating Methanol (MeOH) (2000 rpm, 1500 rpm/s, 20 sec, 90 μl solution per spin)

3. Spin-coat the QD layer. The following spin-coating condition yields a $\sim$ 10 nm QD film. The thickness of the film can be scaled with the QD concentration in the solution.

    - Spin-coating condition: 10 mg/ml QD solution in chloroform, 50 μl solution per spin, 1500 rpm, 3000 rpm/s, 60 sec.

4. Thermally evaporate the following layers at 1 $\sim$ 2 A/s:

    - 100 nm CBP (or TCTA)
    - 10 nm MoO_x
    - 100 nm Al

Appendix B

Supplementary Information

B.1 Förster Resonance Energy Transfer

Förster resonance energy transfer (FRET), also known as fluorescence resonance energy transfer, is a widely known phenomenon that is particularly important in explaining how some excitons can migrate from one molecule to another. A molecule that can emit a photon has a transition dipole, which represents the strength of oscillating current within the molecule as it tries to emit a photon. This oscillating current, just like a dipole antenna, generates an oscillating near-field that can excite a nearby molecule within the reach of the field the same way a photon can excite that molecule.

Because of its importance we would like to give here a derivation of FRET rate, which can be useful in understanding the physical origin of its dependence on the parameters that constitute the formula. For example, the following is an abridged version of the derivation presented by Madigan *et al.* [168] with some modifications. The derivation can roughly be broken up into following parts: (1) Calculate the perturbation Hamiltonian. (2) Apply time-dependent perturbation theory. (3) Replace used variables with experimentally measurable parameters.

Let us consider a system consisting of two molecules: a donor molecule (initially in its excited state) and a nearby acceptor molecule (initially in its ground state). The goal is to calculate the rate at which the exciton is transferred from the donor molecule to the acceptor molecule. We start with the electric potential due to a distribution of charges inside the excited donor molecule using multipolar expansion:

$$V(\vec{r}) = \frac{1}{4\pi\epsilon}\left[\frac{q}{r} + \frac{\vec{\mu}_D \cdot \hat{r}}{r^2} + \frac{1}{2}\frac{(\bar{Q}\hat{r})\cdot\hat{r}}{r^3} + \cdots\right], \tag{B.1}$$

where $\mu_D = \sum_i q_i \vec{r}_i$ is the dipole of the donor molecule. Since the molecules are charge neutral, the first term is zero. We use the dipole approximation and assume the second term is dominant over the higher order terms. Then the resulting electric potential is

$$V(\vec{r}) \approx \frac{1}{4\pi\epsilon}\frac{\vec{\mu}_D \cdot \hat{r}}{r^2}. \tag{B.2}$$

The electric field generated by this donor molecule is simply then

$$\vec{F}(\vec{r}) = -\nabla V(\vec{r}) = \frac{3\hat{r}(\vec{\mu}_D \cdot \hat{r}) - \vec{\mu}}{4\pi\epsilon r^3}. \tag{B.3}$$

This electric field "perturbs" the acceptor molecule by interacting with its dipole. The interaction energy, also called the perturbation Hamiltonian, is calculated from $-\vec{F} \cdot \vec{\mu}_A$. The resulting perturbation Hamiltonian is then

$$\Delta H = \frac{\vec{\mu}_D \cdot \vec{\mu}_A - 3(\vec{\mu}_D \cdot \hat{R})(\vec{\mu}_A \cdot \hat{R})}{4\pi\epsilon R^3}, \tag{B.4}$$

where $\vec{R}$ is the position of the donor molecule with respect to the acceptor molecule.

Now, the initial state of the system is the donor in its excited state and the acceptor in its ground state,

$$|\psi(t=0)\rangle = |e, g\rangle, \tag{B.5}$$

where $|e,g\rangle = |e(\vec{r}_D)\rangle\,|g(\vec{r}_A)\rangle$. Then we can apply the first order time-dependent perturbation theory [81] to this state using the perturbation Hamiltonian calculated in equation B.4 to calculate the rate at which the state acquires the energy transfered state, $|g,e\rangle$, character. The state of the system after time t is then

$$|\psi(t)\rangle = |e,g\rangle + \left[\frac{1}{i\hbar}\int_0^t \langle e,g|\, \Delta H \,|g,e\rangle\, dt'\right] |g,e\rangle\,, \tag{B.6}$$

Probability that the acceptor is excited at time t is then

$$\begin{aligned} P(t) &= |\, \langle g,e|\psi(t)\rangle \,|^2 \\ &= \frac{1}{\hbar^2}|\, \langle g,e|\, \Delta H \,|e,g\rangle \,|^2 \left| \int_0^t e^{i\omega_{DA}t'} \right|^2 \\ &= \frac{1}{\hbar^2}|\, \langle g,e|\, \Delta H \,|e,g\rangle \,|^2 \left[\frac{sin(\omega_{DA}t/2)}{\omega_{DA}/2}\right]^2 . \end{aligned} \tag{B.7}$$

ω_{DA} is angular frequency such that $\hbar\omega_{DA}$ is the energy difference between the donor transition and the acceptor transition (i.e. when the bandgaps of the two molecules are equal, ω_{DA} is zero). Calculating the matrix element, this equation can be rewritten as:

$$P(t) = \frac{1}{\hbar^2}\kappa \frac{\left|\langle\mu_D\rangle_{ge}\right|^2 \left|\langle\mu_A\rangle_{eg}\right|^2}{16\pi^2 n^4 \epsilon_0^2 R^6} \left[\frac{sin(\omega_{DA}t/2)}{\omega_{DA}/2}\right]^2 . \tag{B.8}$$

κ is a geometrical term that depends on the orientation of the donor dipole respect to the acceptor dipole:

$$\kappa = \langle\hat{\mu}_D\rangle_{ge} \cdot \langle\hat{\mu}_A\rangle_{ge} - 3\left(\langle\hat{\mu}_D\rangle_{ge} \cdot \hat{R}\right)\left(\langle\hat{\mu}_A\rangle_{ge} \cdot \hat{R}\right). \tag{B.9}$$

Equation B.8 calculates the probability that the acceptor molecule is excited after time t for a system with single initial state ($|e,g\rangle$) and a single final state ($|g,e\rangle$). However, in reality, there is a distribution of initial and final states due to the presence of phonons for T > 0 K. For a system with a single initial state and a distribution of final states, equation B.8 must be integrated over all ω_{DA} and multiplied by the density of the final states [81]:

$$P(t) = \frac{2\pi}{\hbar^2}\kappa^2 \frac{\left|\langle\mu_D\rangle_{ge}\right|^2 \left|\langle\mu_A\rangle_{eg}\right|^2}{16\pi^2 n^4 \epsilon_0^2 R^6} \rho_D^{g*}(\omega)\rho_A^{e*}(\omega)t \tag{B.10}$$

where $\rho_D^{g*}(\omega)$ and $\rho_A^{e*}(\omega)$ are the density of states for the donor in ground state and the acceptor in excited state, respectively. The $*$ on $g*$ and $e*$ indicates that they are not in their equilibrium states and the nuclear arrangement is still that of the excited state for the donor and the ground state for the acceptor. The transition rate is then the derivative of $P(t)$, which is:

$$\Gamma = \frac{2\pi}{\hbar^2}\kappa^2 \frac{\left|\langle\mu_D\rangle_{ge}\right|^2 \left|\langle\mu_A\rangle_{eg}\right|^2}{16\pi^2 n^4 \epsilon_0^2 R^6} \rho_D^{g*}(\omega)\rho_A^{e*}(\omega). \tag{B.11}$$

Finally, for a system with both a distribution of initial and final states, the transition rate is calculated by multiplying equation B.11 by the probability that the donor is in the excited state with energy $\hbar\omega$, $\rho_D^e(\omega)\rho_A^g(\omega)$, and integrating over all ω. After some rearrangements of the terms, the transition rate becomes:

$$\Gamma = \frac{1}{8\pi\hbar^2 n^4 \epsilon_0^2}\frac{\kappa^2}{R^6}\int \left[\rho_D^e(\omega)\left|\langle\mu_D\rangle\right|^2 \rho_D^{g*}(\omega)\right] \cdot \left[\rho_A^g(\omega)\left|\langle\mu_A\rangle\right|^2 \rho_A^{e*}(\omega)\right] d\omega. \tag{B.12}$$

Now we must relate the relate the above equation with experimentally measurable parameters. The emission and absorption rate of a molecule for a two level system with an energy separation of ω_0 can be written as [81],

$$\begin{aligned} \Gamma^{\downarrow} &= A(\omega)\delta(\omega - \omega_0) \\ \Gamma^{\uparrow} &= BE(\omega)\delta(\omega - \omega_0) \end{aligned} \tag{B.13}$$

where $E(\omega)$ is the energy density in the fields given in units of [J m^{-3} rad^{-1}], and A and B are the *Einstein's coefficients* give by,

$$\begin{aligned} A &= \frac{\omega_0^3}{3\pi\epsilon_0\hbar c^3}\left|\langle\mu_D\rangle\right|^2 \\ B &= \frac{\pi}{3\epsilon_0\hbar^2}\left|\langle\mu_A\rangle\right|^2. \end{aligned} \tag{B.14}$$

For a molecule with a distribution of initial and final states, equation B.13 is modified by replacing $\delta(\omega - \omega_0)$ with $\rho_D^e(\omega)\rho_D^{g*}(\omega)$ for the emission and with $\rho_A^g(\omega)\rho_A^{e*}(\omega)$ for the absorption.

Let us start with $\Gamma^{\downarrow}$, which can be related to the emission spectrum of the donor molecule. The emission spectrum of the donor molecule normalized by the area, $F(\omega)$, represents the emission spectrum of a single photon, which is emitted after a period of the donor exciton lifetime, τ_D. Therefore, the rate at which the donor emits a photon, as a function of ω, is given by,

$$\Gamma^{\downarrow} = \frac{F(\omega)}{\tau_D} \tag{B.15}$$

We can now equate equations B.13 and B.15. After some rearrangement of the terms, we obtain,

$$|\langle\mu_D\rangle|^2 \rho_D^e(\omega)\rho_D^{g*}(\omega) = \frac{3\pi\epsilon_0\hbar c^3}{\tau_D}\frac{F(\omega)}{\omega^3}. \tag{B.16}$$

which is the first bracket inside the integral in equation B.12.

Next we work with $\Gamma^{\uparrow}$, which can be related to the absorption cross section of the acceptor molecule. We start with the differential equation form of the Beer-Lambert law,

$$\frac{dI(\omega)}{dx} = \left[-\sigma_A(\omega)N\right]I(\omega) \tag{B.17}$$

where I is the irradiance per unit frequency interval given in units of [W m^{-2} s rad^{-1}] and N is the density of of the acceptor molecules. Physically, equation B.17 is energy absorbed by a film of acceptor molecules per unit volume. This is just a product of $\hbar\omega$, rate at which an acceptor molecule absorbs photons, and the density of these acceptor molecules. Therefore, we can relate equation B.17 to $\Gamma^{\uparrow}$ as,

$$\begin{aligned} \hbar\omega N\Gamma^{\uparrow} &= \left[\sigma_A(\omega)N\right]I(\omega) \\ &= \left[\sigma_A(\omega)N\right]cE(\omega) \end{aligned} \tag{B.18}$$

where, in the second equality, we used the fact that I is energy density times the speed at which it travels, which is the speed of light, c. Now we can combine bottom equation of B.13 and B.18 and, after some rearrangement of terms, we arrive at,

$$|\langle\mu_A\rangle|^2 \rho_A^g(\omega)\rho_A^{e*}(\omega) = \frac{3\epsilon_0\hbar c}{\pi}\frac{\sigma(\omega)}{\omega} \tag{B.19}$$

which is the second bracket inside the integral in equation B.12. Plugging equations B.16 and B.19 into B.12, we finally obtain the FRET rate:

$$\Gamma_{FRET} = \frac{9c^4\kappa^2}{8\pi n^4\tau}\frac{1}{R^6}\int\frac{F_D(\omega)\sigma_A(\omega)}{\omega^4}d\omega. \tag{B.20}$$

Typically, an average FRET rate is calculated for an ensemble of donor and acceptor molecules where each dipole is oriented randomly. In this case, the geometrical factor, κ^2 is 2/3. Lastly, equation B.20 is often more concisely written as,

$$\Gamma_{FRET} = \frac{1}{\tau}\left(\frac{R_F}{R}\right)^6, \tag{B.21}$$

where R_F, known as the Förster radius, is calculated from,

$$R_F^6 = \frac{3}{4\pi}\frac{c^4}{n^4}\int\frac{F_D(\omega)\sigma_A(\omega)}{\omega^4}d\omega. \tag{B.22}$$

The significance of R_F is that it represents the distance at which the FRET rate is equal to the donor molecule's natural exciton lifetime. One case study of the FRET rate between organic molecules is given in Ref. [169].

B.2 Space-Charge-Limited and Trap-Filled Limit Conduction

Just like OLEDs, the current-voltage characteristics of QD-LEDs generally follow power laws after the diodes turns on. A power law with an exponent greater than two is indicative of conduction through an insulating material with traps, called the trap-filled limit (TFL) conduction, where the exponent is determined by the depth of the trap states in energy [170]. In the limit that there is no trap state, or the trap states are very shallow, the exponent is two, and the conduction is called the space-charge-limited (SCL) conduction [171, 172]. We show here examples of SLC conduction, for a vacuum diode and a trap-free insulator, to provide some insights into the reasons behind this nonlinear behavior. These two examples are provided by Rose *et al.* in Ref. [171], but here we wish to use a slightly different approach.

For a vacuum diode, the current density, J, through the diode is given by,

$$\begin{aligned} J &= qnv \\ &= \epsilon(\nabla E)v, \end{aligned} \tag{B.23}$$

where q is the elementary charge and v is position dependent velocity of the charges. The second equality comes from using Gauss's law,

$$\rho = qn = \epsilon\nabla E, \tag{B.24}$$

where ρ is charge density, and E is the electric field. The velocity of the charges can be related to the electric field by using the conservation of energy:

$$\begin{aligned} \frac{1}{2}mv^2 &= q\int_0^x E(x')dx' \\ v &= \left[\frac{2q}{m}\int_0^x E(x')dx'\right]^{\frac{1}{2}}, \end{aligned} \tag{B.25}$$

where m is the mass of an electron. By inserting the above equation into equation B.23, we obtain,

$$J = \left[\frac{2q}{m}\int_0^x E(x')dx'\right]^{\frac{1}{2}} \epsilon\nabla E. \tag{B.26}$$

Now, assume we have a function, $f(x)$, that satisfies the following two conditions:

$$\begin{aligned}&(1)\left[\int_0^x f(x')dx'\right]^{1/2}\nabla f(x) = constant, c\\&(2) -\int_0^1 f(x)dx = 1.\end{aligned}\tag{B.27}$$

The reason for these conditions will become apparent. Then $E(x)$ can be written using $f(x)$ as follows:

$$E = \frac{V}{L} f\left(x/L\right),\tag{B.28}$$

where V is the voltage across the film and L is the thickness of the film. There are two conditions that this $E(x)$ must satisfy:

$$\begin{aligned}&(1)V = -\int_0^L E(x')dx'\\&(2)J(x) = constant.\end{aligned}\tag{B.29}$$

The first condition simply states that the integration of the electric field from $x = 0$ to $x = L$ must equal to the voltage applied across the film. The second condition implies that there cannot be any charge building up in the film, over time, at steady state. The first condition is satisfied by B.27(2). We can see that the second condition is met by calculating the J:

$$\begin{aligned}
J &= \epsilon\left[\frac{2q}{m}\int_0^x \frac{V}{L}f(\frac{x'}{L})dx'\right]^{\frac{1}{2}}\frac{V}{L}\frac{1}{L}|\nabla f|_{\frac{x}{L}} \\
&let\ y = \frac{x}{L},\ y' = \frac{x'}{L} \\
&= \epsilon\left[\frac{2q}{m}\int_0^y \frac{V}{L}f(y')Ldy'\right]^{\frac{1}{2}}\frac{V}{L}\frac{1}{L}\nabla f(y) \\
&= \epsilon\left[\frac{2q}{m}\right]^{\frac{1}{2}}\left[\int_0^y f(y')dy'\right]^{\frac{1}{2}}\nabla f(y)\frac{V^{\frac{3}{2}}}{L^2} \\
&= \epsilon\left[\frac{2q}{m}\right]^{\frac{1}{2}}c\frac{V^{\frac{3}{2}}}{L^2},
\end{aligned}\tag{B.30}$$

where we have used B.27(1) in the last step. This shows that the second condition is also met. What is important here is that $J \propto \frac{V^{\frac{3}{2}}}{L^2}$. It is clear from the derivation that $V^{\frac{1}{2}}$ comes from the velocity's dependence on V and another V from the charge density's dependence on V.

For an insulator, we replace the first condition in B.27 with $f(x)\nabla f(x) = constant,\ c$, and the current density through the film is given by,

$$J = q\mu nE. \tag{B.31}$$

Using the same trial solution for electric field (B.28) and following the same steps performed to derive the current density for the vacuum diode, we find the current density for an insulator:

$$J = \mu c\frac{V^2}{L^3}. \tag{B.32}$$

In this case, $\frac{V}{L}$ contribution comes from the electric field and $\frac{V}{L^2}$ contribution comes from the charge density. This type of behavior is observed when conducting through organic thin films. We also see this behavior in our devices, for example, in Fig. 3-6 before the turn-on of the diode.

Typically, however, organic and quantum-dot thin films have trap states that can hinder charge conduction and alter the SLC conduction described above. In this TFL conduction regime, J-V curve obeys a power law with exponent greater than two. For an exponential trap distribution of

$$n_t \propto e^{-E/kT_c}, \tag{B.33}$$

where T_c is the characteristic temperature of the exponential trap distribution, the J-V relationship becomes [170, 173]

$$J \propto \frac{V^{m+1}}{L^{2m+1}} \tag{B.34}$$

where $m = T_c/T$.

In all of the above calculations, the μ was assumed to be a constant. However, it is known that, for some materials, the charge mobility is a function of the electric field [174]. Therefore, extracting values for physical parameters like mobility and trap depth from the J-V curve may not be straight forward.

B.3 Coulomb attraction

The third term in Equation 2.11, the Coulomb attraction, is a standard electric potential energy with a coefficient of 1.8. This 1.8 results from assuming the electron and hole are both in their respective $1S$ state (lowest excited state). Therefore, following the first order perturbation theory, the Coulomb energy can be calculated from

$$\Delta E = \langle \psi_e, \psi_h | \frac{-q^2}{4\pi\epsilon|\vec{r_e} - \vec{r_h}|} | \psi_e, \psi_h \rangle, \tag{B.35}$$

where $\psi_{e/h}$ is the wavefunction for a electron/hole in its $1S$ state and is given by

$$\psi_{e/h} = \frac{1}{\sqrt{2\pi a}} \frac{sin(\pi r/a)}{r}. \tag{B.36}$$

B.4 Modeling QD PL quenching in section 5.2

We derive here the equation we used to fit the QD photoluminescence (PL) intensities in Fig. 5-7(a). We note that neither this fitting equation nor the meaning of the curve is essential to the EQE prediction procedure or the conclusion drawn in chapter 5. In the end, the EQE prediction procedure only requires a curve that traces the dependence of the QD PL intensities on the applied voltage bias.

We start with the three equations given in the work by Park *et al.* to explain electric-field-induced quenching of QD photoluminescence:

$$\Delta E_i = \Delta E_0 + \mu \cdot F + \frac{q^2}{4\pi\epsilon}\left(\frac{1}{|\vec{r}_{ct,+} - \vec{r}_{t,+}|} - \frac{1}{|\vec{r}_{ct,+} - \vec{r}_{t,-}|} - \frac{1}{|\vec{r}_{ct,-} - \vec{r}_{t,+}|} + \frac{1}{|\vec{r}_{ct,-} - \vec{r}_{t,-}|}\right) \tag{B.37}$$

$$quantumyield, QY = \frac{1}{1 + \frac{k_{nr}}{k_r}\left(\frac{1}{P_{exc}} - 1\right)} \tag{B.38}$$

$$P_{exc} = \frac{1}{1 + \sum_{i=1}^{N} e^{-\frac{\Delta E_i}{kT}}} \tag{B.39}$$

Combining equations B.38 and B.39 yields:

$$QY = \frac{1}{1 + \frac{k_{nr}}{k_r}\left(\sum_{i=1}^{N} e^{-\frac{\Delta E_i}{kT}}\right)}. \tag{B.40}$$

Next, we approximate equation B.37 so that the energy difference between the exciton state and the charge transfer state varies linearly with the electric field:

$$\Delta E_i = \Delta E_0 + \mu \cdot F \tag{B.41}$$

We now make an approximation and simplify the model such that there are only two trap states relevant to the QY on each QD. The traps have same energy levels but the two are located on opposite sides of the QD, lining up along the direction of the electric field. Plugging equation B.41 into the simplified version of equation B.40

yields:

$$QY = \frac{1}{1 + \frac{k_{nr}}{k_r}\left(e^{-\frac{\Delta E_0 + \mu F}{kT}} + e^{-\frac{\Delta E_0 - \mu F}{kT}}\right)} = \frac{1}{1 + \frac{k_{nr}}{k_r} e^{-\frac{\Delta E_0}{kT}}\left(e^{-\frac{\mu F}{kT}} + e^{\frac{\mu F}{kT}}\right)} \tag{B.42}$$

We assume that the electric field, F, is proportional to the applied voltage bias minus the built-in voltage:

$$F = \alpha(V - V_{bi}) \tag{B.43}$$

Plugging equation B.43 into equation B.42 yields:

$$QY = \frac{1}{1 + \frac{k_{nr}}{k_r} e^{-\frac{\Delta E_0}{kT}}\left(e^{-\frac{\mu\alpha}{kT}(V - V_{bi})} + e^{\frac{\mu\alpha}{kT}(V - V_{bi})}\right)} \tag{B.44}$$

We parameterize equation B.44 with three parameters, B, C, and D. We also introduce another parameter, A, to normalize the QY since the measurements we take are relative QYs and not absolute QYs.

$$QY = \frac{A}{1 + B\left(e^{-C(V-D)} + e^{C(V-D)}\right)} \tag{B.45}$$

Equation B.45 is used to fit the dependence of QD PL intensities on applied voltage bias in Fig. 5-7(a). Since there are many fitting parameters, many of which lump together physically meaningful variables, we do not investigate the physical meaning in the values of the fitting parameters.

Bibliography

[1] P. O. Anikeeva, J. E. Halpert, M. G. Bawendi, and V. Bulovic. Quantum dot light-emitting devices with electroluminescence tunable over the entire visible spectrum. *Nano Lett.*, 9:2532–2536, 2009.

[2] V. Wood and V. Bulovic. Colloidal quantum dot light-emitting devices. *Nano Rev.*, 1:17, 2010.

[3] J. J. Shiang, A. V Kadavanich, R. K. Grubbs, and A. P. Alivisatos. Symmetry of annealed wurtzite CdSe nanocrystals: assignment to the C_{3v} point group. *J. Phys. Chem.*, 99:17417–17422, 1995.

[4] J. A. Hollingsworth and V. I. Klimov. *Nanocrystal Quantum Dots.* CRC Press, 2010.

[5] Y. Shirasaki, G. J. Supran, M. G. Bawendi, and V. Bulovic. Emergence of colloidal quantum-dot light-emitting technologies. *Nature Photonics*, 7:13–23, 2012.

[6] S. Coe-Sullivan, J. S. Steckel, W.-K. Woo, M. G. Bawendi, and V. Bulovic. Large-area ordered quantum-dot monolayers via phase separation during spin-casting. *Adv. Func. Mater.*, 15:1117–1124, 2005.

[7] J. W. Stouwdam and R. A. J. Janssen. Red, green, and blue quantum dot LEDs with solution processable ZnO nanocrystal electron injection layers. *J. Mater. Chem.*, 18:18891894, 2008.

[8] L. Kim et al. Contact printing of quantum dot light-emitting devices. *Nano Lett.*, 8:4513–4517, 2008.

[9] T.-H. Kim et al. Full-colour quantum dot displays fabricated by transfer printing. *Nature Photon.*, 5:176–182, 2011.

[10] S. Coe-Sullivan. presenting work from AFOSR grant. *OECD/NNI Symp.*, 2012.

[11] M. A. Baldo and S. R. Forrest. Highly efficient phosphorescent emission from organic electroluminescent devices. *Nature*, 395:151–154, 1998.

[12] J. Kwak et al. Bright and efficient full-color colloidal quantum dot light-emitting diodes using an inverted device structure. *Nano Lett.*, 12:2362–2366, 2012.

[13] N. F. Gardner, G. O. Muller, Y. C. Shen, G. Chen, S. Watanabe, W. Gotz, and M. R. Krames. Blue-emitting InGaN-GaN double-heterostructure light-emitting diodes reaching maximum quantum efficiency above 200 A/cm^2. *Appl. Phys. Lett.*, 91:243506, 2007.

[14] S.-J. Park, S. Link, W. L. Miller, A. Gesquiere, and P. F. Barbara. Effect of electric field on the photoluminescence intensity of single CdSe nanocrystals. *Chem. Phys.*, 341:169–174, 2007.

[15] W.-K. Woo et al. Reversible charging of CdSe nanocrystals in a simple solid state device. *Adv. Mater.*, 14:1068–1071, 2002.

[16] C. Galland, Y. Ghosh, A. Steinbruck, M. Sykora, J. A. Hollingsworth, V. I. Klimov, and H. Htoon. Two types of luminescence blinking revealed by spectroelectrochemistry of single quantum dots. *Nature*, 479:203–207, 2011.

[17] Y. Shirasaki, G. J. Supran, W. A. Tisdale, and V. Bulovic. Origin of efficiency roll-off in colloidal quantum-dot light-emitting diodes. *Physical Review Letters*, 2013.

[18] Y. Shirasaki, K. W. Stone, G. J. Supran, and V. Bulovic. Quantum-confined Stark effect in colloidal quantum-dot LEDs observed through electroabsorption spectroscopy. *in preparation*, 2013.

[19] Y. Shirasaki and V. Bulovic. Effect of varying quantum-dot film thickness in colloidal quantum-dot light-emitting diodes. *in preparation*, 2013.

[20] J. Oliver. Quantum dots: global market growth and future commercial prospects. *BCC Research paper*, page NAN027C, 2011.

[21] www.displaysearch.com, 2012.

[22] V. L. Colvin, M. C. Schlamp, and A. P. Alivisatos. Light-emitting diodes made from cadmium selenide nanocrystals and a semiconducting polymer. *Nature*, 370:354–357, 1994.

[23] S. Coe, W.-K. Woo, M. G. Bawendi, and V Bulovic. Electroluminescence from single monolayers of nanocrystals in molecular organic devices. *Nature*, 420:800–803, 2002.

[24] A. H. Mueller et al. Multicolor light-emitting diodes based on semiconductor nanocrystals encapsulated in GaN charge injection layers. *Nano Lett.*, 5:1039–1044, 2005.

[25] A. G. Pattantyus-Abraham et al. Depleted-heterojunction colloidal quantum dot solar cells. *ACS Nano*, 4:3374–3380, 2010.

[26] B. N. Pal et al. High-sensitivity p-n junction photodiodes based on PbS nanocrystal quantum dots. *Adv. Func. Mater.*, 22:1741–1748, 2012.

[27] G. Konstantatos et al. Ultrasensitive solution-cast quantum dot photodetectors. *Nature*, 442:180–183, 2006.

[28] W. K. Koh, S. R. Saudari, A. T. Fafarman, C. R. Kagan, and C. B. Murray. Thiocyanate-capped PbS nanocubes: ambipolar transport enables quantum dot based circuits on a flexible substrate. *Nano Lett*, 11:4764–4767, 2011.

[29] I. L. Medintz, E. R. Uyeda, H. T. adn Goldman, and H. Mattoussi. Quantum dot bioconjugates for imaging, labelling and sensing. *Nature Mater.*, 4:435–446, 2005.

[30] V. A. Shchukin and D. Bimberg. Spontaneous ordering of nanostructures on crystal surfaces. *Rev. Mod. Phys.*, 71:1125–1171, 1999.

[31] B. T. A. Klar, T. Franzl, A. L. Rogach, and J. Feldmann. Super-efficient exciton funneling in layer-by-layer semiconductor nanocrystal structures. *Adv. Mater.*, 17:769–773, 2005.

[32] M. Grundmann. The present status of quantum dot lasers. *Physica E*, 5:167184, 2000.

[33] S. Coe-Sullivan. Quantum dot developments. *Nature Photon.*, 3:315–316, 2009.

[34] C. B. Murray, D. J. Norris, and M. G. Bawendi. Synthesis and characterization of nearly monodisperse CdE (E = S, Se, Te) semiconductor nanocrystallites. *J. Am. Chem. Soc.*, 115:8706–8715, 1993.

[35] C. B. Murray, C. R. Kagan, and M. G. Bawendi. Synthesis and characterization of monodisperse nanocrystals and close-packed nanocrystal assemblies. *Ann. Rev. Mater. Sci.*, 30:545–610, 2000.

[36] K. Sanderson. Quantum dots go large. *Nature*, 459:760–761, 2009.

[37] D. J. Norris, M. G. Bawendi, and L. E. Brus. *Molecular Electronics: A "Chemistry for the 21st Century Monograph.* Blackwell Science, 1997.

[38] Y. H. Niu et al. Improved performance from multilayer quantum dot light-emitting diodes via thermal annealing of the quantum dot layer. *Adv. Mater.*, 19:3371–3376, 2007.

[39] L. Qian, Y. Zheng, J. Xue, and P. H. Holloway. Stable and efficient quantum-dot light-emitting diodes based on solution-processed multilayer structures. *Nature Photon.*, 5:543–548, 2011.

[40] Q. Sun et al. Bright, multicoloured light-emitting diodes based on quantum dots. *Nature Photon.*, 1:717–722, 2007.

[41] L. Sun et al. Bright infrared quantum-dot light-emitting diodes through inter-dot spacing control. *Nature Nanotech.*, 7:369373, 2012.

[42] G. Konstantatos, C. Huang, L. Levina, Z. Lu, and E. H. Sargent. Efficient infrared electroluminescent devices using solution-processed colloidal quantum dots. *Adv. Func. Mater.*, 15:1865–1869, 2005.

[43] J. Lee, V. C. Sundar, J. R. Heine, M. G. Bawendi, and K. F. Jensen. Full color emission from II-VI semiconductor quantum dot-polymer composites. *Adv. Mater.*, 12:1102–1105, 2000.

[44] J. A Chen. High-efficiency wide-color-gamut solid-state backlight system for LCDs using quantum-dot enhancement film. *SID Display Week 2012*, 2012.

[45] M. A. Hines and P. Guyot-sionnest. Synthesis and characterization of strongly luminescing ZnS-capped CdSe nanocrystals. *J. Phys. Chem.*, 100:468–471, 1996.

[46] B. O. Dabbousi et al. (CdSe)ZnS core-shell quantum dots: synthesis and characterization of a size series of highly luminescent nanocrystallites. *J. Phys. Chem. B*, 101:9463–9475, 1997.

[47] X. Peng, M. C. Schlamp, A. V. Kadavanich, and A. P. Alivisatos. Epitaxial growth of highly luminescent CdSe/CdS core/shell nanocrystals with photostability and electronic accessibility. *J. Am. Chem. Soc.*, 119:7019–7029, 1997.

[48] J. M. Pietryga et al. Utilizing the lability of lead selenide to produce heterostructured nanocrystals with bright, stable infrared emission. *J. Am. Chem. Soc.*, 130:4879–4885, 2008.

[49] T. Chang et al. High near-infrared photoluminescence quantum efficiency from PbS nanocrystals in polymer films. *Synth. Metals*, 148:257–261, 2005.

[50] C. R. Kagan, C. B. Murray, M. Nirmal, and M. G. Bawendi. Electronic energy transfer in CdSe quantum dot solids. *Phys. Rev. Lett.*, 76:1517–1520, 1996.

[51] C. Kagan, C. Murray, and M. G. Bawendi. Long-range resonance transfer of electronic excitations in close-packed CdSe quantum-dot solids. *Phys. Rev. B*, 54:8633–8643, 1996.

[52] F. Xu et al. Efficient exciton funneling in cascaded pbs quantum dot superstructures. *ACS Nano*, 5:9950–9957, 2011.

[53] A. Efros et al. Band-edge exciton in quantum dots of semiconductors with a degenerate valence band: dark and bright exciton states. *Phys. Rev. B*, 54:4843–4856, 1996.

[54] T. Zhu et al. Mist fabrication of light emitting diodes with colloidal nanocrystal quantum dots. *Appl. Phys. Lett.*, 92:023111, 2008.

[55] H. M. Haverinen, R. A. Myllyl, and G. E. Jabbour. Inkjet printing of light emitting quantum dots. *Appl. Phys. Lett.*, 94:073108, 2009.

[56] V. Wood et al. Inkjet-printed quantum dot-polymer composites for full-color AC-driven displays. *Adv. Mater.*, pages 2151–2155, 2009.

[57] K.-S. Cho et al. High-performance crosslinked colloidal quantum-dot light-emitting. *Nature Photon.*, 3:341–345, 2009.

[58] X. Ma, F. Xu, J. Benavides, and S. G. Cloutier. High performance hybrid near-infrared LEDs using benzenedithiol cross-linked PbS colloidal nanocrystals. *Org. Electron.*, 13:525–531, 2012.

[59] J. Kwak et al. Characterization of quantum dot/conducting polymer hybrid films and their application to light-emitting diodes. *Adv. Mater.*, 21:5022–5026, 2009.

[60] Y. Liu et al. Dependence of carrier mobility on nanocrystal size and ligand length in PbSe nanocrystal solids. *Nano Lett.*, 10:1960–1969, 2010.

[61] A. V. Malko et al. From amplified spontaneous emission to microring lasing using nanocrystal quantum dot solids. *Appl. Phys. Lett.*, 81:1303–1305, 2002.

[62] Z. Tang, B. Ozturk, Y. Wang, and N. A. Kotov. Simple preparation strategy and one-dimensional energy transfer in CdTe nanoparticle chains. *J. Phys. Chem. B*, 108:6927–6931, 2004.

[63] M. Nirmal et al. Fluorescence intermittency in single cadmium selenide nanocrystals. *Nature*, 383:802–804, 1996.

[64] W. G. J. H. M. van Sark, P. L. T. M. Frederix, A. A. Bol, H. C. Gerritsen, and A. Meijerink. Blueing, bleaching, and blinking of single CdSe/ZnS quantum dots. *ChemPhysChem*, 3:871–879, 2002.

[65] F. Koberling and A. B. Mews. Oxygen-induced blinking of single CdSe nanocrystals. *Adv. Mater.*, 13:672–676, 2001.

[66] X. Wang, J. Zhang, A. Nazzal, and M. Xiao. Photo-oxidation-enhanced coupling in densely packed CdSe quantum-dot films. *Appl. Phys. Lett.*, 83:162–164, 2003.

[67] D. B. Tice, M. T. Frederick, R. P. H. Chang, and E. A. Weiss. Electron migration limits the rate of photobrightening in thin films of CdSe quantum dots in a dry N_2 (g) atmosphere. *J. Phys. Chem. C*, 115:3654–3662, 2011.

[68] M. Jones, J. Nedeljkovic, R. J. Ellingson, A. J. Nozik, and G. Rumbles. Photoenhancement of luminescence in colloidal CdSe quantum dot solutions. *J. Phys. Chem. B*, 107:11346–11352, 2003.

[69] S. R. Cordero, P. J. Carson, R. A. Estabrook, G. F. Strouse, and S. K. Buratto. Photo-activated luminescence of CdSe quantum dot monolayers. *J. Phys. Chem. B*, 104:12137–12142, 2000.

[70] M. Oda et al. Photoluminescence of CdSe/ZnS/TOPO nanocrystals expanded on silica glass substrates: adsorption and desorption effects of polar molecules on nanocrystal surfaces. *J. Lumin.*, 119–120:570–575, 2006.

[71] T. Uematsu, S. Maenosono, and Y. Yamaguchi. Photoinduced fluorescence enhancement in mono- and multilayer films of CdSe/ZnS quantum dots: dependence on intensity and wavelength of excitation light. *J. Phys. Chem. B*, 109:8613–8618, 2005.

[72] Y. Chen et al. Giant multishell CdSe nanocrystal quantum dots with suppressed blinking. *J. Am. Chem. Soc.*, 130:5026–5027, 2008.

[73] B. Mahler et al. Towards non-blinking colloidal quantum dots. *Nature Mater.*, 7:659–664, 2008.

[74] S. Hohng and T. Ha. Near-complete suppression of quantum dot blinking in ambient conditions. *J. Am. Chem. Soc.*, 126:1324–1325, 2004.

[75] X. Wang et al. Non-blinking semiconductor nanocrystals. *Nature*, 459:686–689, 2009.

[76] P. Spinicelli et al. Non-blinking semiconductor colloidal quantum dots for biology, optoelectronics and quantum optics. *ChemPhysChem*, 10:879–882, 2009.

[77] M. V. Kovalenko, M. Scheele, and D. V. Talapin. Colloidal nanocrystals with molecular metal chalcogenide surface ligands. *Science*, 324:1417–1420, 2009.

[78] A. Nag et al. Metal-free inorganic ligands for colloidal nanocrystals: S2, HS, Se2, HSe, Te2, HTe, TeS3. *J. Am. Chem. Soc.*, 133:10612–10620, 2011.

[79] U. Resch-Genger, M. Grabolle, S. Cavaliere-Jaricot, R. Nitschke, and T. Nann. Quantum dots versus organic dyes as fluorescent labels. *Nature Meth.*, 5:763–775, 2008.

[80] R. Meerheim et al. Influence of charge balance and exciton distribution on efficiency and lifetime of phosphorescent organic light-emitting devices. *J. Appl. Phys.*, 104:014510, 2008.

[81] D. J. Griffiths. *Introduction to Quantum Mechanics Second Edition.* Pearson Prentice Hall, 2005.

[82] D. J. Norris and M. G. Bawendi. Measurement and assignment of the size-dependent optical spectrum in CdSe quantum dots. *Phys. Rev. B*, 53:16338–16346, 1996.

[83] M. Nirmal, D. J. Norris, M. Kuno, M. G. Bawendi, A. L. Efros, and M. Rosen. Observation of the "dark exciton" in CdSe quantum dots. *Phys. Rev. Lett.*, 75:3728–3731, 1995.

[84] M. Fox. *Optical Properties of Solids.* Oxford University Press, 2003.

[85] C. W. Tang and S. A. VanSlyke. Organic electroluminescent diodes. *Appl. Phys. Lett.*, 51:913–915, 1987.

[86] M. A. Baldo, S. Lamansky, P. E. Burrows, M. E. Thompson, and S. R. Forrest. Very high-efficiency green organic light-emitting devices based on electrophosphorescence. *Appl. Phys. Lett.*, 75, 1999.

[87] S. Coe-Sullivan. Nanotechnology for displays: a potential breakthrough for OLED displays and LCDs. *SID Display Week 2012*, 2012.

[88] B. S. Mashford, M. Stevenson, Z. Popovic, C. Hamilton, Z. Zhou, C. Breen, J. Steckel, V. Bulovic, M. Bawendi, S. Coe-Sullivan, and P. T. Kazlas. High-efficiency quantum-dot light-emitting devices with enhanced charge injection. *Nature Photon.*, 2013.

[89] B. O. Dabbousi, M. G. Bawendi, O. Onitsuka, and M. F. Rubner. Electroluminescence from CdSe quantum-dot/polymer composites. *Appl. Phys. Lett.*, 66:1316–1318, 1995.

[90] H. Mattoussi et al. Electroluminescence from heterostructures of poly(phenylene vinylene) and inorganic CdSe nanocrystals. *J. Appl. Phys.*, 83:7965–7974, 1998.

[91] M. C. Schlamp, X. Peng, and A. P. Alivisatos. Improved efficiencies in light emitting diodes made with CdSe(CdS) core/shell type nanocrystals and a semiconducting polymer. *J. Appl. Phys.*, 82:5837–5842, 1997.

[92] T.-W. F. Chang et al. Efficient excitation transfer from polymer to nanocrystals. *Appl. Phys. Lett.*, 84:4295–4297, 2004.

[93] M. J. Panzer et al. Nanoscale morphology revealed at the interface between colloidal quantum dots and organic semiconductor films. *Nano Lett.*, 10:2421–2426, 2010.

[94] M. Achermann et al. Energy-transfer pumping of semiconductor nanocrystals using an epitaxial quantum well. *Nature*, 429:642–646, 2004.

[95] M. Achermann, M. A Petruska, D. D. Koleske, M. H. Crawford, and V. I. Klimov. Nanocrystal-based light-emitting diodes utilizing high-efficiency nonradiative energy transfer for color conversion. *Nano Lett.*, 6:1396–1400, 2006.

[96] J. S. Steckel et al. Color-saturated green-emitting QD-LEDs. *Angew. Chem.*, 45:5796–5799, 2006.

[97] P. O. Anikeeva, C. F. Madigan, J. E. Halpert, M. G. Bawendi, and V. Bulovic. Electronic and excitonic processes in light-emitting devices based on organic materials and colloidal quantum dots. *Phys. Rev. B*, 78:085434, 2008.

[98] A. Rizzo et al. Hybrid light-emitting diodes from microcontact-printing double-transfer of colloidal semiconductor CdSe/ZnS quantum dots onto organic layers. *Adv. Mater.*, 20:1886–1891, 2008.

[99] S. A. Empedocles and M. G. Bawendi. Quantum-confined stark effect in single CdSe nanocrystallite quantum dots. *Science*, 278:2114–2117, 1997.

[100] P. O. Anikeeva, J. E. Halpert, M. G. Bawendi, and V. Bulovic. Electroluminescence from a mixed red-green-blue colloidal quantum dot monolayer. *Nano Lett.*, 7:2196–2200, 2007.

[101] Y. Q. Li, A. Rizzo, R. Cingolani, and G. Gigli. Bright white-light-emitting device from ternary nanocrystal composites. *Adv. Mater.*, 18:2545–2548, 2006.

[102] P. Jing et al. Shell-dependent electroluminescence from colloidal CdSe quantum dots in multilayer light-emitting diodes. *J. Appl. Phys.*, 105:044313, 2009.

[103] R. H. Friend et al. Electroluminescence in conjugated polymers. *Nature*, 397:121–128, 1999.

[104] P. E. Burrows, V. Bulovic, S. R. Forrest, L. S. Sapochak, and D. M. Mccarty. Reliability and degradation of organic light emitting devices. *Appl. Phys. Lett.*, 65:2922–2924, 1994.

[105] J. M. Caruge, J. E. Halpert, V. Wood, V. Bulovic, and M. G. Bawendi. Colloidal quantum-dot light-emitting diodes with metal-oxide charge transport layers. *Nature Photon.*, 2:247–250, 2008.

[106] V. Wood et al. Selection of metal oxide charge transport layers for colloidal quantum dot LEDs. *ACS Nano*, 3:3581–3586, 2009.

[107] Vanessa Wood, Matthew J. Panzer, Deniz Bozyigit, Yasuhiro Shirasaki, Ian Rousseau, Scott Geyer, Moungi G. Bawendi, and Vladimir Bulovic. Electroluminescence from nanoscale materials via field-driven ionization. *Nano Letters*, 11:2927–2932, 2011.

[108] S. H. Cho et al. High performance AC electroluminescence from colloidal quantum dot hybrids. *Adv. Mater.*, 24:4540–4546, 2012.

[109] D. Bozyigit, V. Wood, Y. Shirasaki, and V. Bulovic. Study of field driven electroluminescence in colloidal quantum dot solids. *J. Appl. Phys.*, 111:113701, 2012.

[110] J.-M. Caruge, J. E. Halpert, V. Bulovic, and M. G. Bawendi. Nio as an inorganic hole-transporting layer in quantum-dot light-emitting devices. *Nano Lett.*, 6:2991–2994, 2006.

[111] C. Borek et al. Highly efficient, near-infrared electrophosphorescence from a Pt-metalloporphyrin complex. *Angew. Chem.*, 46:1109–1112, 2007.

[112] J. R. Sommer et al. Efficient near-infrared polymer and organic light-emitting diodes based on electrophosphorescence from (tetraphenyltetranaphtho-2,3-porphyrin)platinum(ii). *ACS Appl. Mater. Interf.*, 1:274–278, 2009.

[113] G. Qian et al. Simple and efficient near-infrared organic chromophores for light-emitting diodes with single electroluminescent emission above 1000 nm. *Adv. Mater.*, 21:111–116, 2009.

[114] G. J. S. Supran et al. High efficiency and brightness near-infrared quantum-dot LEDs. *US patent application no. 61/735,344*, 2012.

[115] Who goes there: Friend or foe?, 1993.

[116] Y. T. Lim, S. Kim, A. Nakayama, N. E. Stott, M. G. Bawendi, and J. V. Frangioni. Selection of quantum dot wavelengths for biomedical assays and imaging. *Mol. Imag.*, 2:50–64, 2003.

[117] P. Yager et al. Microfluidic diagnostic technologies for global public health. *Nature*, 442:412–418, 2006.

[118] E. H. Sargent. Infrared quantum dots. *Adv. Mater.*, 17:515–522, 2005.

[119] K. N. Bourdakos, D. M. N. M. Dissanayake, T. Lutz, S. R. P. Silva, and R. J. Curry. Highly efficient near-infrared hybrid organic-inorganic nanocrystal electroluminescence device. *Appl. Phys. Lett.*, 92:153311, 2008.

[120] J. S. Steckel, S. Coe-Sullivan, V. Bulovic, and M. G. Bawendi. 1.3m to 1.55m tunable electroluminescence from PbSe quantum dots embedded within an organic device. *Adv. Mater.*, 15:1862–1866, 2003.

[121] K. R. Choudhury, D. W. Song, and F. So. Efficient solution-processed hybrid polymer-nanocrystal near infrared light-emitting devices. *Org. Electron.*, 11:23–28, 2010.

[122] S. Hoogland et al. Megahertz-frequency large-area optical modulators at 1.55 m based on solution-cast colloidal quantum dots. *Opt. Express*, 16:6683–6691, 2008.

[123] A. L. Rogach, A. Eychmller, S. G. Hickey, and S. V. Kershaw. Infrared-emitting colloidal nanocrystals: synthesis, assembly, spectroscopy, and applications. *Small*, 3:536–557, 2007.

[124] S. V. Kershaw, M. Harrison, A. L. Rogach, and A. Kornowski. Development of IR-emitting colloidal IIVI quantum-dot materials. *IEEE J. Sel. Top. Quant. Electron.*, 6:534–543, 2000.

[125] K.-Y. Cheng, R. Anthony, U. R. Kortshagen, and R. J. Holmes. High efficiency silicon nanocrystal light-emitting devices. *Nano Lett.*, 11:1952–1956, 2011.

[126] N. Tessler, V. Medvedev, M. Kazes, S. Kan, and U. Banin. Efficient near-infrared polymer nanocrystal light-emitting diodes. *Science*, 295:1506–1508, 2002.

[127] L. Bakueva et al. Size-tunable infrared (1000-1600 nm) electroluminescence from PbS quantum-dot nanocrystals in a semiconducting polymer. *Appl. Phys. Lett.*, 82:2895–2897, 2003.

[128] O. Solomeshch et al. Optoelectronic properties of polymer-nanocrystal composites active at near-infrared wavelengths. *J. Appl. Phys.*, 98:074310, 2005.

[129] K.-Y. Cheng, R. Anthony, U. R. Kortshagen, and R. J. Holmes. Hybrid silicon nanocrystal-organic light-emitting devices for infrared electroluminescence. *Nano Lett.*, 10:1154–1157, 2010.

[130] D. S. Koktysh et al. Near-infrared electroluminescence from HgTe nanocrystals. *ChemPhysChem*, 5:1435–1438, 2004.

[131] E. O'Connor et al. Near-infrared electroluminescent devices based on colloidal HgTe quantum dot arrays. *Appl. Phys. Lett.*, 86:201114, 2005.

[132] Y. Zhang et al. Employing heavy metal-free colloidal quantum dots in solution-processed white light-emitting diodes. *Nano Lett.*, 11:329–332, 2011.

[133] Z. Tan et al. Near-band-edge electroluminescence from heavy-metal-free colloidal quantum dots. *Adv. Mater.*, 23:3553–3558, 2011.

[134] D. Kovalev et al. Breakdown of the k-conservation rule in Si nanocrystals. *Phys. Rev. Lett.*, 81:2803–2806, 1998.

[135] D. Jurbergs, E. Rogojina, L. Mangolini, and U. Kortshagen. Silicon nanocrystals with ensemble quantum yields exceeding 60 *Appl. Phys. Lett.*, 88:233116, 2006.

[136] R. K. Ligman, L. Mangolini, U. R. Kortshagen, and S. A. Campbell. Electroluminescence from surface oxidized silicon nanoparticles dispersed within a polymer matrix. *Appl. Phys. Lett.*, 90:061116, 2007.

[137] L. Mangolini, E. Thimsen, and U. Kortshagen. High-yield plasma synthesis of luminescent silicon nanocrystals. *Nano Lett.*, 5:655–659, 2005.

[138] P. R. Brown, R. R. Lunt, N. Zhao, T. P. Osedach, D. D. Wanger, L.-Y. Chang, M. G. Bawendi, and V. Bulovic. Improved current extraction from ZnO/PbS quantum dot heterojunction photovoltaics using a MoO_3 interfacial layer. *Nano Lett.*, 11:2955–2961, 2011.

[139] S. Reineke, G. Schwartz, K. Walzer, and K. Leo. Reduced efficiency roll-off in phosphorescent organic light emitting diodes by suppression of triplet-triplet annihilation. *Appl. Phys. Lett.*, 91:123508, 2007.

[140] D. Pugh-Thomas, B. M. Walsh, and M. C. Gupta. CdSe(ZnS) nanocomposite luminescent high temperature sensor. *Nanotechnology*, 22:185503, 2011.

[141] H. Huang, A. Dorn, G. P. Nair, V. Bulovic, and M. G. Bawendi. Bias-induced photoluminescence quenching of single colloidal quantum dots embedded in organic semiconductors. *Nano Lett.*, 7:3781–3786, 2007.

[142] V. I. Klimov, A. A. Mikhailovsky, D. W. McBranch, C. A. Leatherdale, and M. G. Bawendi. Quantization of multiparticle Auger rates in semiconductor quantum dots. *Science*, 287:1011–2013, 2000.

[143] T. Hartmann, P. Reineker, and V. I. Yudson. Auger release of a deeply trapped carrier in a quantum dot. *Phys. Rev. B*, 84:245317, 2011.

[144] A. W. Cohn, A. M. Schimpf, C. E. Gunthardt, and D. R. Gamelin. Size-dependent trap-assisted Auger recombination in semiconductor nanocrystals. *Nano Letters*, 13:1810–1815, 2013.

[145] Y. Wu, K. Arai, and T. Yao. Temperature dependence of the photoluminescence of ZnSe/ZnS quantum-dot structures. *Phys. Rev. B*, 53:R10485–R10488, 1996.

[146] C.-C. Pan, T. Gilbert, N. Pfaff, S. Tanaka, Y. Zhao, D. Feezell, J. S. Speck, S. Nakamura, and S. P. DenBaars. Reduction in thermal droop using thick single-quantum-well structure in semipolar $(20\bar{2}\bar{1})$ blue light-emitting diodes. *Applied Physics Express*, 5:102103, 2012.

[147] D. Bozyigit, O. Yarema, and V. Wood. Origins of low quantum effciencies in quantum dot LEDs. *Advabced Functional Materials*, 2013.

[148] C. A. Leatherdale, C. R. Kagan, N. Y. Morgan, S. A. Empedocles, M. A. Kastner, and M. G. Bawendi. Photoconductivity in CdSe quantum dot solids. *Phys. Rev. B*, 62:2669–2680, 2000.

[149] L. Yang, B. Wei, and J. Zhang. Transient thermal characterization of organic light-emitting diodes. *Semicond. Sci. Technolo.*, 27:105011, 2012.

[150] K. J. Bergemann, R. Krasny, and S. R. Forrest. Thermal properties of organic light-emitting diodes. *Organic Electronics*, 13:1565–1568, 2012.

[151] C. A. Leatherdale and M. G. Bawendi. Observation of solvatochromism in CdSe colloidal quantum dots. *Phys. Rev. B*, 63:165315, 2001.

[152] I. H. Campbell, M. D. Joswick, and I. D. Parker. Direct measurement of the internal electric field distribution in a multilayer organic light-emitting diode. *Appl. Phys. Lett.*, 67:3171–3173, 1995.

[153] A. S. Dissanayake, J. Y. Lin, and H. X. Jiang. Quantum-confined Stark effects in $CdS_{1-x}Se_x$ quantum dots. *Phys. Rev. B*, 51, 1995.

[154] G. W. Wen, J. Y. Lin, H. X. Jiang, and Z. Chen. Quantum-confined Stark effects in semiconductor quantum dots. *Phys. Rev. B*, 52:5913–5922, 1995.

[155] M. V. Jarosz, V. J. Porter, B. R. Fisher, M. A. Kastner, and M. G. Bawendi. Photoconductivity studies of treated CdSe quantum dot films exhibiting increased exciton ionization efficiency. *Phys. Rev. B*, 70:195327, 2004.

[156] A. Pandey and P. Guyot-Sionnest. Hot electron extraction from colloidal quantum dots. *J. Phys. Chem. Lett.*, 1:45–47, 2010.

[157] C. Wang, B. L. Wehrenberg, C. Y. Woo, and P. Guyot-Sionnest. Light emission and amplification in charged CdSe quantum dots. *J. Phys. Chem. B*, 108:9027–9031, 2004.

[158] P. P. Jha and P. Guyot-Sionnest. Photoluminescence switching of charged quantum dot films. *J. Phys. Chem. C*, 111:15440–15445, 2007.

[159] R. Berera, R. van Grondelle, and J. T. M. Kennis. Ultrafast transient absorption spectroscopy: principles and application to photosynthetic systems. *Photosynth. Res.*, 101:105–118, 2009.

[160] V. I. Klimov. Optical nonlinearities and ultrafast carrier dynamics in semiconductor nanocrystals. *J. Phys. Chem. B*, 104:6112–6123, 2000.

[161] P. Kambhampati. Hot exciton relaxation dynamics in semiconductor quantum dots: Radiationless transitions on the nanoscale. *J. Phys. Chem. C*, 115:22089–22109, 2011.

[162] G. U. Bublitz and S. G. Boxer. Stark spectroscopy: Applications in chemistry, biology, and materials science. *Annu. Rev. Phys. Chem.*, 48:213–242, 1997.

[163] D. J. Norris, A. Sacra, C. B. Murray, and M. G. Bawendi. Measurement of the size dependent hole spectrum in CdSe quantum dots. *Phys. Rev. Lett.*, 72:2612–2615, 1994.

[164] B. Ruhstaller, S. A. Carter, S. Barth, H. Riel, W. Riess, and J. C. Scott. Transient and steady-state behavior of space charges in multilayer organic light-emitting diodes. *J. Appl. Phys.*, 89:4575–4586, 2001.

[165] J. Park. Speedup of dynamic response of organic light-emitting diodes. *J. Lightwave Technol.*, 28:2873–2880, 2010.

[166] M.-H. Tsai, Y.-H. Hong, C.-H. Chang, H.-C. Su, C.-C. Wu, A. Matoliukstyte, J. Simokaitiene, S. Grigalevicius, J. V. Grazulevicius, and C.-P. Hsu. 3-(9-carbazolyl)carbazoles and 3,6-di(9-carbazolyl)carbazoles as effective host materials for efficient blue organic electrophosphorescence. *Advanced Materials*, 19:862–866, 2007.

[167] Y. Kuwabara, H. Ogawa, H. Inada, N. Noma, and Y. Shirota. Thermally stable multilayered organic electroluminescent devices using novel starburst molecules, 4,4',4"-tri(*N*-carbazolyl)triphenylamine (TCTA) and 4,4',4"-tris(3-methylphenylphenyl-amino)triphenylamine (m-MTDATA), as hole-transport materials. *Advanced Materials*, 6:677–679, 1994.

[168] C. Madigan and V. Bulovic. Course notes for Organic Optoelectronics class at MIT. Class number 6.789, dated 2002, 2013.

[169] Y. Shirasaki, P. O. Anikeeva, J. R. Tischler, M. S. Bradley, and V. Bulovic. Efficient Förster energy transfer from phosphorescent organic molecules to J-aggregate thin films. *Chem. Phys. Lett.*, 18:243–246, 2010.

[170] P. E. Burrows, Z. Shen, V. Bulovic, D. M. McCarty, S. R. Forrest, J. A. Cronin, and M. E. Thompson. Relationship between electroluminescence and current transport in organic heterjunction light-emitting devices. *J. Appl. Phys.*, 79:7991–8006, 2013.

[171] A. Rose. Space-charge-limited currents in solids. *Physical Review*, 97:1538–1544, 1955.

[172] M. A. Lampert. Space-charge-limited currents in an insulator with traps. *Physical Review*, 103:1648–1656, 1956.

[173] A. Rose. *Concepts in Photoconductivity and Allied Problems.* Interscience Publishers, 1963.

[174] P. W. M. Blom, M. J. M. de Jong, and M. G. van Munster. Electric-field and temperature dependence of the hole mobility in poly(p-phenylene vinylene). *Phys. Rev. B*, 55:656–659, 1997.